MODELING VOLCANIC ASH AND SULFUR DIOXIDE WITH THE WEATHER RESEARCH FORECASTING WITH CHEMISTRY (WRF-CHEM) MODEL

By

Sean D. Egan, B.S.

A Dissertation Submitted in Partial Fulfillment of the Requirements

for the Degree of

DOCTOR OF PHILOSOPHY

in

Environmental Chemistry

University of Alaska Fairbanks

December 2019

APPROVED:

Dr. Catherine Cahill, Committee Co-Chair
Dr. Martin Stuefer, Committee Co-Chair
Dr. Peter Webley, Committee Member
Dr. Taryn Lopez, Committee Member
Dr. William Simpson, Committee Member
Dr. Thomas Green, Department Chair
Department of Chemistry
Dr. Kinchel Doerner, Dean
College of Natural Science and Mathematics
Dr. Michael Castellini
Dean of the Graduate School

ABSTRACT

The Weather Research Forecasting with Chemistry (WRF-Chem) model is capable of modeling volcanic emissions of ash, sulfur dioxide and water vapor. Here, it is applied to eruptions from three volcanoes: the 2008 eruption of Kasatochi Volcano in Alaska, the 2010 eruption of Eyjafjallajökull in Iceland and the 2019 eruption of Raikoke in the Kurile Islands. WRF-Chem's ability to model volcanic emissions dispersion is validated through comparison of model output to remote sensing, in situ and field measurements. A sensitivity of the model to modeled plume height is discussed. This work also modifies the base WRF-Chem code in three ways and studies the effects of these modifications. First, volcanic ash aggregation parameterizations are added covering three modes of particle collisions through Brownian motion, differential settling and shear. Second, water vapor emissions from volcanic eruptions are added and coupled to the new aggregation scheme. The effects of these changes are assessed and found to produce volcanic ash concentrations in agreement with in situ measurements of plume concentrations and field measurements of tephra fallout. Third, the model is adapted to include multiple model initializations such that each is perturbed by selecting between two volcanic ash particle sizes and five initial plume heights. This modified WRF-Chem is nested in an application program interface that enables a new, automated, near real-time capability. This capability is assessed and the feasibility of its use as an augmenting tool to current operational VATD models is commented upon.

TABLE OF CONTENTS

Page

LIST OF FIGURES

LIST OF TABLES

ACKNOWLEDGEMENTS AND DEDICATION

The works presented in this dissertation arose in part from the help and guidance of many people who deserve acknowledgment and thanks for their efforts. In particular, I want to thank my committee co-chairs and members; Dr. Cathy Cahill for first recruiting me as a graduate student, for her positive and encouraging attitude, for her extensive expertise and for sticking by me through the ups and downs of my graduate career; Dr. Martin Stuefer, for giving me guidance without boundaries and limitless lab space despite a limited supply; Dr. Peter Webley, for his enthusiasm, his wit and his ability to succinctly convey complex ideas; Dr. Taryn Lopez, who provided a sharp mind, keen intellect and detailed approach to the review of my work; and Dr. Bill Simpson, the greatest professor and teacher I have ever known, whose knowledge of atmospheric chemistry is now the foundation of my own. Without this solid and dedicated committee, these chapters would have never come together as individual works, let alone as a compiled dissertation.

A number of colleagues deserve thanks for their help in my studies; Dr. Alexa Van Eaton at the Cascades Volcano Observatory provided guidance in the development of the equations used in Chapter 3; Hans Schwaiger with the Alaska Volcano Observatory provided the initial motivation that prompted my work on volcanic ash physics. Dr. Arnau Folch with the Barcelona Supercomputing Center provided feedback and suggestions regarding my first attempts at incorporating volcanic ash aggregation into the WRF-Chem base code. Don Bahls and Oralee Knudson with the Arctic Region Supercomputing Center taught me just enough Linux to become a professional, independent and productive supercomputer user.

Additionally, this dissertation would not have been possible without the numerous people who were in my life to support me and who also deserve recognition and thanks for their efforts. Above all else I depended most on my husband, partner and best friend of 13 years, David Robinson, whose dreams inspire my own and whose limitless encouragement, patience and love makes any goal possible to achieve. To my mentors, Larry Michael and Allan Ramsey, who showed me that hard work and close friends are both key to success in life. To my roommates, Dr. Colin Triplett and Luke Wetzel, who provided the intellectual and emotional support I needed when the studies got rough, when my husband was deployed, when I didn't know who else to turn to for advice and for always finding a way to keep me grounded. I especially want to give thanks to my officemate, Dr. Christine Waigl, who didn't just give me coding advice and feedback on my

writing, but who also gave me a friendship that supported me through comprehensive exams, a dissertation proposal, a dissertation defense, and all the little nuances that come between those milestones. To Dr. Mark Faller, who ensured I did not pursue scientific knowledge blindly and who taught me to question what I believe in. And to Dr. Matthew Blackett, who gave me friendship, hospitality, encouragement and a place to escape to across the pond when I needed to get away.

As an Officer in the United States Navy, I'd like give thanks to my colleagues who supported my efforts in the completion of this dissertation. First, to Lieutenant Commander Gregory Contreras, who was there for me when I didn't know what path to go down. His mentoring and experience continues to show me how I may best apply my talents to serve the United States Navy with honor, courage and commitment. This dissertation would not have been possible without his support. Secondly, to the members of my current command, the Joint Typhoon Warning Center, for sharing the watch and the culmination of my doctoral studies with me. I am proud to serve our country, to protect our sailors, marines, airmen and soldiers and to defend freedom and democracy around the world alongside all of you.

Finally, I'd like to thank my family. To the closest thing I have to brothers; Andrew Ahumada and Clayton Damm, who have always given me a warm home full of friendship to return to; Anthony Holmes-Orem, who puts my decisions and outlook on life into perspective; and Raul Villa Rojas, whose wisdom and perseverance has given me strength for so many years. You three have my deepest gratitude for the long summer days full of hikes, the long winter nights full of laughter and for sharing the hard times with me. Thank you to my late father, David Egan, my mother, Nancy Reynolds Egan and my aunt, Janet Reynolds Asher for your friendship, for all of your years of support, for always welcoming me back home, for participating in all of life's milestones with me and for the love you've given Dave and me over the years.

This dissertation is dedicated to Veronica Husak, without whose love and friendship I would have never truly begun to live.

CHAPTER 1 – INTRODUCTION

1.1 ORIGINS OF AIR POLLUTION MODELING AND DISSERTATION MOTIVATION

Atmospheric modeling as a science arose from a fundamental human need to forecast the weather. Government and merchant naval vessels desired to understand and predict weather to ensure successful trade and exploration missions (Jacobson, 2005). Farmers needed a basic understanding of weather to grow crops and feed their people. As the scientific community developed our understanding of mathematics and physics, it began to apply this understanding to the motions of the atmosphere in an effort to better predict the weather. At first this led to the development of a graphical calculus where physical observations, such as wind speeds, were geometrically interpolated into continuous isolines. This gave way to the use of discretized, gridded surfaces allowing for the application of the analytical "primitive" meteorological equations in finite-difference form to be applied to individual cells, beginning with initial attempts at numerical solutions for entire forecast periods in the 1900s (Hunt, 1998). These primitive equations describe the atmosphere through three types of equations: a continuity equation, equations describing the conservation of momentum, and a thermal energy equation. Features such as gradient winds could be resolved on a large scale, though through a laborious process, giving rise to some of the first numerical weather prediction forecasts (Hunt, 1998).

The advent of the computer in the mid-1900s increased the feasibility, and thus the use of, numerical weather prediction methods. Calculations of primitive equations could be solved faster and with less error with computers than by hand. As computational power increased, the methods used to solve the primitive equations also improved, moving from 1 dimensional (1D) to 4 dimensional (4D) methods, including variables in the horizontal (i,j), vertical (k) and in time (t) dimensions (Lynch, 2008).

Eventually, national governments formed meteorological agencies such as the United States' National Oceanic and Atmospheric Administration (NOAA) and National Weather Service (NWS) in order to predict and better understand the weather. These agencies adapted existing numerical methods to forecast the weather on a global scale through the development of global spectral models such as the Global Forecast System (GFS), developed by NOAA, and the Integrated Forecast System (IFS), developed by the European Center for Medium-Range Weather

Forecasts (ECMWF). A range of customers, from individuals to governmental agencies, now use these models today.

While air pollution has existed as a concern for many decades, compared to weather prediction it has more recently developed into an area of intensive scientific study. Volcanic eruptions (Francesco et al., 2015; Church et al., 2005; Hansen et al., 1992; Sigurdsson, 1990; Kelly and Sear, 1984), forest fires (Aponte et al., 2016; Jung et al., 2014; Emmanuel, 2001; Flannigan, 2000), dust storms (Kedia et al., 2018; Manktelow et al., 2010; Slingo et al., 2006; Zhuang, 2001) and meteorite impacts (Coldwell, 2018; Artemieva et al., 2017; Brown et al., 2008; Toon, 1984) all generate particulate matter that can affect the earth's climate system and the life that inhabits it. For example, volcanic sulfur dioxide (SO_2) is suspected to have caused the "little ice age" by enhancing albedo in the upper atmosphere (Crowley et al., 2008). As industrialization occurred, anthropogenic emissions became a large source of air pollution starting in Britain, with bouts of smog that killed over 4,000 people in London in the winter of 1952 (Davis DL, 2002). Petrochemical smog in the Los Angeles basin gave rise to the study of air pollution in earnest due to resulting legislation to improve air quality.

The need to study and forecast air pollution episodes gave rise to particle dispersion models. Whereas previous models were tailored for weather prediction, these models studied other aspects of chemical species in the atmosphere, such as their origin, rate of change during transport, and ultimate fate (Holmes and Morawska, 2006). Today, dispersion models are used to study a variety of atmospheric problems such as petrochemical conversion, aerosol generation and transport, radionuclide transport, transpacific dust transport, haze and volcanic ash transport (Holmes and Morawska, 2006). Volcanic ash modeling is of particular concern for civilian and military aviation communities, as ash clouds can seize jet engines, clog fuel lines, interfere with radio transmissions and infiltrate cabins, resulting in carryon economic and logistical challenges (Casadevall, 1992; Miller, Casadevall, et al., 2000). For example, the volcanic ash clouds associated with the 1989 eruption of Mount Redoubt damaged 79 aircraft, 26 of which involved severe damage, and 9 which involved engine failure (Guffanti et al., 2010).

This dissertation studies the capability of the Weather Research Forecasting with Chemistry (WRF-Chem) model (Grell et al., 2009), a mesoscale, numerical weather prediction model, to forecast volcanic emissions and includes an effort to improve the existing capability for

use in volcanic ash hazard mitigation as it applies to aircraft. This first chapter discusses pertinent background information regarding volcanic emissions and the WRF-Chem model. The second chapter examines the existing capability of WRF-Chem to model the transport and chemical conversion of SO_2 into sulfate aerosols. Chapter 3 discusses the development and addition of a volcanic ash aggregation scheme into WRF-Chem and the improvements it brings for both distal and proximal ash forecasting. Chapter 4 covers the modification of WRF-Chem to serve as a near real-time Volcanic Ash Transport and Dispersion (VATD) model with comparisons to real-time remote sensing operations and observational agency reporting. The dissertation concludes with Chapter 5, which provides an overall summary of the findings of the work, as well as future directions.

1.2 VOLCANIC ASH

Volcanic eruptions emit pyroclastic rock fragments, known as tephra, into the atmosphere. These particles are typically described by their diameter (d) since their atmospheric residence times are a function of their size. Larger bombs (greater than 64 mm diameter) and lapilli (2-64 mm) are removed from the atmosphere rather quickly as their fall velocities are on the order of meters per second (Moore and Peck, 1962; Rose and Durant, 2009; 2011). Volcanic ash particles (less than 2 mm), on the other hand, may be transported many kilometers due to their slow settling velocities (Rose and Durant, 2009; 2011).

To facilitate discussion and study of ash particles, field volcanologists commonly refer to the range of volcanic ash particle sizes from an eruption as a "particle size distribution" (PSD) or "grain size distribution" (GSD). The continuous distribution of particle diameters may span many orders of magnitude. Of particular use is the Φ-scale, developed by Krumbein (1934) which is used to discuss the particle sizes of volcanic ash (Equation 1.2.1) where, 10^{-3} represents a reference diameter of 1 mm and so $2^{-\Phi}$ results in a particle diameter in mm. Table 1.1 lists the sizes that correspond to each Φ bin, ranging from 2 mm to less than 3.9065 μm.

$$10^{-3}e^{-\Phi \ln(2)} \quad (1.2.1)$$

Studies indicate that settling velocities and residence times depend on an ash particles' Stoke's Law drag coefficient, and therefore depend on their geometry and diameter (Brown et al., 2012; Lane et al., 1993; Walker et al., 1971). After an explosive volcanic eruption, small volcanic

ash particles are advected via buoyant hot air and pyroclastic currents while larger ash particles settle to the ground quickly (Rose and Durant, 2009).

Larger ash particles, generally accepted to be greater than 63 μm in diameter (Φ bins 1-6), may be ejected directly from the eruption itself, or may be created during the eruption through aggregation processes where smaller ash particles stick together to form larger, composite ash particles called aggregates (Brown et al., 2012; Rose and Durant, 2009). Observations indicate these aggregation processes are enhanced in the presence of high water vapor concentrations (greater than 8 wt%) and ice (Durant et al., 2008; 2008). As an example, field observations suggest hydrometeor (i.e. hail, sleet, rain) enhanced ash sedimentation increased aggregation rates in the Mount St. Helens, Washington, and Mount Pinatubo, Philippines cases (Durant et al., 2009; Guo et al., 2004). Additionally, grain size studies of tephra fallout from the 2009 eruption of Mount Redoubt, Alaska, USA, showed rapid ash aggregation during the initial phase of the eruption due to the formation of hail and subsequent riming of ash laden water droplets (Van Eaton et al., 2015).

Smaller, "fine ash" particles form the majority of erupted ash (greater than 50 %) and are generally accepted to be less than 63 μm in diameter (Φ bins 7-10) (Brown et al., 2012; Rose and Durant, 2009). While larger particles are removed from a volcanic ash cloud quickly, smaller particles may be entrained in the surrounding air and transported. Due to their smaller size, some of these fine ash particles may remain aloft for quite some time. Fine ash particles of d less than 30 μm, for instance, have terminal settling velocities of up to 10^{-1} m s^{-1}, indicating that they could remain aloft for weeks and thus be transported long distances (Rose and Durant, 2011).

Like their larger counterparts, fine ash particles also aggregate, resulting in larger aggregate particles with faster settling velocities and lower residence lifetimes. These processes involve electrostatic attraction, moist adhesion or the formation of hydrometeors, as is common with larger particles (Gilbert and Lane, 1994; James et al., 2002; Sorem, 1982). Electrostatic aggregation occurs due to the formation of charge separation in volcanic clouds (James et al., 2002). As ash particles are created and rub together in a turbulent plume, charge builds differentially, and eventually causes particles of opposite charge to clump together. This process has been studied in laboratory experiments where volcanic rock was crushed, thus generating an initial charge separation, and aggregate sizes measured (James et al., 2002). Ash aggregates created via electrostatic attraction have been observed in many volcanic eruptions, such as Mount St. Helens

and Redoubt, though characterization of the constituent ash particles remains difficult as these loosely bound clusters tend to break up upon impact with the ground (Carey and Sigurdsson, 1982; Scott and McGimsey, 1994).

Volcanic ash plumes may be observed by a variety of means. Thermal infrared sensors on polar orbiting satellites, such as the Advanced Very High Resolution Radiometer (AVHRR) and the Moderate Resolution Imagining Spectroradiometer (MODIS) are commonly used by Volcanic Ash Advisory Centers (VAACs) to detect and monitor volcanic ash plumes and clouds via split window algorithms (Prata, 1989; Prata and Tupper, 2009). Geostationary satellites with infrared (IR) capable sensors, such as the Advanced Band Imager (ABI) on the Geostationary Environmental Operational Satellite (GOES) and Advanced Himawari Imager (AHI) on Himawari, have relatively high temporal resolution and are therefore particularly useful as they can provide animated imagery of plume movement. Infrared ash detection algorithms use differences in IR absorbance between ash clouds (12 μm) and ice clouds (10 μm) to create temperature contrasts. Ice cloud obfuscation and dust remain limiting factors to the use of these algorithms, though more recent developments in the use of additional channels has brought increased sensitivity (Pavolonis et al., 2006; Pergola et al., 2008; Tupper et al., 2004). Recent advances in hyperspectral algorithms now allow the use of these sensors aboard geostationary satellites such as GOES and Himawari, providing near real time coverage and animated images of volcanic plumes in transport (Pavolonis, 2010; Pavolonis et al., 2013). When volcanic ash is difficult to detect due to a lack of thermal contrast or poor visibility, other volcanic emissions such as SO_2 can be used as proxies for ash as they often travel along with the ash plume (Carn, et al., 2007; Thomas and Prata, 2011; Yang et al., 2010).

In addition to satellite bound remote sensors, volcanic ash has also been measured by other remote sensing, as well as in situ, methods. The eruptive column and initial transport of Mount Redoubt's 2009 plume, for example, was measured by doppler radar (Schneider and Hoblitt, 2013). The 2010 eruption of Eyjafjallajökull was studied extensively by a variety of methods, to include in situ measurements of the plume via airborne collectors and optical particle sizers (Schumann et al., 2011). In addition, high speed camera imagery of falling ash particles as well as field samples of ash fallout were taken in order to better understand aggregation processes (Bonadonna et al., 2011; Taddeucci et al., 2011).

1.3 VOLCANIC SULFUR DIOXIDE

Gaseous volcanic emissions are comprised mostly (approx.. 95 mol%) of water vapor, carbon dioxide (CO_2) and sulfur dioxide (SO_2), with smaller amounts of gasses containing a variety of halide gasses, hydrogen sulfide (H_2S) and carbon monoxide (CO) (Wallace and Edmonds, 2011). These gaseous emissions impact the earth's climate system in various ways, the extent of which is poorly understood (Robock, 2000).

Volcanos emit an estimated 21-25 Tg of SO_2 into the Earth's atmosphere every year from eruptions, therefore making up almost one fifth of the Earth's global SO_2 budget supply (Carn et al., 2017). Sulfur dioxide ultimately converts to sulfate through oxidation with aqueous hydrogen peroxide (H_2O_2) and hydroxyl radicals ($\cdot OH$) (Jacob, 1999; Wayne, 1985). Sulfate aerosols in large quantities have immense negative radiative feedback effects due to their enhancement of atmospheric albedo (Robock, 2000). For example, the large amount of sulfate generated from the 1991 Pinatubo eruption was able to cause a slight offset in the Earth's radiation budget, resulting in a net cooling (Dutton and Christy, 1992; Hansen et al., 1992; Kirchner et al., 1999; Minnis et al., 1993).

Sulfur dioxide, unlike volcanic ash, does not settle unless absorbed by water droplets and removed from the atmosphere as rain. This results in a much larger residence time when compared to ash, and SO_2 can persist in the atmosphere for weeks or months. The SO_2 plume from the 2008 Kasatochi volcanic eruption in Alaska, for example, had a lifetime on the order of days as suggested by remote sensing measurements and computational modeling (Corradini et al., 2010; Egan et al., 2015 (this dissertation); Kristiansen et al., 2010). The resulting SO_2 plume from the 1991 Pinatubo eruption was so large that the resulting SO_2 plume traversed the earth at the equator several times causing a net cooling of the global climate (Bluth et al., 1992; Dutton and Christy, 1992; Hansen et al., 1992; Minnis et al., 1993).

Instead of settling, SO_2 in the atmosphere undergoes a series of conversions, beginning with sulfur in a +4 oxidation state and ending in a +6 state. Despite an energetically favorable oxidation reaction with oxygen, the predominant mode of oxidation is through a reaction with the hydroxyl radical to form sulfate aerosols in the gaseous phase (Equations 1.3.1 – 1.3.3) (Calvert et al., 1985; Calvert and Stockwell, 1983; Wayne, 1985).

$$SO_2 + \cdot OH + M \rightarrow HOSO_2 + M^* \qquad (1.3.1)$$

$$O_2 + HOSO_2 \rightarrow \cdot HO_2 + SO_3 \qquad (1.3.2)$$

$$H_2O + SO_3 \rightarrow H_2SO_4 \qquad (1.3.3)$$

Here, M is a third body quencher, which decreases in concentration with altitude as pressure decreases (Jacob, 1999). Because the hydroperoxy radical (·HO_2) reacts with nitrogen oxide (Equation 1.3.4), this process is catalytic with ·OH being regenerated.

$$HO_2 + NO \rightarrow \cdot OH + NO_2 \qquad (1.3.4)$$

Assuming a steady state hydroxyl radical concentration, which should be the case due to the catalytic nature of the reaction, the loss rate of SO_2 from the gas phase is calculated as follows (Equations 1.3.5 – 1.3.8).

$$\frac{d[SO_2]}{dt} = -k[SO_2][\cdot OH][M] \qquad (1.3.5)$$

$$\frac{d[SO_2]}{[SO_2]} = -k_{m,\cdot OH}dt \qquad (1.3.6)$$

$$\int_{[SO_2]_i}^{[SO_2]_f} \frac{d[SO_2]}{[SO_2]} = \int_0^t -k_{m,\cdot OH}dt \qquad (1.3.7)$$

$$[SO_2]_f = [SO_2]_i e^{-k_{m,\cdot OH}t} \qquad (1.3.8)$$

While ·OH dominates gas phase oxidation of SO_2, aqueous phase reactions include many more oxidants and depend on the gas phase concentration of SO_2, the solubility of SO_2 and gas phase oxidants and the rate of mass transfer of these species between the gas phase and the aqueous phase. Major oxidants in the aqueous phase include ozone (O_3), hydrogen peroxide (H_2O_2), methyl hydrogen peroxide (CH_3O_2H) as well as ·OH and ·HO_2 (Calvert et al., 1985; Wayne, 1985).

Aqueous oxidation of SO_2 begins with the dissolution of SO_2 in water droplets to form the bisulfite anion, HSO_3^- (Equation 1.3.9). Bisulfite further deprotonates to form sulfite (Equation 1.3.10), and in turn, reacts with ·OH and O_3 to form sulfate (Equation 1.3.11). These processes account for the increase in the oxidation state of the sulfur from +4 in SO_2 to +6 in SO_4^{2-}.

$$SO_2 + H_2O \rightleftharpoons H^+ + HSO_3^- \qquad (1.3.9)$$

$$HSO_3^- \rightleftharpoons H^+ + SO_3^{2-} \qquad (1.3.10)$$

$$HSO_3^- + OH^- + O_3 \rightleftharpoons SO_4^{2-} + H_2O + O_2 \qquad (1.3.11)$$

According to Stockwell et al. (1997), the rate constant, k, as well as the solubility of the reactants increases with increasing pH. The oxidation rate of bisulfite with H_2O_2, on the other hand (Equation 1.3.12), decreases with increasing pH, offsetting the increasing solubility of bisulfite and SO_2 (Wayne, 1985).

$$HSO_3^- + H_2O_2 \rightleftharpoons SO_4^{2-} + H_2O \qquad (1.3.12)$$

This difference in solubility lessens the dependence of bisulfite reactions with pH. In addition, H_2O_2 is much more soluble in water than O_3. These observations suggest H_2O_2 is the primary reactant in the production of sulfur +6.

Volcanic SO_2 is observed by various remote sensing platforms. Detection via SO_2 is widely used to detect and quantify SO_2. Sulfur dioxide interacts strongly with many different wavelengths of ultraviolet (UV) radiation between 260 and 320nm. Examples of UV sensors that have been used for SO_2 detection include the Scanning Imaging Absorption Spectrometer for Atmospheric Cartography (SCIAMACHY), the Total Ozone Mapping Spectrometer (TOMS), the Global Ozone Monitoring Experiment (GOME), the hyperspectral Ozone Monitoring Instrument (OMI) and more recently the Tropospheric Monitoring Instrument (TROPOMI) and the Ozone Maping and Profiler Suite (OMPS) (Carn et al., 2007; Carn et al., 2015; Krueger, 1983; Lee et al., 2008; Loyola et al., 2008; Theys et al., 2017; Yang et al., 2007, 2009, 2010). Exploiting strong UV bands also provides information regarding absorption cross-sections and enables calculation of SO_2 column densities. For example, the band residual difference (BRD), linear fit and more recently principal component analysis methods have been used to develop SO_2 column densities from volcanic eruptions (Carn et al., 2008; Li et al., 2013; Wang et al., 2012; Yang et al., 2007, 2009, 2010). Because SO_2 and sulfate aerosols absorb UV radiation differently, UV sensors allow for the differentiation between SO_2 and SO_4^{2-} (Carn, et al., 2007).

While less common, SO_2 may also be detected via infrared sensors by exploiting the symmetric, ν_1, and antisymmetric, ν_3, vibrational bands centered at 1152 cm^{-1} and 1362 cm^{-1}, respectively. In addition, where these IR spectral windows may be closed due to the presence of other compounds in the atmosphere, the weak $\nu_1 + \nu_3$ band at 2500 cm^{-1} may also be exploited. High-resolution, also called "hyperspectral", IR spectrometers have been used to detect SO_2 using these methods, such as the Atmospheric Infrared Sounder (AIRS) and the Infrared Atmospheric Sounding Interferometer (IASI) (Carn et al., 2005; Clarisse et al., 2008). High resolution IR sensors onboard geostationary satellites such as GOES allow for real-time tracking of volcanic ash plumes such as in the eruption of Soufrière Hills Volcano on the island of Montserrat (Ackerman et al., 2018; Prata and Bernardo, 2007). Despite this, IR methods often are hindered if the SO_2 cloud is low in the atmosphere or if there are large clouds or deep convection in the image.

1.4 The Weather Research Forecasting with Chemistry Model

There are many models capable of forecasting volcanic ash dispersion and transport, each with benefits and limitations. Particle dispersion models are computationally cheap and provide quick output when immediate information is needed about the fate of a volcanic cloud (Webley et

al., 2009a, Peterson and Dehn, 2008). These models treat volcanic ash particles as individual tracers and follow their movements along a path tied to the underlying meteorology. Multiple studies have used these models for volcanic ash and SO_2 back trajectory analysis in order to constrain the initial conditions of an eruptive plume (Hirtl et al., 2019; Kristiansen et al., 2010). Some are used as operational Volcanic Ash Transport and Dispersion (VATD) models by VAACs in order to provide public aviation hazard notices. Different agencies chose different types of models to use for these forecasts based on the organization who developed the model. Table 1.2 gives examples of VATD models and their current capabilities. The North Pacific monitoring region currently uses three different VATD models: Puff, used primarily by the US Air Force, the Modèle lagrangien de dispersion de particules d'ordre zéro (MLDP0), used by Canadian agencies, and the Hybrid Single-Particle Lagrangian Integrated Trajectory (HYSPLIT) model used by the US National Weather Service (NWS) and National Oceanic and Atmospheric Administration (NOAA) (Draxler and Hess, 1998; Searcy et al., 1998; Servranckx et al., 1996). The accuracy of these models is limited by various factors, such as uncertainties in eruption source parameters, such as plume height and PSD, and empirically derived assumptions regarding computationally complex problems such as turbulent diffusion and vertical motion (Chen and Servranckx, 2004; Peterson and Dean, 2008). Analysis of the Puff VATD model forecasts generated for the 2001 Mt. Cleveland, Alaska, volcanic eruption showed good agreement between model results and observations from GOES, AVHRR and MODIS (Dean et al., 2004). In a separate case, analysis of the performance of both Puff and HYSPLIT for the 1992 Mt. Spurr, Alaska, volcanic eruption showed a very high dependence on eruption source parameters, with HYSPLIT underestimating ash at lower altitudes (Webley et al., 2009). The 2010 Eyjafjallajökull, Iceland, eruption, due to its costly impacts on the European aviation industry, is a particularly well studied case (Mazzocci et al., 2010). Many of the European VATD models have been assessed, many showing the models to be highly dependent on assumptions of initial conditions and meteorology (Dacre et al., 2016; Grant et al., 2012).

While not yet an operational VATD model, the WRF-Chem model has been adapted to model volcanic ash (Stuefer et al., 2013a). WRF-Chem, like many of the Eulerian VATD models, tracks chemical concentrations in a rectilinear model domain (Skamarock et al., 2005). WRF-Chem is a fully compressible (continuity equation is solved elastically), non-hydrostatic (buoyancy is reflected in the atmosphere) model that includes microphysics and chemistry packages that are

calculated in step with the atmospheric dynamics (Grell et al., 2005). Since these calculations are included in line, there is no interpolation required, unlike other offline models. WRF-Chem has been used in numerous studies to research and forecast volcanic ash and SO_2 transport (Hirtl et al., 2019; Egan et al., 2015; Steensen et al., 2013; Stuefer et al., 2013b; Webley et al., 2012).

WRF-Chem includes ten volcanic ash bins, as well as volcanically generated SO_2 and water vapor emissions. Volcanic plumes are initialized in an umbrella shape above the vent with 75% of the erupted mass in the umbrella plume, and 25% initialized in a linear detrainment underneath. The model initializes the distribution of ash particles into Φ bins as listed in Table 1.1.

The WRF-Chem model, when modeling volcanic emissions (assumed here to contain only ash, water and SO_2), requires certain observations regarding the plumes to be defined in the model such as: volcano latitude and longitude, volcanic vent height (above sea level, A.S.L.), plume top, particle size distribution (PSD), eruption duration, eruption rates for ash, SO_2 and water vapor, and eruption start time and end times. Users may input these parameters into WRF-Chem by two methods. When empirical knowledge of a volcanic eruption is unavailable, such as in an operational forecasting setting where satellite products may not yet be available, ash and SO_2 may be initialized into the WRF-Chem model through binary files generated by the Prep-Chem-Src chemistry initialization package (Freitas et al., 2011). In place of observed plume parameters, Prep-Chem-Src utilizes a lookup table that includes the most common Eruption Source Parameters (ESPs) for all of the world's known volcanoes, which were developed using a combination of historical data and assumptions regarding volcanic magma composition (Mastin et al., 2009). In cases where empirical knowledge of a current or past eruption is available, the model can be initialized with specific initial plume conditions. Plume height, eruption rate (specified in minute intervals), PSD and eruption start time may all be explicitly specified.

WRF also requires meteorological initial conditions to drive the model. The simulations conducted in this dissertation will use meteorology fields generated by the National Center for Environmental Prediction (NCEP). Three of NCEP's products will be used, depending on the case. NCEP's Final Reanalysis (FNL) product will be used to simulate large, continental size domains (see Chapter 3 in the case of Eyjafjallajökull volcano). While the FNL product comes in a variety of resolutions, we use a relatively coarse domain resolution of 1° by 1°, minimizing file size requirements. In addition, higher resolution runs are available from 2015 onward, so past

simulations are constrained to the coarser resolutions. FNL products contain meteorology fields generated by the same model used in the Global Forecast System (GFS), providing unlimited domain range, but it is initialized over an hour later than GFS, allowing more observation data to be used (Saha et al., 2010). The North American Regional Reanalysis (NARR) product, also generated by NCEP, provides relatively high-resolution meteorological fields at 0.3° by 0.3° at the equatorial latitudes and covers the North American continent (See Chapter 2 in the case of Kasatochi volcano) (ESRL, 2016). For forecasting volcanic plumes, NCEP's Global Forecast System product is used. A table of these products, their respective NCEP dataset names, spatial resolutions and temporal resolutions are provided below in Table 1.3. All of these datasets are available via archive at the University Center for Atmospheric Research (UCAR) Computational and Information Systems Lab (CISL).

The WRF model also requires geographic information such as soil information (affecting planetary boundary layer dynamics), snow and vegetation cover (affecting surface albedo), ocean temperatures and more, provided by the United States Geologic Survey Land Cover dataset (USGS, 2016). Using the parameters provided, the atmospheric sinks of volcanic ash and SO_2 are also reflected in the model chemistry calculations. The settling of volcanic ash is calculated using the Stoke's Law for each tracer (ash particle) as a function of their density and effective radius, the dynamic viscosity of the system and the acceleration due to gravity. A growth factor of three (applied to the effective diameter) is included to increase the radius of the particles when relative humidity exceeds 100%. Volcanic SO_2 sinks may be calculated by various chemistry packages. For example, WRF-Chem includes chemistry routines for the conversion of atmospheric SO_2 via the Regional Acid Deposition Model which follows the first order kinetics of SO_2 oxidation mentioned above (Chang, 1991; Grell et al., 2005; Stockwell et al., 1997).

1.5 Assessment and Changes to WRF-Chem in Volcanic Emissions Modeling

The following chapters of this dissertation are divided into 3 independent works, Chapters 2, 3 and 4, along with closing remarks and conclusions in Chapter 5. Chapter 2, WRF-Chem modeling of sulfur dioxide emissions from the 2008 Eruption of Kasatochi Volcano, details modeling of sulfur dioxide emissions from the eruptions of Kasatochi Volcano in 2008 using WRF-Chem. Here, model output is compared to remote sensing data and comments are made on

the ability of WRF-Chem to capture the evolution and transport of the SO_2 cloud. The work in Chapter 2 has been published in Annals of Geophysics in 2015.

Chapter 3, Modeling volcanic ash aggregation processes and related impacts on the April/May 2010 eruptions of Eyjafjallajökull Volcano with WRF-Chem, covers the addition of a volcanic ash aggregation scheme to the WRF-Chem base code. Comments are provided on changes in the model performance, the affects of the new code on model output, and an assessment of the model's ability to capture the dispersion of ash clouds from the 2010 eruptions of Eyjafjallajökull in Iceland. This work has be submitted for publication in Natural Hazards and Earth System Sciences in November, 2019.

Chapter 4, Near Real-Time Volcanic Ash Forecasting with the Weather Research Forecasting with Chemistry (WRF-Chem) Model, suggests a methodology for using WRF-Chem as an automated, near real-time tool. The code is modified such that 10 different volcanic ash fields are available from one simulation run, greatly reducing the model run time. This work is intended to be submitted for publication in the Spring of 2020.

TABLES

Table 1.1 – Volcanic ash Φ bin distribution and corresponding bin number. Values are based on Equation 1.2.1, developed by Krumbein (1934)

Bin #	ϕ	Size
1	<0	1-2 mm
2	0-1	0.5-1 mm
3	1-2	0.25-0.5 mm
4	2-3	125-250 μm
5	3-4	62.5-125 μm
6	4-5	31.25-62.5 μm
7	5-6	15.625-31.25 μm
8	6-7	7.8125-15.625 μm
9	7-8	3.9065-7.8125 μm
10	>8	<3.9065 μm

Table 1.2 – Volcanic Ash Transport and Dispersion (VATD) currently in use in research and operational settings

Model Name:	ASH3D	ATHAM	FALL3D	FLEXPART	HYSPLIT	NAME	PUFF	WRF
Operational	X		X	X	X	X	X	
Topography	X	X	X	X	X	X	X	X
U advection	X	X	X	X	X	X	X	X
V advection	X	X	X	X	X	X	X	X
U diffusion	X	X	X	X	X	X	X	X
V diffusion	X	X	X	X	X	X	X	X
Sedimentation	X	X	X	X	X	X	X	X
Aggregation			X					
Chemistry		X	X	X	X	X		X
Fully Coupled								X

Table 1.3 – Atmospheric model data used in WRF-Chem studies

Product Name	Dataset ID	Spatial Resolution	Temporal Resolution	Chapters Used
NCEP FNL	ds083.2	1° by 1°	6 hourly	3, 4
NCEP GFS	ds084.1	0.3° by 0.3°	3 hourly	4
NCEP NARR	ds608.0	0.25° by 0.25°	3 hourly	2

REFERENCES

Aponte, C., de Groot, W. J. and Wotton, B. M.: Forest fires and climate change: causes, consequences and management options, Int. J. Wildland Fire, 25(8), doi:10.1071/WFv25n8_FO, 2016.

Artemieva, N. and Morgan, J.: Quantifying the Release of Climate-Active Gasses by Large Meteorite Impacts With a Case Study of Chicxulub, Geophys. Res. Lett., 44(20), doi:10.1002/2017GL074879, 2017.

Bluth, G. J. S., Doiron, S. D., Schnetzler, C. C., Krueger, A. J. and Walter, L. S.: Global tracking of the SO2 clouds from the June, 1991 Mount Pinatubo eruptions, Geophys. Res. Lett., 19(2), 151–154, doi:10.1029/91GL02792, 1992.

Brown, P., ReVelle, D. O., Silber, E. A., Edwards, W. N., Arrowsmith, S., Jackson, L. E., Tancredi, G. and Eaton, D.: Analysis of a crater-forming meteorite impact in Peru, J. Geophys. Res. Planets, 113(E9), doi:10.1029/2008JE003105, 2008.

Brown, R. J., Bonadonna, C. and Durant, A. J.: A review of volcanic ash aggregation, Phys. Chem. Earth Parts ABC, 45–46, 65–78, doi:10.1016/j.pce.2011.11.001, 2012.

Calvert, J. G. and Stockwell, W. R.: Acid generation in the troposphere by gas-phase chemistry, Environ. Sci. Technol., 17(9), 428A-443A, doi:10.1021/es00115a727, 1983.

Calvert, J. G., Lazrus, A., Kok, G. L., Heikes, B. G., Walega, J. G., Lind, J. and Cantrell, C. A.: Chemical mechanisms of acid generation in the troposphere, Nature, 317(6032), 27–35, doi:10.1038/317027a0, 1985.

Carey, S. N. and Sigurdsson, H.: Influence of particle aggregation on deposition of distal tephra from the May 18, 1980, eruption of Mount St. Helens volcano, J. Geophys. Res. Solid Earth, 87(B8), 7061–7072, doi:10.1029/JB087iB08p07061, 1982.

Carn, S. A., Strow, L. L., Souza-Machado, S. de, Edmonds, Y. and Hannon, S.: Quantifying tropospheric volcanic emissions with AIRS: The 2002 eruption of Mt. Etna (Italy), Geophys. Res. Lett., 32(2), L02301, doi:10.1029/2004GL021034, 2005.

Carn, S. A., Krotkov, N. A., Yang, K., Hoff, R. M., Prata, A. J., Krueger, A. J., Loughlin, S. C. and Levelt, P. F.: Extended observations of volcanic SO2 and sulfate aerosol in the stratosphere, Atmospheric Chem. Phys. Discuss., 7(1), 2857–2871, 2007a.

Carn, S. A., Krueger, A. J., Krotkov, N. A., Yang, K. and Levelt, P. F.: Sulfur dioxide emissions from Peruvian copper smelters detected by the Ozone Monitoring Instrument, Geophys. Res. Lett., 34(9), L09801, doi:10.1029/2006GL029020, 2007b.

Carn, S. A., Krotkov, N. A., Fioletov, V., Yang, K., Krueger, A. J. and Tarasick, D.: Emission, transport and validation of sulfur dioxide in the 2008 Okmok and Kasatochi eruption clouds, in AGU Fall Meeting Abstracts, vol. 1, p. 07, 2008.

Casadevall, T. J.: Volcanic Haazards and Aviation Safety: Lessons of the Past Decade, United States Geological Survey, 1992.

Chang, J. S.: The regional acid deposition model and engineering model, National Acid Precipitation Assessment Program, Office of the Director., 1991.

Chen, P. and Servranckx, R.: Modeling Volcanic Ash Transport and Dispersion: Expectations and Reality, 2004.

Church, J. A., White, N. J. and Arblaster, J. M.: Significant decadal-scale impact of volcanic eruptions on sea level and ocean heat content, Nature, 438, 74-77, doi:10.1038/nature04237

Clarisse, L., Coheur, P. F., Prata, A. J., Hurtmans, D., Razavi, A., Phulpin, T., Hadji-Lazaro, J. and Clerbaux, C.: Tracking and quantifying volcanic SO2 with IASI, the September 2007 eruption at Jebel at Tair, Atmos Chem Phys, 8(24), 7723–7734, 2008.

Coldwell, B. C. and Pankhurst, M. J.: Evaluating the influence of meteorite impact events on global potassium feldspar availability to the atmosphere since 600 Ma, G. Geol. Soc., 176(2), doi:10.1144/jgs2018-084, 2018.

Corradini, S., Merucci, L., Prata, A. J. and Piscini, A.: Volcanic ash and SO2 in the 2008 Kasatochi eruption: Retrievals comparison from different IR satellite sensors, J. Geophys. Res. Atmospheres, 115(D2), doi:10.1029/2009JD013634, 2010.

Crowley, T. J., Zielinski, G., Vinther, B., Udisti, R., Kreutz, K., Cole-dai, J., Castellano, E., Ejòfs, S., Bnqmjuvef, J. U., Ujnf, B. and Uibu, J.: on Volcanism and the Little Ice Age., n.d.

Dacre, H. F., Harvey, N. J., Webley, P. W. and Morton, D.: How accurate are volcanic ash simulations of the 2010 Eyjafjallajökull eruption?, J. Geophys. Res. Atmospheres, 121(7), 2015JD024265, doi:10.1002/2015JD024265, 2016.

Davis DL: A Look Back at the London Smog of 1952 and the Half Century Since, Environ. Health Perspect., 110(12), A734–A735, doi:10.1289/ehp.110-a734, 2002.

Dean, K. G., Dehn, J., Papp, K. R., Smith, S., Izbekov, P., Peterson, R., Kearney, C. and Steffke, A.: Integrated satellite observations of the 2001 eruption of Mt. Cleveland, Alaska, J. Volcanol. Geotherm. Res., 135(1–2), 51–73, doi:10.1016/j.jvolgeores.2003.12.013, 2004.

Draxler, R. R. and Hess, G. D.: An overview of the HYSPLIT_4 modelling system for trajectories, Aust. Meteorol. Mag., 47(4), 295–308, 1998.

Durant, A. J., Shaw, R. A., Rose, W. I., Mi, Y. and Ernst, G. G. J.: Ice nucleation and overseeding of ice in volcanic clouds, J. Geophys. Res. Atmospheres, 113(D9), D09206, doi:10.1029/2007JD009064, 2008.

Durant, A. J., Rose, W. I., Sarna-Wojcicki, A. M., Carey, S. and Volentik, A. C. M.: Hydrometeor-enhanced tephra sedimentation: Constraints from the 18 May 1980 eruption of Mount St. Helens, J. Geophys. Res. Solid Earth, 114(B3), 2009.

Dutton, E. G. and Christy, J. R.: Solar radiative forcing at selected locations and evidence for global lower tropospheric cooling following the eruptions of El Chichón and Pinatubo, Geophys. Res. Lett., 19(23), 2313–2316, doi:10.1029/92GL02495, 1992.

Egan, S. D., Stuefer, M., Webley, P., Cahill, C. F. and Dehn, J.: WRF-Chem modeling of sulfur dioxide emissions from the 2008 Kasatochi Volcano, Ann. Geophys., 57(0), doi:10.4401/ag-6626, 2015.

Emmanuel, S. C.: Impact to lung health of haze from forest fires: The Singapore experience, Respirology, 5(2), 175-182, doi:10.1046/j.1440-1843.2000.00247.x, 2001.

ESRL: NCEP North American Regional Reanalysis (NARR), [online] Available from: http://www.esrl.noaa.gov/psd/data/gridded/data.narr.html (Accessed 20 November 2016), 2016.

Flannigan, M. D., Stocks, B. J. and Wotton, B. M.: Climate change and forest fires, Sci. Total Environ., 262(3), doi:10.1016/S0048-9697(00)00524-6, 2000.

Francesco, S. R., Chafik, L., Caballero, R. and Battisti, D. S.: Impacts of high-latitude volcanic eruptions on ENSO and AMOC, Proc. Natl. Acad. Sci. U.S.A., 112(45), 13784-13788, doi:10.1073/pnas.1509153112, 2015.

Freitas, S. R., Longo, K. M., Alonso, M. F., Pirre, M., Marecal, V., Grell, G., Stockler, R., Mello, R. F. and Gácita, M. S.: PREP-CHEM-SRC–1.0: a preprocessor of trace gas and aerosol emission fields for regional and global atmospheric chemistry models, Geosci. Model Dev., 4(2), 419–433, 2011.

Gilbert, J. S. and Lane, S. J.: The origin of accretionary lapilli, Bull. Volcanol., 56(5), 398–411, doi:10.1007/BF00326465, 1994.

Graf, H.-F., Feichter, J. and Langmann, B.: Volcanic sulfur emissions: Estimates of source strength and its contribution to the global sulfate distribution, J. Geophys. Res. Atmospheres, 102(D9), 10727–10738, doi:10.1029/96JD03265, 1997.

Grant, A. L. M., Dacre, H. F., Thomson, D. J. and Marenco, F.: Horizontal and vertical structure of the Eyjafjallajökull ash cloud over the UK: a comparison of airborne lidar observations and simulations, Atmos Chem Phys, 12(21), 10145–10159, doi:10.5194/acp-12-10145-2012, 2012.

Grell, G. A., Peckham, S. E., Schmitz, R., McKeen, S. A., Frost, G., Skamarock, W. C. and Eder, B.: Fully coupled "online" chemistry within the WRF model, Atmos. Environ., 39(37), 6957–6975, doi:10.1016/j.atmosenv.2005.04.027, 2005.

Guo, S., Rose, W. I., Bluth, G. J. S. and Watson, I. M.: Particles in the great Pinatubo volcanic cloud of June 1991: The role of ice, Geochem. Geophys. Geosystems, 5(5), Q05003, doi:10.1029/2003GC000655, 2004.

Hansen, J., Lacis, A., Ruedy, R. and Sato, M.: Potential climate impact of Mount Pinatubo eruption, Geophys. Res. Lett., 19(2), 215–218, 1992.

Hirtl, M., Stuefer, M., Arnold, D., Grell, G., Maurer, C., Natali, S., Scherllin-Pirscher, B. and Webley, P.: The effects of simulating volcanic aerosol radiative feedbacks with WRF-Chem during the Eyjafjallajökull eruption, April and May 2010, Atmos. Environ., 198, 194–206, doi:10.1016/j.atmosenv.2018.10.058, 2019.

Holmes, N. S. and Morawska, L.: A review of dispersion modelling and its application to the dispersion of particles: An overview of different dispersion models available, Atmos. Environ., 40(30), 5902–5928, doi:10.1016/j.atmosenv.2006.06.003, 2006.

Hunt, J. C. R.: Lewis Fry Richardson and his contributions to mathematics, meteorology, and models of conflict, Annu. Rev. Fluid Mech., 30, 13-35, doi:10.1146/annurev.fluid.30.1.0, 1998.

Jacob, D.: Introduction to atmospheric chemistry, Princeton University Press, 1999.

Jacobson, M. Z.: Fundamentals of atmospheric modeling, 2nd ed., Cambridge university press., 2005.

James, M. R., Gilbert, J. S. and Lane, S. J.: Experimental investigation of volcanic particle aggregation in the absence of a liquid phase, J. Geophys. Res. Solid Earth, 107(B9), 2191, doi:10.1029/2001JB000950, 2002.

Jung, J., Lyu, Y., Lee, M., Hwang, T., Lee, S. and Oh S.: Impact of Siberian forest fires on the atmosphere over the Korean Peninsula during summer 2014, Atmos. Chem. Phys., 16(11), 6757-6770, doi:10.5194/acp-16-6757-2016, 2016.

Kedia, S., Kumar, R., Islam, S., Sathe, Y. and Kaginalkar, A.: Radiative impact of a heavy dust storm over Inda and surrounding oceanic regions, Atmos. Environ., 185, 109-120, doi:10.1016/j.atmosenv.2018.05.005, 2018.

Kelly, P. M. and Sear, C. B.: Climatic impacts of explosive volcanic eruptions, Nature, 311, 740-743, doi:10.1038/311740a0, 1984.

Kirchner, I., Stenchikov, G. L., Graf, H.-F., Robock, A. and Antuña, J. C.: Climate model simulation of winter warming and summer cooling following the 1991 Mount Pinatubo volcanic eruption, J. Geophys. Res. Atmospheres 1984–2012, 104(D16), 19039–19055, 1999.

Kristiansen, N. I., Stohl, A., Prata, A. J., Richter, A., Eckhardt, S., Seibert, P., Hoffmann, A., Ritter, C., Bitar, L., Duck, T. J. and Stebel, K.: Remote sensing and inverse transport modeling of the Kasatochi eruption sulfur dioxide cloud, J. Geophys. Res., 115(D2), D00L16, doi:10.1029/2009JD013286, 2010.

Krueger, A. J.: Sighting of El Chichon Sulfur Dioxide Clouds with the Nimbus 7 Total Ozone Mapping Spectrometer, Science, 220, 1983.

Krumbein, W. C.: Size frequency distributions of sediments, J. Sediment. Res., 4(2) [online] Available from: http://archives.datapages.com/data/sepm/journals/v01-32/data/004/004002/0065.htm (Accessed 24 April 2016), 1934.

Lane, S. J., Gilbert, J. S. and Hilton, M.: The aerodynamic behaviour of volcanic aggregates, Bull. Volcanol., 55(7), 481–488, doi:10.1007/BF00304591, 1993.

Lee, C., Richter, A., Lee, H., Kim, Y. J., Burrows, J. P., Lee, Y. G. and Choi, B. C.: Impact of transport of sulfur dioxide from the Asian continent on the air quality over Korea during May 2005, Atmos. Environ., 42(7), 1461–1475, doi:10.1016/j.atmosenv.2007.11.006, 2008.

Loyola, D., Van Geffen, J., Valks, P., Erbertseder, T., Van Roozendael, M., Thomas, W., Zimmer, W. and Wißkirchen, K.: Satellite-based detection of volcanic sulphur dioxide from recent eruptions in Central and South America, Adv. Geosci., 14, 35–40, 2008.

Lynch, P.: The origins of computer weather prediction and climate modeling, J. Comput. Phys., 227(7), 3431-3444, 2008.

Manktelow, P. T., Carlaw, K. S., Mann, G. W. and Spracklen, D. V.: The impact of dust on sulfate aerosol, CN and CCN during an East Asian dust storm, Atmos. Chem. Phys., 10, 365-382, 2010.

Mastin, L. G., Guffanti, M., Servranckx, R., Webley, P., Barsotti, S., Dean, K., Durant, A., Ewert, J. W., Neri, A., Rose, W. I., Schneider, D., Siebert, L., Stunder, B., Swanson, G., Tupper, A., Volentik, A. and Waythomas, C. F.: A multidisciplinary effort to assign realistic source parameters to models of volcanic ash-cloud transport and dispersion during eruptions, J. Volcanol. Geotherm. Res., 186(1–2), 10–21, doi:10.1016/j.jvolgeores.2009.01.008, 2009.

Miller, T. P., Casadevall, T. J. and others: Volcanic ash hazards to aviation, Encycl. Volcanoes, 915–930, 2000.

Minnis, P., Harrison, E. F., Stowe, L. L., Gibson, G. G., Denn, F. M., Doelling, D. R. and Smith, W. L.: Radiative climate forcing by the Mount Pinatubo eruption, Science, 259(5100), 1411–1415, 1993.

Moore, J. G. and Peck, D. L.: Accretionary Lapilli in Volcanic Rocks of the Western Continental United States, J. Geol., 70(2), 182–193, 1962.

Pavolonis, M. J.: Advances in Extracting Cloud Composition Information from Spaceborne Infrared Radiances—A Robust Alternative to Brightness Temperatures. Part I: Theory, J. Appl. Meteorol. Climatol., 49(9), 1992–2012, doi:10.1175/2010JAMC2433.1, 2010.

Pavolonis, M. J., Feltz, W. F., Heidinger, A. K. and Gallina, G. M.: A Daytime Complement to the Reverse Absorption Technique for Improved Automated Detection of Volcanic Ash, J. Atmospheric Ocean. Technol., 23(11), 1422–1444, doi:10.1175/JTECH1926.1, 2006.

Pavolonis, M. J., Heidinger, A. K. and Sieglaff, J.: Automated retrievals of volcanic ash and dust cloud properties from upwelling infrared measurements, J. Geophys. Res. Atmospheres, 118(3), 1436–1458, doi:10.1002/jgrd.50173, 2013.

Pergola, N., Marchese, F., Tramutoli, V., Filizzola, C. and Ciampa, M.: Advanced satellite technique for volcanic activity monitoring and early warning, [online] Available from: http://www.earth-prints.org/handle/2122/4992 (Accessed 1 July 2019), 2008.

Peterson, R. A. and Dean, K. G.: Forecasting exposure to volcanic ash based on ash dispersion modeling, J. Volcanol. Geotherm. Res., 170(3–4), 230–246, doi:10.1016/j.jvolgeores.2007.10.003, 2008.

Prata, A. J.: Infrared radiative transfer calculations for volcanic ash clouds, Geophys. Res. Lett., 16(11), 1293–1296, 1989.

Prata, A. J. and Tupper, A.: Aviation hazards from volcanoes: the state of the science, Nat. Hazards, 51(2), 239–244, doi:10.1007/s11069-009-9415-y, 2009.

Robock, A.: Volcanic eruptions and climate, Rev. Geophys., 38(2), 191–219, doi:10.1029/1998RG000054, 2000.

Rose, W. I. and Durant, A. J.: Fine ash content of explosive eruptions, J. Volcanol. Geotherm. Res., 186, 32–39, doi:10.1016/j.jvolgeores.2009.01.010, 2009.

Saha, S., Moorthi, S., Pan, H.-L., Wu, X., Wang, J., Nadiga, S., Tripp, P., Kistler, R., Woollen, J., Behringer, D., Liu, H., Stokes, D., Grumbine, R., Gayno, G., Wang, J., Hou, Y.-T., Chuang, H.-Y., Juang, H.-M. H., Sela, J., Iredell, M., Treadon, R., Kleist, D., Van Delst, P., Keyser, D., Derber, J., Ek, M., Meng, J., Wei, H., Yang, R., Lord, S., Van Den Dool, H., Kumar, A., Wang, W., Long, C., Chelliah, M., Xue, Y., Huang, B., Schemm, J.-K., Ebisuzaki, W., Lin, R., Xie, P., Chen, M., Zhou, S., Higgins, W., Zou, C.-Z., Liu, Q., Chen, Y., Han, Y., Cucurull, L., Reynolds, R. W., Rutledge, G. and Goldberg, M.: The NCEP Climate Forecast System Reanalysis, Bull. Am. Meteorol. Soc., 91(8), 1015–1057, doi:10.1175/2010BAMS3001.1, 2010.

Schneider, D. J. and Hoblitt, R. P.: Doppler weather radar observations of the 2009 eruption of Redoubt Volcano, Alaska, J. Volcanol. Geotherm. Res., 259, 133–144, doi:10.1016/j.jvolgeores.2012.11.004, 2013.

Schumann, U., Weinzierl, B., Reitebuch, O., Schlager, H., Minikin, A., Forster, C., Baumann, R., Sailer, T., Graf, K., Mannstein, H., Voigt, C., Rahm, S., Simmet, R., Scheibe, M., Lichtenstern, M., Stock, P., Ruba, H., Schauble, D., Tafferner, A., Rautenhaus, M., Gerz, T., Ziereis, H., Krautstrunk, M., Mallaun, C., Gayet, J. F., Lieke, K., Kandler, K., Ebert, M., Weinbruch, S., Stohl, A., Gasteiger, J., Gross, S., Freudenthaler, V., Wiegner, M., Ansmann, A., Tesche, M., Ólafsson, H. and Sturm, K.: Airborne observations of the Eyjafjalla volcano ash cloud over Europe during air space closure in April and May 2010, Atmos Chem Phys, 11(5), 2245–2279, 2011.

Scott, W. E. and McGimsey, R. G.: Character, mass, distribution, and origin of tephra-fall deposits of the 1989–1990 eruption of redoubt volcano, south-central Alaska, J. Volcanol. Geotherm. Res., 62(1–4), 251–272, doi:10.1016/0377-0273(94)90036-1, 1994.

Searcy, C., Dean, K. and Stringer, W.: PUFF: A high-resolution volcanic ash tracking model, J. Volcanol. Geotherm. Res., 80(1), 1–16, 1998.

Servranckx, R., D'Amours, R., Jean, M., Toviessi, J.-P. and Trudel, S.: Volcanic ash forecasting at the Canadian Meteorological Centre, Environ. Emerg. Response Div. Environ. Can. Present. Publ. Pan Pac. Hazards, 96, 1996.

Sigurdsson, H.: Assessment of the atmospheric impact of volcanic eruptions, Geol. Soc. Am. Spec. Pap., 247, 99-110, 1990.

Skamarock, W. C., Klemp, J. B., Dudhia, J., Gill, D. O., Barker, D. M., Wang, W. and Powers, J. G.: A Description of the Advanced Research WRF Version 2., 2005.

Slingo, A., Ackerman, T. P., Allan, R. P., Kassianov, E. I., McFarlane, S. A., Robinson, G. J., Barnard, J. C., Miller, M. A., Harries, J. E., Russell, J. E. and Dewitte, S.: Observations of the impact of a major Saharan dust storm on the atmospheric radiation balance, Geophys. Res. Lett., 33(24), doi: 10.1029/2006GL027869, 2006.

Sorem, R. K.: Volcanic ash clusters: Tephra rafts and scavengers, J. Volcanol. Geotherm. Res., 13(1), 63–71, doi:10.1016/0377-0273(82)90019-1, 1982.

Steensen, T., Stuefer, M., Webley, P., Grell, G. and Freitas, S.: Qualitative comparison of Mount Redoubt 2009 volcanic clouds using the PUFF and WRF-Chem dispersion models and satellite remote sensing data, J. Volcanol. Geotherm. Res., 259, 235–247, doi:10.1016/j.jvolgeores.2012.02.018, 2013.

Stockwell, W. R., Kirchner, F., Kuhn, M. and Seefeld, S.: A new mechanism for regional atmospheric chemistry modeling, J. Geophys. Res. Atmospheres, 102(D22), 25847–25879, doi:10.1029/97JD00849, 1997.

Stuefer, M., Freitas, S. R., Grell, G., Webley, P., Peckham, S., McKeen, S. A. and Egan, S. D.: Inclusion of ash and SO 2 emissions from volcanic eruptions in WRF-Chem: development and some applications, Geosci. Model Dev., 6(2), 457–468, doi:doi.org/10.5194/gmd-6-457-2013, 2013a.

Stuefer, M., Freitas, S. R., Grell, G., Webley, P., Peckham, S., McKeen, S. A. and Egan, S. D.: Inclusion of ash and SO2 emissions from volcanic eruptions in WRF-Chem: development and some applications, Geosci Model Dev, 6(2), 457–468, doi:10.5194/gmd-6-457-2013, 2013b.

Taddeucci, J., Scarlato, P., Montanaro, C., Cimarelli, C., Bello, E. D., Freda, C., Andronico, D., Gudmundsson, M. T. and Dingwell, D. B.: Aggregation-dominated ash settling from the Eyjafjallajökull volcanic cloud illuminated by field and laboratory high-speed imaging, Geology, 39(9), 891–894, doi:10.1130/G32016.1, 2011.

Thomas, H. E. and Prata, A. J.: Sulphur dioxide as a volcanic ash proxy during the April–May 2010 eruption of Eyjafjallajökull volcano, Iceland, Atmos Chem Phys, 11(14), 6871–6880, 2011.

Toon, O. B.: Sudden Changes in Atmospheric Composition and Climate, Patt. Chan. Earth Evol., 41-61, doi:10.1007/978-3-642-69317-5_4, 1984.

Tupper, A., Carn, S., Davey, J., Kamada, Y., Potts, R., Prata, F. and Tokuno, M.: An evaluation of volcanic cloud detection techniques during recent significant eruptions in the western 'Ring of Fire,' Remote Sens. Environ., 91(1), 27–46, doi:10.1016/j.rse.2004.02.004, 2004.

USGS: Land Cover Institute (LCI) Land Cover Datasets, [online] Available from: http://landcover.usgs.gov/landcoverdata.php (Accessed 20 November 2016), 2016.

Van Eaton, A. R., Mastin, L. G., Herzog, M., Schwaiger, H. F., Schneider, D. J., Wallace, K. L. and Clarke, A. B.: Hail formation triggers rapid ash aggregation in volcanic plumes, Nat. Commun., 6, doi:10.1038/ncomms8860, 2015.

Walker, G. P. L., Wilson, L. and Bowell, E. L. G.: Explosive Volcanic Eruptions—I The Rate of Fall of Pyroclasts, Geophys. J. Int., 22(4), 377–383, doi:10.1111/j.1365-246X.1971.tb03607.x, 1971.

Wallace, P. J. and Edmonds, M.: The Sulfur Budget in Magmas: Evidence from Melt Inclusions, Submarine Glasses, and Volcanic Gas Emissions, Rev. Mineral. Geochem., 73(1), 215–246, doi:10.2138/rmg.2011.73.8, 2011.

Wang, J., Park, S., Zeng, J., Yang, K., Carn, S., Krotkov, N. and Omar, A. H.: Modeling of 2008 Kasatochi volcanic sulfate direct radiative forcing: assimilation of OMI SO_2 plume height data and comparison with MODIS and CALIOP observations, Atmospheric Chem. Phys. Discuss., 12(10), 26435–26475, doi:10.5194/acpd-12-26435-2012, 2012.

Wayne, R. P.: Chemistry of atmospheres, 3rd ed., Oxford University Press., 2000.

Webley, P. W., Dehn, J., Lovick, J., Dean, K. G., Bailey, J. E., Valcic, L.: Near-real-time volcanic ash cloud detection: Experiences from the Alaska Volcano Observatory, J. Volcanol. Geoth. Res., 186(1,2), 79-90, doi:10.1016/j.jvolgeores.2009.02.010, 2009a.

Webley, P. W., Stunder, B. J. B. and Dean, K. G.: Preliminary sensitivity study of eruption source parameters for operational volcanic ash cloud transport and dispersion models — A case study of the August 1992 eruption of the Crater Peak vent, Mount Spurr, Alaska, J. Volcanol. Geotherm. Res., 186(1–2), 108–119, doi:10.1016/j.jvolgeores.2009.02.012, 2009b.

Webley, P. W., Steensen, T., Stuefer, M., Grell, G., Freitas, S. and Pavolonis, M.: Analyzing the Eyjafjallajökull 2010 eruption using satellite remote sensing, lidar and WRF-Chem dispersion and tracking model, J. Geophys. Res., 117, D00U26, 2012.

Yang, K., Krotkov, N. A., Krueger, A. J., Carn, S. A., Bhartia, P. K. and Levelt, P. F.: Retrieval of large volcanic SO2 columns from the Aura Ozone Monitoring Instrument: Comparison and limitations, J. Geophys. Res., 112(D24), D24S43, doi:10.1029/2007JD008825, 2007.

Yang, K., Krotkov, N. A., Krueger, A. J., Carn, S. A., Bhartia, P. K. and Levelt, P. F.: Improving retrieval of volcanic sulfur dioxide from backscattered UV satellite observations, Geophys. Res. Lett., 36(3), L03102, doi:10.1029/2008GL036036, 2009.

Yang, K., Liu, X., Bhartia, P. K., Krotkov, N. A., Carn, S. A., Hughes, E. J., Krueger, A. J., Spurr, R. J. D. and Trahan, S. G.: Direct retrieval of sulfur dioxide amount and altitude from spaceborne hyperspectral UV measurements: Theory and application, J. Geophys. Res. Atmospheres, 115(D2), n/a–n/a, doi:10.1029/2010JD013982, 2010.

Zhuang, G., Guo, J., Yuan, H. and Zhau, C.: The compositions, sources and size distribution of the dust storm from China in spring of 2000 and its impact on the global environment, Chinese Sci. Bull., 46(11), 895-900, doi:10.1007/BF02900460, 2000.

CHAPTER 2* - WRF-CHEM MODELING OF SULFUR DIOXIDE EMISSIONS FROM THE 2008 ERUPTION OF KASATOCHI VOLCANO

*Published as Egan, S. D., Stuefer, M., Webley, P. and Cahill, C. F.: Annals of Geophysics, Volume 57, doi:10.4401/ag-6626, 2015

ABSTRACT

We simulate the dispersion and chemical evolution of the sulfur dioxide (SO_2) plume following the eruption of Kasatochi Volcano in Alaska, USA, on August 7th, 2008 with the Weather Research Forecasting with Chemistry (WRF-Chem) model. The model was initialized with the observed three distinct plumes, which were characterized by a total estimated SO_2 mass of 0.5 to 2.7 Tg. WRF-Chem modeled output was compared to remote sensing retrievals from the Ozone Monitoring Instrument (OMI), and the modeled plumes agreed well in shape and location with the OMI retrievals. The calculated SO_2 column densities showed comparable Dobson Unit values with higher densities especially in the center of the distal plume over northern Canada. We concluded from our analysis that WRF-Chem derived a 9.1-day lifetime of the SO_2 when initialized with a 12km eruption height. Sensitivity tests with varying eruption plume heights revealed significantly increased lifetimes of SO_2 up to 17.1 days for higher plumes.

2.1 INTRODUCTION

Kasatochi volcano [52.169°N, 175.511°W] is a small (2.7 x 3.3 km, 314 m above sea level, a.s.l.), uninhabited stratovolcano in the Aleutian Arc of Alaska (Scott et al., 2010). On August 2nd, 2008 US Fish and Wildlife biologists reported small tremors and a sulfur odor while on assignment (Waythomas et al., 2010). They were evacuated prior to a M5.8 earthquake on August 7th, 2008 at 2:00 pm AKDT (22:00 UTC), detected by instruments from the Great Sitkin seismic Network. Infrared satellite retrievals from the Advanced Very High Resolution Radiometer (AVHRR) confirmed the presence of a volcanic plume situated over the volcano's vent during this time (Waythomas et al., 2010).

Two additional eruptions followed at 01:50 UTC and 04:35 UTC (Scott et al., 2010). The ash and SO_2 emissions dispersed in a complex pattern due in large part to a low-pressure cyclogenesis situated nearly on top of the volcano (Krotkov et al., 2010). Coarse ash and fine lapilli

deposited quickly while most of the fine ash and SO_2 initially dispersed to the southeast (Waythomas et al., 2010). The resulting SO_2 plume eventually entered the jet stream and traveled into the continental United States and Canada within a week (Krotkov et al., 2010).

The Kasatochi eruption is unique for various reasons. It resulted in the largest injection of SO_2 into the atmosphere since the Mount Hudson eruption in Chile, August 1991. Initial estimates were between 1.20 to 2.7 Tg (Krotkov et al., 2010; Prata et al., 2010). By using inverse transport modeling, Kristiansen et al. (2010) established a 1.7 Tg mass loading. In addition, plume altitudes exceeded the tropopause (maxima near 7 to 12 km with smaller emissions up to 20 km) introducing about 1.0 Tg of SO_2 into the stratosphere (Kristiansen et al., 2010).

Modeling SO_2 emissions is useful for various reasons. SO_2 is often collocated with volcanic ash and thus may be used as a proxy for ash where remote sensing is hindered by ice formation, water or cloud cover. Additionally, WRF-Chem studies of historical volcanic eruptions are motivated to test and provide source data and model parameterization schemes capable of predicting volcanic SO_2 and ash eruptions in an operational setting in near real-time. Here, we use the well-defined Kasatochi SO_2 eruption to study WRF-Chem's ability to model volcanic SO_2 transport and conversion.

2.2 BACKGROUND

Sulfur dioxide emissions from Kasatochi have been modeled previously with particle dispersion models (D'Amours et al., 2010; Kristiansen et al., 2010). Wang and others (2010) studied SO_2 dispersion and aerosol formation plume height sensitivity using the Eulerian GEOS-Chem model by initializing the model domain with time-fitted SO_2 column densities from the Ozone Monitoring Instrument (OMI) using the Extended Iterative Spectral Fit (EISF) method. This WRF-Chem study differs from the GEOS-Chem study in that it does not require plume column densities, only specific eruption source data such as location, height, emission rate and duration. These parameters are included in tabulated Eruption Source Parameters (Mastin et al., 2009), which may be used to initialize WRF-Chem for operational volcanic ash and SO_2 forecasts.

Sulfur dioxide converts quickly (on the order of days) to sulfate aerosols. In the stratosphere, where the majority of the Kasatochi SO_2 converted to sulfate, the conversion process is dominated by the interaction of SO_2 with the hydroxyl radical (·OH). Production of ·OH begins

with the generation of excited states of atomic oxygen from ozone and diatomic oxygen via photolysis. The hydroxyl radical oxidizes SO_2 in the stratosphere according to Equation 2.2.1.

$$SO_2 + \cdot OH + M \rightarrow HOSO_2 + M^* \quad (2.2.1)$$

M* is a third body quencher required to remove excess energy from the reaction. This process was initially proposed to decrease the ambient amount of □OH, and thus a second order rate equation would be needed to model it. However, as mentioned by McKeen et al. (1984), there is a cycling of the hydroperoxy radical, $\cdot HO_2$, and ·OH in the presence of nitrogen oxide species, NO_x (McKeen et al., 1984):

$$O_2 + HOSO_2 \rightarrow \cdot HO_2 + SO_3 \quad (2.2.2)$$

$$\cdot HO_2 + NO \rightarrow \cdot OH + NO_2 \quad (2.2.3)$$

This cycling ensures the regeneration of ·OH concentration. If we assume [·OH] is constant and [M] varies only with pressure, we may solve the following differential equation to analytically calculate the change in concentration of SO_2 with time:

$$\frac{dSO_2}{dt} = -k_3[SO_2][\cdot OH][M] \quad (2.2.4)$$

$$[SO_2]_f = [SO_2]_i e^{-k_{3,M}[\cdot OH]t} \quad (2.2.5)$$

Here, $k_3[M]$ is the pseudo first order rate constant based on Equation 2.2.3. Sulfur dioxide and ·OH also interact via aqueous phase reactions. In such reactions, ·OH is produced by dissolved hydrogen peroxide in water, which then reacts with dissolved, aqueous SO_2.

2.3 METHODS

The application of WRF-Chem for simulating the transport and effects of volcanic emissions within the atmosphere has been described (Stuefer et al., 2013). Importantly, WRF-Chem has been proposed as an operational tool for volcanic emissions modeling. Here, we test the feasibility of using WRF-Chem to capture SO_2 emissions using the well-studied 2008 Kasatochi eruption.

The choice of eruption initialization parameters greatly impacts the ability of the model to predict volcanic ash and SO_2 transport (Mastin et al., 2009; Webley et al., 2009). Table 2.1 lists the domain initialization parameters used in this study and Table 2.2 provides the initialization parameters for the eruption. We utilized the Global Forecast System (GFS) Final Reanalysis (FNL) datasets as base meteorological fields (NOAA, 2014).

WRF-Chem may use either default values for Eruption Source Parameters (ESP) or if available, source data from plume observations. Karagulian and others (2010) discovered a minimum of 1.7 Tg SO_2 from the Kasatochi eruption using remote sensing data from the Infrared Atmospheric Sounding Interferometer (IASI). Kristiansen and others (2010) utilized inverse transport modeling to establish a similar mass of 1.7 Tg based on measurements from UV, IR and Lidar data. In a recent GEOS-Chem study by Wang et al. (2013) a value of 2.0 Tg SO_2 was used. Herein, we initialized WRF-Chem with a total of 1.7 Tg of SO_2. This mass was gradually added to the model using a constant eruption rate of 23,600 kg s^{-1} over the course of the three eruptions, using eruption durations and times based on Waythomas et al. (2010) (compare Table 2.2).

WRF-Chem initializes, by default, volcanic ash and SO_2 plumes as an umbrella shape with 75% of erupted mass in the plume surrounding the specified plume height and 25% of the mass linearly detrained underneath (Stuefer et al., 2013). For the eruption plume height, the ESP implemented within the WRF-Chem preprocessor as a default includes a height of 11 km for Kasatochi. However, in accordance with Kristiansen et al. (2010), we chose 12 km a.s.l ± 4 km for this study in order to test the sensitivity of the model to its plume height source. For the example of our mean plume height of 12 km a.s.l, the umbrella will include 75% of the mass between 9 – 13 km a.s.l (peaking at 12 km a.s.l) and 25% below 9 km, linearly decreasing with height (Stuefer et al, 2013).

Kasatochi erupted over half of the SO_2 into the stratosphere. Therefore, it is important to capture the gas-phase chemistry behind stratospheric SO_2 oxidation shown in Equation 2.2.1. The model simulations utilized the Second Generation Regional Acid Deposition Model Mechanism (RADM2) for gas and aqueous phase reactions. The RADM2 model includes the oxidation of SO_2 by ·OH as depicted in Equation 2.2.1 using the first order kinetics in Equations 2.2.4 and 2.2.5 (Stockwell et al., 1990) as well as the treatment of the NO_x species in Equations 2.2.2 and 2.2.3. Gaseous precursors, such as NO and ·OH, were loaded into the model using the Prep-Chem-Source

1.4 preprocessor (Freitas et al., 2011). As mentioned, SO_2 also converts via aqueous phase chemistry with ·OH. This scheme is also parameterized within WRF-Chem RADM2.

Global ozone and other trace gases, such as SO_2, are detected by the Ozone Monitoring Instrument (OMI), a nadir viewing, ultraviolet (UV)/visible spectrometer aboard the National Aeronautical and Space Administration's (NASA) Earth Observing System's (EOS) Aura satellite. OMI covers a spectral range of 264-504 nm, allowing measurements of ultraviolet and visible SO_2 signals. It provides global coverage once per day with a nadir pixel size of 13 x 24 km^2 and swath width of 2,600 km and has been used in previous research studies for volcanic emissions analysis (Kristiansen et al., 2010; Krotkov et al., 2010; Lopez et al., 2013; Wang et al., 2013)

For spatial analysis, we utilized NASA's Level 2 SO_2 product, ColumnAmountSO2_STL (from here on STL). Column densities of SO_2 in Dobson Units (DU) for this product are shown in Figure 2.1. Since the STL derived data may underestimate the total amount of SO_2 in plume areas of high concentration, we used values from Krotkov et al. (2010) based on the Extended Iterative Spectral Fit (EISF) method for mass analysis. Applications of this method to Kasatochi SO_2 suggest that it may capture additional SO_2 that other algorithms might miss (Krotkov et al., 2010; Yang et al., 2010).

2.4 RESULTS

Figure 2.1 shows the dispersion of the plume as modeled by WRF-Chem and derived by the OMI STL product. The model captured the plume's interaction with the meteorology well, as it dispersed over the North American continent. Figure 2.2 shows a brief spatial analysis along two transects (105°W and 145°W) marked in red. Plume SO_2 column densities were generally collocated with OMI here, however the normalized masses peaked in different areas. To compare the change in mass in the domain, a linear correlation plot was constructed and presented in Figure 2.3. We saw a high degree of correlation (> 0.9 r^2) for all plume height test cases between the change in WRF-Chem predicted SO_2 mass and those observed by OMI.

A lifetime of SO_2 was established using linear regression analysis; the lifetimes significantly varied with height. The 12km eruption height yielded a 9.1 days lifetime (r^2=0.74) while the 8 km and 16 km plumes resulted in longer lifetimes of 10.6 and 17.1 days (r_2=0.72, 0.68), respectively.

2.5 DISCUSSION

WRF-Chem generally predicted a more disperse plume than was observed by OMI. In addition, there is a higher mass bias in the model results. This is markedly different from the work of Wang et al. (2010) where GOES-Chem produced a low mass bias. In addition, the mass located in the distal plume trended higher than that in the proximal. This is likely a direct result of the chosen ESP used for the modeled case as this varied with the plume height.

The rate of SO_2 conversion agreed well with literature values. We used values from Krotkov et al. (2010) using the EISF method and from Kristiansen et al., (2010) to test WRF-Chem output. In Figure 2.3 we see that all three initialized eruption heights produced r^2 values above 0.9.

As mentioned, a range of values was produced for the lifetime using linear regression analysis. The 12 km eruption produced the shortest lifetime, being about 9 days. This dependence of lifetime on plume height is most likely a direct result of different chemistry at the various levels of the atmosphere. The 12 km eruption included SO_2 mass located mostly in the stratosphere where conversion based on Equation 2.2.1 dominated, yet also included enough SO_2 in the troposphere where aqueous phase and heterogeneous chemistry can also occur.

WRF-Chem captured the dynamics and mass changes of the Kasatochi plume according to these results. It is, therefore, a robust candidate for volcanic emissions modeling, especially in the operational setting where multiple unknowns such as a specific plume height are present.

FIGURES

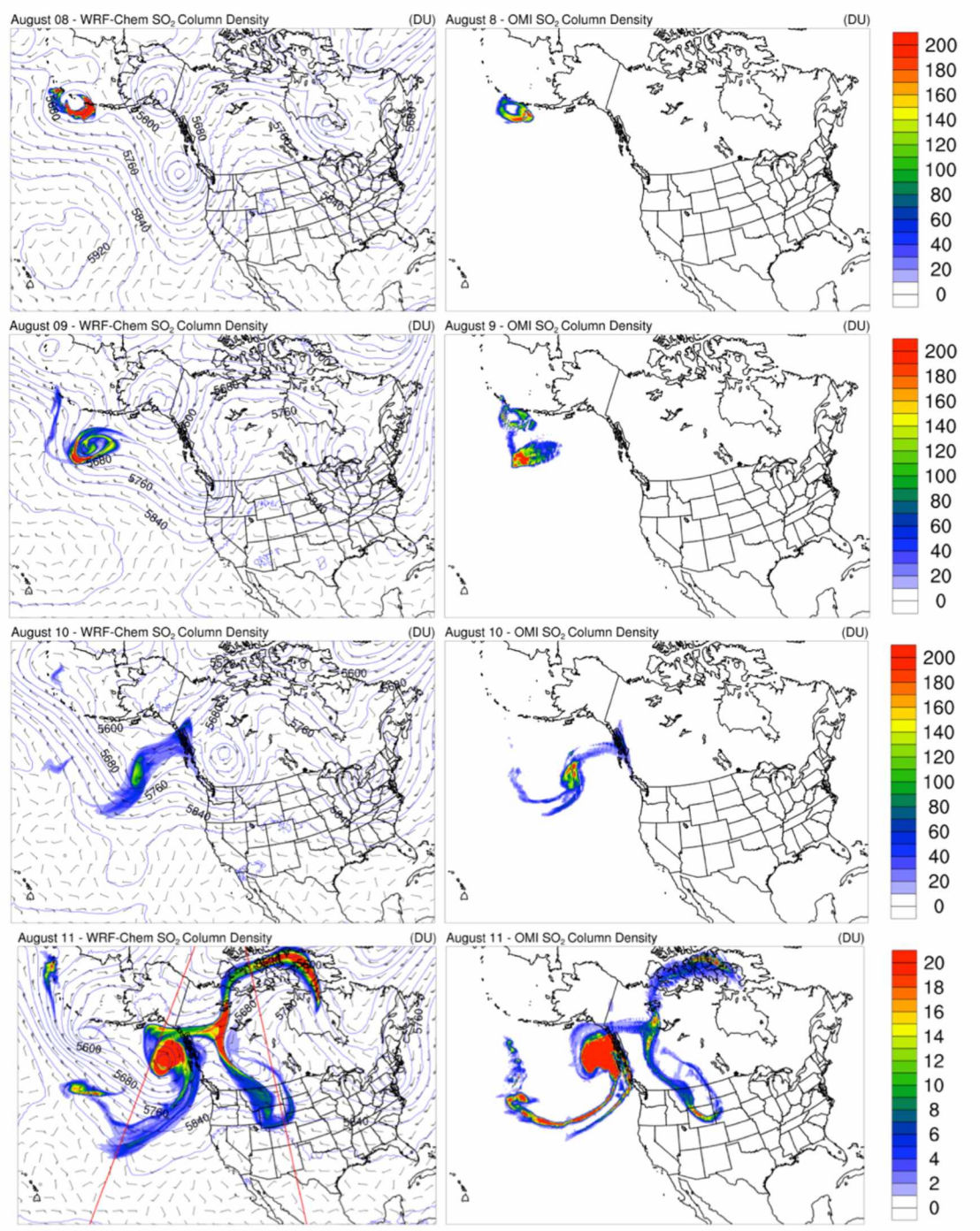

Figure 2.1 - Dispersion of the Kasatochi SO2 plume as modeled by WRF-Chem (left) and calculated by the OMI STL product (right). Spatial analysis transects are shown in Red on the August 11th plot.

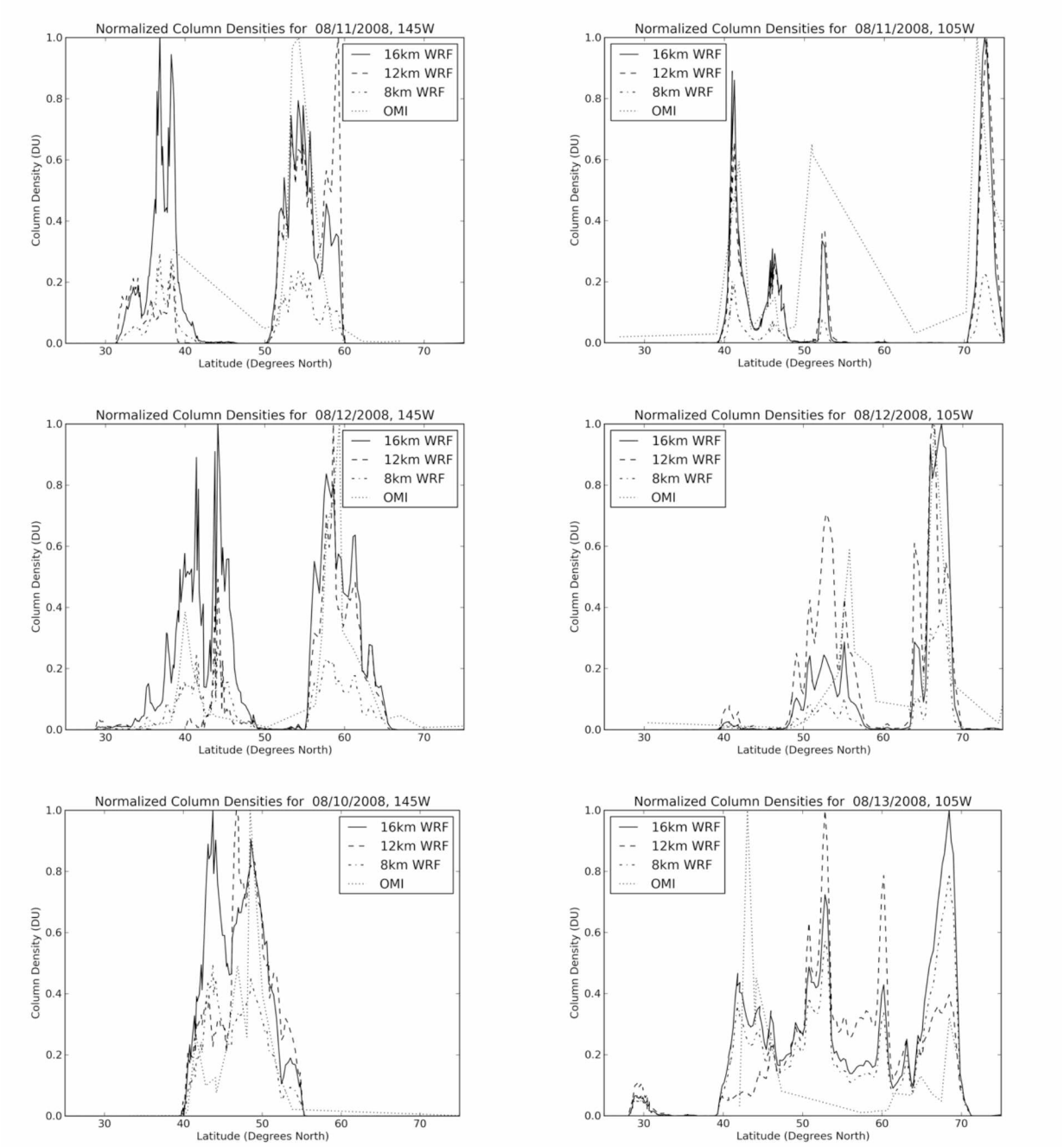

Figure 2.2 – Spatial comparisons of SO_2 column densities from WRF-Chem using 8, 12 and 16 km initialized plume heights and from OMI STL product.

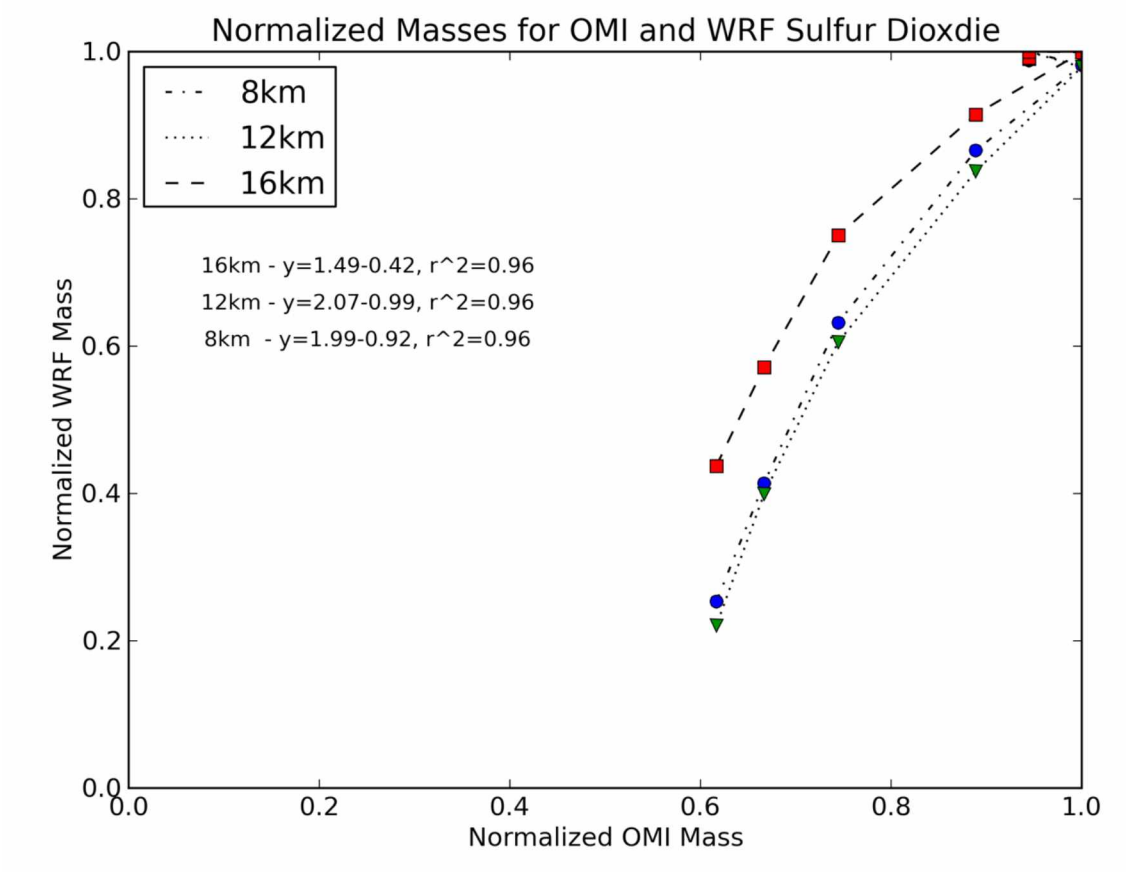

Figure 2.3 – Correlation between WRF-Chem (y axis) and literature OMI EISF (x axis) SO_2 domain masses for 8, 12 and 16 km plume heights.

TABLES

Table 2.1 – WRF-Chem domain parameters used for the modeling of the 2008 eruptions of Kasatochi Volcano

Domain Size	600 x 400
dx, dy	15 km x 15 km
Vertical levels	40, terrain following
Model Height	2,000 Pa
Projection	Lambert-Conformal
Center Lat/Lon	50°N, -120°W

Table 2.2 – Eruption times, durations and eruption rates of sulfur dioxide used in modeling of the 2008 eruptions of Kasatochi Volcano.

Eruption Date, Time	Eruption Duration	Eruption Rate
8/7 22:00 UTC	60 minutes	23600 kg/s
8/8 01:50 UTC	30 minutes	23600 kg/s
8/8 04:35 UTC	30 minutes	23600 kg/s

REFERENCES

D'Amours, R., Malo, A., Servranckx, R., Bensimon, D., Trudel, S. and Gauthier-Bilodeau, J.-P.: Application of the atmospheric Lagrangian particle dispersion model MLDP0 to the 2008 eruptions of Okmok and Kasatochi volcanoes, J. Geophys. Res. Atmospheres, 115(D2), D00L11, doi:10.1029/2009JD013602, 2010.

Freitas, S. R., Longo, K. M., Alonso, M. F., Pirre, M., Marecal, V., Grell, G., Stockler, R., Mello, R. F. and Sánchez Gácita, M.: PREP-CHEM-SRC – 1.0: a preprocessor of trace gas and aerosol emission fields for regional and global atmospheric chemistry models, Geosci Model Dev, 4(2), 419–433, doi:10.5194/gmd-4-419-2011, 2011.

Karagulian, F., Clarisse, L., Clerbaux, C., Prata, A. J., Hurtmans, D. and Coheur, P. F.: Detection of volcanic SO2, ash, and H2SO4 using the Infrared Atmospheric Sounding Interferometer (IASI), J. Geophys. Res., 115(D2), D00L02, doi:10.1029/2009JD012786, 2010.

Kristiansen, N. I., Stohl, A., Prata, A. J., Richter, A., Eckhardt, S., Seibert, P., Hoffmann, A., Ritter, C., Bitar, L., Duck, T. J. and Stebel, K.: Remote sensing and inverse transport modeling of the Kasatochi eruption sulfur dioxide cloud, J. Geophys. Res., 115(D2), D00L16, doi:10.1029/2009JD013286, 2010.

Krotkov, N. A., Schoeberl, M. R., Morris, G. A., Carn, S. and Yang, K.: Dispersion and lifetime of the SO2 cloud from the August 2008 Kasatochi eruption, J. Geophys. Res., 115(D2), D00L20, doi:10.1029/2010JD013984, 2010.

Lopez, T., Carn, S., Werner, C., Fee, D., Kelly, P., Doukas, M., Pfeffer, M., Webley, P., Cahill, C. and Schneider, D.: Evaluation of Redoubt Volcano's sulfur dioxide emissions by the Ozone Monitoring Instrument, J. Volcanol. Geotherm. Res., 259, 290–307, doi:10.1016/j.jvolgeores.2012.03.002, 2013.

Mastin, L. G., Guffanti, M., Servranckx, R., Webley, P., Barsotti, S., Dean, K., Durant, A., Ewert, J. W., Neri, A., Rose, W. I., Schneider, D., Siebert, L., Stunder, B., Swanson, G., Tupper, A., Volentik, A. and Waythomas, C. F.: A multidisciplinary effort to assign realistic source parameters to models of volcanic ash-cloud transport and dispersion during eruptions, J. Volcanol. Geotherm. Res., 186(1–2), 10–21, doi:10.1016/j.jvolgeores.2009.01.008, 2009.

McKeen, S. A., Liu, S. C. and Kiang, C. S.: On the chemistry of stratospheric SO2 from volcanic eruptions, J. Geophys. Res., 89(D3), 4873–4881, doi:10.1029/JD089iD03p04873, 1984.

NOAA: National Centers for Environmental Prediction Global Forecast System (Final) global gridded analysis archive - 2000 to Present, [online] Available from: http://rda.ucar.edu/datasets/ds083.2/ (Accessed 18 June 2014), 2014.

Prata, A. J., Gangale, G., Clarisse, L. and Karagulian, F.: Ash and sulfur dioxide in the 2008 eruptions of Okmok and Kasatochi: Insights from high spectral resolution satellite measurements, J. Geophys. Res., 115, D00L18, 2010.

Scott, W. E., Nye, C. J., Waythomas, C. F. and Neal, C. A.: August 2008 eruption of Kasatochi volcano, Aleutian Islands, Alaska—Resetting an island landscape, Arct. Antarct. Alp. Res., 42(3), 250–259, 2010.

Stockwell, W. R., Middleton, P., Chang, J. S. and Tang, X.: The second generation regional acid deposition model chemical mechanism for regional air quality modeling, J. Geophys. Res., 95(D10), 16343–16,367, doi:10.1029/JD095iD10p16343, 1990.

Stuefer, M., Freitas, S. R., Grell, G., Webley, P., Peckham, S., McKeen, S. A. and Egan, S. D.: Inclusion of ash and SO2 emissions from volcanic eruptions in WRF-Chem: development and some applications, Geosci Model Dev, 6(2), 457–468, doi:10.5194/gmd-6-457-2013, 2013.

Wang, J., Park, S., Zeng, J., Ge, C., Yang, K., Carn, S., Krotkov, N. and Omar, A. H.: Modeling of 2008 Kasatochi Volcanic Sulfate Direct Radiative Forcing: Assimilation of OMI SO2 Plume Height Data and Comparison with MODIS and CALIOP Observations, Atmospheric Chem. Phys., 13, 1895–1912, doi:10.5194/acp-13-1895-2013, 2013.

Waythomas, C. F., Scott, W. E., Prejean, S. G., Schneider, D. J., Izbekov, P. and Nye, C. J.: The 7–8 August 2008 eruption of Kasatochi Volcano, central Aleutian Islands, Alaska, J. Geophys. Res. Solid Earth, 115(B12), n/a–n/a, doi:10.1029/2010JB007437, 2010.

Webley, P. W., Stunder, B. J. B. and Dean, K. G.: Preliminary sensitivity study of eruption source parameters for operational volcanic ash cloud transport and dispersion models — A case study of the August 1992 eruption of the Crater Peak vent, Mount Spurr, Alaska, J. Volcanol. Geotherm. Res., 186(1–2), 108–119, doi:10.1016/j.jvolgeores.2009.02.012, 2009.

Yang, K., Liu, X., Bhartia, P. K., Krotkov, N. A., Carn, S. A., Hughes, E. J., Krueger, A. J., Spurr, R. J. D. and Trahan, S. G.: Direct retrieval of sulfur dioxide amount and altitude from spaceborne hyperspectral UV measurements: Theory and application, J. Geophys. Res. Atmospheres, 115(D2), doi:10.1029/2010JD013982, 2010.

CHAPTER 3* - MODELING VOLCANIC ASH AGGREGATION PROCESSES AND RELATED IMPACTS ON THE APRIL/MAY 2010 ERUPTIONS OF EYJAFJALLAJÖKULL VOLCANO WITH WRF-CHEM

*Submitted as Egan, S. D., Stuefer, M., Webley, P., Cahill, C. F. and Lopez, T., Hirtl M.: Natural Hazards and Earth System Science, November 2019

ABSTRACT

Volcanic eruptions eject ash and gases into the atmosphere that can contribute to significant hazards to aviation, public and environment health, and the economy. Several volcanic ash transport and dispersion (VATD) models are in use for operational forecasting of volcanic ash transport, but none include a treatment of volcanic ash aggregation processes. Volcanic ash aggregation can greatly reduce the atmospheric budget, dispersion and lifetime of ash particles and therefore its impacts. To enhance our understanding and modeling capabilities of the ash aggregation process, a volcanic ash aggregation scheme was integrated into the Weather Research Forecasting with online Chemistry (WRF-Chem) model. Aggregation rates and ash mass loss in this modified code are calculated in-line with the meteorological conditions, providing a fully coupled treatment of aggregation processes. The updated-model results were compared to field measurements of tephra fallout and in situ airborne measurements of ash particles from the April/May 2010 eruptions of Eyjafjallajökull Volcano, Iceland. WRF-Chem, coupled with the newly added aggregation code, modeled ash clouds that agreed spatially and temporally with these in situ and field measurements. A sensitivity study provided insights into the mechanics of the aggregation code by analyzing each aggregation process (collision kernel) independently, as well as by varying the fractal dimension of the newly formed aggregates. In addition, the airborne lifetime (e-folding) of total domain ash mass was analyzed for a range of fractal dimension, and a maximum reduction of 79.5% was noted.

3.1 INTRODUCTION

Volcanic eruptions inject gases and ash particles of various sizes into the atmosphere, posing hazards to life, infrastructure and aviation (Miller and Casadevall, 2000). Volcanic emissions can alter the composition of the atmosphere and affect the Earth's radiation budget and

climate (Angell, 1993; Cole-Dai, 2010; Thordarson and Self, 2003). The environmental and economic impacts of past and recent eruptions have spurred increased interest in the inclusion of volcanic ash into numerical weather prediction (NWP) models (Folch et al., 2009, 2015; Lin et al., 2012; Stuefer et al., 2013). Today, forecasters and scientists utilize volcanic ash transport and dispersion (VATD) models for ash hazard mitigation, the development, calibration and validation of remote sensing tools, the study of ash physics and to study the initial plume characteristics of eruptions. A current limitation of most VATD models is their ability to capture volcanic ash aggregation.

Volcanic ash aggregation is important for many reasons. Aggregation affects the atmospheric lifetime of ash, the distance ash is transported from the eruption source, the size and type of tephra observed on the ground, and the duration ash poses a threat to aircraft (Brown et al., 2012; Casadevall, 1994; Rose and Durant, 2011). Aggregation has been observed in several well studied volcanic eruptions such as those of Mount St. Helens (Washington), Mount Redoubt (Alaska) and Eyjafjallajökull (Iceland). Additionally, aggregation occurs in both proximal (< 15 km from the plume corner) and distal ash clouds (Bonadonna et al., 2011; Bonadonna and Phillips, 2013; Brown et al., 2012; Carey and Sigurdsson, 1982; Rose and Durant, 2009, 2011; Taddeucci et al., 2011; Wallace et al., 2013).

Proximal volcanic ash aggregates form more rapidly than distal aggregates for a number of reasons. For example, ice and liquid water enhance the sticking of particles and thus increases the rate of aggregation (Brown et al., 2012; Rose and Durant, 2011). This process can occur in a hail-like process with a cycle of freezing and thawing leading to enhanced aggregation (Van Eaton et al., 2015). In addition, the higher concentration of ash in the proximal plume increases the number of collisions.

Water enhanced aggregation in the proximal plume has been observed in a number of eruptions. Field observations of tephra from the May 18, 1980 eruption of Mount St. Helens detail the formation of large volcanic aggregates (up to 1mm) closely correlated with the presence of rain, snow, and hail (Waitt et al., 1981). Gilbert and Lane (1994) note that aggregation rates were enhanced by high proximal water vapor concentrations during the eruptions of Sakurajima volcano in the 1990s, and the majority of this water-enhanced aggregation occurred proximally, within the first minutes of the eruption. In addition, studies of the 2009 eruption of Mount Redoubt in Alaska

show definitive evidence for aggregation enhanced sedimentation in the proximal plume (Van Eaton et al., 2015; Wallace et al., 2013). Van Eaton et al. (2015) state the effects of aggregation were so great in the Redoubt eruption that over 95% of fine ash mass fell to the ground as aggregates.

Distal aggregation usually occurs at a slower rate than proximal aggregation as the plume ages and diffuses (Rose and Durant, 2009, 2011). Despite a slower rate of aggregation the majority of distal fine ash settles to the ground as larger aggregates (Brown et al., 2012; Carey and Sigurdsson, 1982; Rose and Durant, 2011; Wallace et al., 2013). Both coarse and fine ash particles are known to aggregate in distal clouds by forming dry clusters due to electrostatic attraction, or as liquid or frozen water particles (Brown et al., 2012; Rose and Durant, 2011). Distal aggregate formation has been observed from eruptions such as Etna Volcano, Italy in 1971, Mount St. Helens, U.S. in 1980 and Mount Redoubt, U.S. in 1990 (Booth and Walker, 1973; Sorem, 1982; Sparks et al., 1997). For many eruptions, electrostatic aggregation of fine ash is expected to be responsible for the bimodal distribution of volcanic ash fallout (Carey and Sigurdsson, 1982; Cornell et al., 1983; James et al., 2003).

Recently, aggregation processes were observed to play an integral role in the dispersion of the plume generated from the April and May 2010 eruptions of Eyjafjallajökull Volcano, Iceland. In-situ measurements of ash particle fall velocities using high speed photography observed aggregation-enhanced sedimentation that increased fallout rates by a factor of 10 (Taddeucci et al., 2011). The effect of ash aggregation caused a significant quantity of additional ash fall across Iceland, rather than be transported further. Ash aggregation overall clearly reduced the atmospheric residency time of the Eyjafjallajökull ash plume (Gudmundsson et al., 2012). In addition, aggregation was observed to cause enhanced fallout over parts of mainland Europe and the United Kingdom (Stevenson et al., 2012).

Aggregation processes not only affect the lifetime of volcanic ash, but also the makeup of volcanic ash cloud particle size distributions (PSDs) which may complicate modeling and remote sensing efforts (Brown et al., 2012; Rose and Durant, 2011). For example, volcanic ash remote sensing algorithms require information regarding particle sizes and extinction coefficients (Stohl et al., 2011; Wallace et al., 2013). Remote sensing methods are also used to estimate eruption parameters and PSDs via extinction coefficients using inverse modeling (Kristiansen et al., 2012;

Stohl et al., 2011). Additionally, volcanic PSDs are also important for the study of radiative properties of volcanic ash and their effects on the atmosphere (Hirtl et al., 2019; Young et al., 2012).

The effects imposed on volcanic ash clouds by aggregation processes necessitates their parameterization in volcanic ash transport and dispersion (VATD) models. Despite this, only few of the existing VATD models capture aggregation processes. For example, a volcanic ash aggregation parameterization scheme has been implemented within the FALL3D model (Folch et al., 2009). In an operational setting, FALL3D runs by ingesting offline meteorological fields from gridded atmospheric models, such as the Weather Research Forecasting (WRF) model, and then calculating volcanic ash advection and sedimentation during the parent model output time step. Another method of capturing volcanic ash aggregation is to initialize VATD models with PSDs that account for volcanic aggregation in the eruptive column by using initial plume models. FPLUME, a one dimensional (1D) plume model based on buoyant plume theory, constructs initial plume characteristics that account for ash aggregation (Folch et al., 2016). In this case, the 1D plume model develops an initial PSD at the source that accounts for aggregation processes and then keeps this PSD invariant during further plume transport.

In effort to study and predict volcanic ash aggregation effects using a fully coupled modeling system, where the fate of the airborne ash particles is coupled to the atmospheric environment, a volcanic ash aggregation scheme was incorporated into the Weather Research Forecasting with Chemistry (WRF-Chem) model (Grell et al., 2005). This coupled system requires no temporal nor spatial interpolations as it calculates interactions between the meteorology and ash at each modeling time step (on the order of seconds). While many dispersion models require less computing power than WRF, a number of them require a mesoscale model, like WRF, to generate regional, gridded meteorological fields for their initialization. As an example, FALL3D is typically initialized with a WRF model run that is executed prior to the dispersion model. Modeling particle dispersion with WRF-Chem is, therefore, as computationally feasible as running these models since in many cases, a mesoscale, gridded model must be run for their initialization.

The following sections of this paper detail the inclusion of a computationally feasible volcanic ash aggregation scheme into the WRF-Chem model and the impacts of these modifications on model output. The following 'Aggregation Parameterization and

Implementation' section (Section 3.2) details the background and incorporation of a mathematical scheme that is physically descriptive of aggregation processes into WRF-Chem, as well as the development of a new methodology for selecting aggregation sticking efficiencies that depend on relative humidity. This newly implemented code is then applied to the April and May 2010 eruptions of Eyjafjallajökull, as well as to a controlled sensitivity study using a single eruption. The setup of these two cases is discussed in Section 2.3 'Methods', with remarks on the model output in Section 2.4 'Results'. Concluding remarks are then provided in the final Section 2.5 'Conclusions'.

3.2 Aggregation Parameterization and Implementation

Smoluchowski (1917) developed the original analytical theory of the process of coagulation of colloid particles based upon Prof. R. Zsigmondy's experiments with gold solutions. The Smoluchowski Coagulation Equation (Equation 1) is an integrodifferential, population balance equation that describes the evolution of particle number density, $n_v(v)$, in time t, as primary particles of one volume, v , collide and stick together with particles of different volumes, v', to form aggregates (Smoluchowski, 1917). It is physically descriptive of the aggregation process.

$$\frac{\partial \mathrm{n_v(v)}}{\partial \mathrm{t}} = \frac{1}{2}\int_0^{\mathrm{v}} \mathrm{K(v-v', v)n_v(v-v')n_v(v')dv'} - \mathrm{n_v(v)}\int_0^{\infty} \mathrm{K(v, v')n_v(v')dv'} \quad (3.2.1)$$

Equation 1 describes the number of aggregates of volume v formed, n_v, per unit time, t, on the left, and the loss of primary particles between volumes v and v' on the right as particles aggregate based on the collision frequency of the particles. Frequency is weighted by the coagulation kernel, K, which is the product of the collision kernel, A, and a sticking efficiency, α, thus, $K = A\alpha$.

Volcanic ash may undergo various processes that result in collisions, such as Brownian motion, differential sedimentation and fluid shear, and as a result there are many formulations of the coagulation kernel, K (Jacobson, 2005). For example, collisions due to Brownian interactions (A_B) occur randomly during diffusion and are temperature dependent. As temperature increases, the diffusion rate increases thus increasing their chances of interacting with other particles. Particle collisions due to shear (A_S) occur when ash moving in different horizontal directions collide due

to changes in laminar flow. This kernel therefore depends on wind speed and direction. Lastly, differential sedimentation (A_{DS}) captures particle interactions due to the different fall velocities of different sized particles. The rate at which particles settle is dependent on their size and therefore the differential sedimentation kernel depends on the difference in size between particles. As larger particles fall, they have a greater chance of encountering smaller, slower moving particles on their descent. In summary, the collision kernels A_B, A_S and A_{DS} represent the rate at which ash particles collide based on Brownian motion, fluid shear and differential sedimentation, respectively. Each kernel depends directly on the number concentration and size distribution of ash particles, and each depends highly on its own set of parameters.

While physically descriptive of the aggregation process, the Smoluchowski Equation itself, in addition to the equations governing the coagulation kernel, K, is prohibitively computationally expensive to solve explicitly, even with simple boundary conditions. Advances in simplifying the equation for use in computational volcanic ash modeling resulted in large part from work by Dekkers and Friedlander (2002) and Costa et al. (2010) by assuming a time independent aggregate size distribution and fractal geometry of volcanic ash aggregates, respectively. Assuming a fractal aggregate geometry greatly simplifies the equations describing the coagulation kernels (A_B, A_S and A_{DS}) by establishing a particle size-volume fractal relationship, described by a fractal dimension factor , ξ. In addition, an assumption of fractal geometry allows n_v in Equation 1 to be described in terms of the total number of particles in a computational space, n_{tot}, forming aggregates of a certain fractal dimension, D_f, based on a generally accepted fractal relationship (Jullien and Botet, 1987; Lee and Kramer, 2004). The simplified Smoluchowski equation described by Costa et al. (2010) results in a calculation of $\frac{\partial n_v(v)}{\partial t}$, from Equation 1, that is much more computationally feasible (Equation 2)

$$\Delta n_{tot} = \alpha\left(A_B n_{tot}^2 + A_S \Phi^{\frac{3}{D_f}} n_{tot}^{2-\frac{3}{D_f}} + A_{DS}\Phi^{\frac{4}{D_f}} n_{tot}^{2-\frac{4}{D_f}}\right)\Delta t \quad (3.2.2)$$

Here, Δn_{tot} represents the total number of particles per unit volume lost to aggregation. The equation relies on the solid volume fraction of the aggregates, Φ (Folch et al., 2016), the number densities of the bins, n_{tot}, as well as the fractal dimension of the fine ash particles, D_f

(Costa et al., 2010). Equations describing the collision kernel, A, were also simplified using a fractal representation of ash geometry and were reduced to Equations 3-5, shown in Table 3.1.

New code capable of calculating Equations 2 to 5 was developed in this study and integrated into the WRF-Chem code. Refer to the appendix of this dissertation for the changes that were made. WRF-Chem 3.9.1 was used, which is available to download from the WRF homepage: www2.mmm.ucar.edu/wrf/users/downloads.html (Current Fall 2019). The edited code may be downloaded using the "git" repository located at "www.github.com/sdegan-USN/wrf_aggregation".

Most of the source variables necessary to solve Equations 2 to 5 are available in WRF-Chem by selecting the appropriate aerosol and chemistry packages. For example, chemistry option (chem_opt) 402 (WRF-Chem User Guide 3.9, 2018) includes chemistry and humidity variables provided by the Regional Deposition Acid Model Version 2 (RADM2) (Stockwell et al., 1990) and the Goddard Chemistry Aerosol Radiation and Transport (GOCART) models (Chin et al., 2000), as well as the inclusion of volcanic sulfur dioxide (SO_2) and ten volcanic ash particle size bins (Stuefer et al., 2013). Three variables required by Equations 2 to 5, the sticking efficiency, α, fractal dimension, D_f, and fractal dimension factor, ξ are not, however, included in WRF-Chem and therefore must be calculated or assumed.

The fractal dimension, D_f, relates the number of primary particles N in an aggregate to the size of the aggregate, R, such that N scales proportionally as $N \propto R^{D_f}$. For example, as D_f approaches 3, primary particles in the aggregate use up more and more space such that $D_f = 3.0$ would indicate a solid, filled aggregate. A lack of experimental data adds a degree of uncertainty when selecting the fractal dimension, however previous studies of eruptive events from Mount Saint Helens and Mount Spurr led to the use of $D_f = 2.99$ by applying a regression analysis applied to model output comparisons to observed deposits (Folch et al., 2010). The fidelity of confidence in the choice of the fractal dimension is also hindered by the fact that it does not necessarily, by its definition, remain constant with plume transport.

The fractal dimension factor, ξ, used to simplify the coagulation kernel equations relates the fractal dimension, D_f, to the diameters and volumes of the primary particles in the aggregates. This relationship is given in Equation 6

$$d_i = \xi v_i^{\frac{1}{D_f}} \quad (3.2.6)$$

Here, d_i and v_i are the diameter and volume of the primary particles forming an aggregate. Costa et al. (2010), Dekkers and Friedlander, (2002) and Folch et al. (2010) indicate that a fractal dimension on the order of 0.6 to 1 is sufficient for describing the geometry of volcanic ash particles and aggregates. As done in Costa et al. (2010), a unity fractal dimension factor is utilized in this study.

The sticking efficiency coefficient, α, relies heavily on the concentration of water vapor and ice (Costa et al., 2010). In order to formulate an appropriate estimate for the sticking efficiency coefficient, a new parameterization was incorporated into the WRF-Chem emissions driver that includes volcanic water vapor emissions that are specified by the user. This code adds these emissions to the ambient water vapor mass within the model environment. Van Eaton et al. (2012) demonstrated that the sticking efficiency of volcanic ash particles follow exponential curves. Using these fitted curves, the sticking efficiency coefficient, α, between two particles i and j may be calculated using a fitting coefficient, S. This coefficient varies with water vapor concentration, $[H_2O]$, and the radius of the colliding particles, r. A lookup table was added to select sticking coefficients based on this work by utilizing the water vapor content of the model cell and the particle size (Equation 3.7 and Table 3.2). Importantly, this equation is computationally inexpensive to solve. Although electrostatic interactions are significant enough to cause aggregation of particles, they are most likely insignificant when compared to aggregation in the presence of water (James et al., 2003; Schumacher and Schmincke, 1995). Since the modeled background water rarely approaches 0% relative humidity, dry interactions are not parameterized in this study.

$$\alpha(ij, [H_2O]) = e^{-Sr} \quad (3.2.7)$$

The four aggregation equations (Equation 2 to 5) are solved for volcanic ash bins 2 to 10 at every time step, for every model grid cell, and account for interaction of particles between the different bins by using the total mass to calculate the available number of primary particles available for aggregation. Large particles, greater than 1 mm in diameter, are included in WRF-Chem volcanic ash bin 1, which has been designated as the "aggregate" bin. All aggregates generated by the code are moved to bin 1 since large particles assume high fall velocities and thus

contribute to ash fallout within periods of minutes to hours (Rose and Durant, 2011) and their corresponding masses are subtracted from bins 2-10. All volcanic ash removed from the model domain is stored in the ASH_FALL variable, allowing the analysis of fallout mass and location when enabled in the WRF-Chem registry.

3.3 METHODS

Eyjafjallajökull erupted in April and May 2010, dispersing ash over Europe that caused numerous flight delays over the course of weeks and a resulting loss of revenue to airlines in the billions of dollars (Harris et al., 2010). Due to the massive extent of the eruption's impacts on Europe, it became one of the most studied and well-documented eruptions in history, providing numerous sources of data regarding the plume's characteristics. For example, the German Aerospace Center (Deutsches Zentrum für Luft- und Raumfahrt, DLR) took several in situ measurements of Eyjafjallajökull's ash clouds over the course of the two months of eruptions by flying its Falcon aircraft into forecasted plume locations. During the flights, Schumann et al. (2011) recorded particle number concentrations using a Grimm SKY-OPC 1.129 optical particle counter and a Particle Measuring Systems, Inc. (PMS) Forward Scattering Spectrometer Probe (FSSP), observing a range of particles from 0.25 and 24 μm. In addition, upper and lower mass concentration estimates were calculated using the minimum and maximum imaginary component of the refractive index, of which the FSSP was particularly sensitive. For the flight of May 17, a "medium" estimate of mass concentration was also calculated that lies between the upper and lower values. From these studies, information on particle number, mass concentration, plume heights and gas composition are available, providing one of the best datasets available to study distal and proximal volcanic emissions (Schumann et al., 2011). In addition to these in situ data, Doppler measurements of the eruptive column and ground air sampling measurements were conducted by many groups to establish descriptive and accurate eruption source parameters (Arason et al., 2011; Devenish et al., 2012a, Devenish et al., 2012b; Stevenson et al., 2012). Observations of volcanic tephra fallout are also available and provide important insights into the PSD and transport of the distal Eyjafjallajökull ash clouds (Gudmundsson et al., 2012; Stevenson et al., 2012). In addition, volcanic ash aggregation was directly observed via high speed photography near the vent, lending proof that particle aggregation occurred in the plumes Eyjafjallajökull produced (Taddeucci et al., 2011).

3.3.1 EYJAFJALLAJÖKULL MODEL DOMAIN SETUP

The newly implemented aggregation code was applied to the April and May 2010 eruptions of Eyjafjallajökull. Additionally, sensitivity studies were conducted using a single eruption on May 5th, 2010. In all studies, the model domain was centered at 50°N, 0°W, offsetting the Eyjafjallajökull vent (63.62°N, 19.61°E) to the northwest of the domain to account for the southwest trajectory of the ash clouds. The model was setup for high spatial resolution simulations at 10 km^2 per grid cell, with a total of 500 x 500 horizontal grid cells per vertical layer. The domain is shown in Figure 3.1 with Eyjafjallajökull marked in red. The model included 48 pressure levels with the top level of the model set to 2,000 Pa. The integration time step of the dynamics and chemical fields was set to 30 seconds.

Meteorological fields were obtained from the National Center for Environmental Prediction Final Global Operational Analysis (NCEP FNL) datasets, ds083.2, accessed through the National Center for Atmospheric Research Data Archive (NCAR, 2000). These datasets represent the final analysis of historical Global Forecast System (GFS) model output. Ingest was conducted similar to Hirtl et al. (2019), using a 9 day spin up time before the first eruption on 14 April and with meteorological initializations every 48 hours. The WRF-Chem volcanic package was enabled with chemistry option 402, which includes ten particle sizes of volcanic ash (Stuefer et al., 2013). These particle sizes are shown in Table 3.3. The Yonsei University Planetary Boundary Layer (YSU PBL) scheme and the Noah Land Surface Model (LSM) were included for PBL and near ground physics (Chen and Dudhia, 2001; Hong et al., 2006).

Water was added to the model domain by multiplying the water content of Eyjafjallajökull's magma, 1.8% (Keiding and Sigmarsson, 2012) to the total erupted mass of 400 Tg for fine and coarse ash estimated by Taddeucci et al. (2011). This 1.8% multiplier produces water vapor emissions that agree with constraints constructed by comparing H_2O/SO_2 emission ratios using values from Allard et al. (2011), yielding a ratio of 458 mol/mol, and SO_2 emission rates from two remote sensing studies by Boichu et al (2013 and Thomas and Prata (2011). The code was modified to read in volcanic water vapor emissions rates into WRF-Chem as a callable Fortran module.

In addition, Hirtl et al. (2019) noted that the model topography of Eyjafjallajökull is smoothed at the 10 km^2 model spatial resolution, resulting in a vent height 400 m lower than the actual height of 1000 m. A 400 m height offset was applied to correct this.

3.3.2 Sensitivity Study – Parameterizations

Multiple sensitivity studies were conducted in order to assess: 1) the overall change in mass due to aggregation, 2) the effects of different fractal dimensions, D_f, on the aggregation rate, 3) the contribution of each collision kernel, A_B, A_S and A_{DS}, to the decrease in domain ash mass and 4) the effect of adding coupled water vapor emissions to the model domain on the aggregation rate. These sensitivity studies were conducted on a smaller time slice of the parent domain, using a 9 hour eruptive event on May 5th, 2019, initialized at 00:00Z with a rate of 4 x 10^6 kg s^{-1}, which corresponds to an average value of Eyjafjallajökull's largest eruptions. A 72 hour spin up time was included prior to the eruption initialization to allow the meteorological fields to stabilize, and was then run for 6 days, ending 00:00Z on the 11th of May. New meteorological fields were ingested every 24 hours for high fidelity. Each volcanic ash bin was populated with 10% of the total erupted mass in order to simplify output analysis.

In order to assess how the aggregation code affects model output, WRF-Chem was run with and without the aggregation code enabled. Due to a lack of experimental data, a choice of fractal dimension, D_f, is difficult. Therefore, the fractal dimension, D_f, was varied to measure its effects on the overall aggregation rate. The span of fractal dimensions chosen ranges from $D_f = \{2.5, 2.6, 2.7, 2.8, 2.9, 2.95, 2.98, 2.99, 3.0\}$ and is based on studies by Costa et al. (2010) and from a similar study of Mount Saint Helens and Mount Spurr using Fall3D by Folch et al. (2010). In the later, a fractal dimension of 2.99 was chosen based on a best fit method (Folch et al., 2010).

The contribution of each collision kernel, A_B, A_S and A_{DS}, to the total reduction in domain mass was also assessed by using the same domain and eruption parameters, and enabling only one kernel at a time using a fractal dimension of 2.5 and 3.0. The total change in mass from each kernel was then divided by the total change in mass with all kernels enabled to find the percent contribution.

The impacts of the inclusion of water vapor on the aggregation rate were studied by running the code with and without the 1.8% water vapor emissions included in the model domain. For the

simulation run without water vapor emissions, only background water vapor from the FNL datasets were used.

3.3.3 April and May 2010 Eruptions of Eyjafjallajokull - Parameterizations

WRF-Chem was also configured to simulate Phase I (April 2010) and the Phase III (May 2010) eruptions of Eyjafjallajökull using the same model domain described above. Phase II eruptions were effusive rather than explosive and ejected tephra at much lower altitudes of 2 to 4 km ASL (Gudmundsson et al., 2012) and were thus not included in this modeling case study.

Eruption source parameters (ESP) for Eyjafjallajökull were adapted from Mastin et al. (2014) and Hirtl et a. (2019). Camera footage and C-band Doppler radar measurements were used to establish three hourly plume heights for the April and May 2010 eruptions (Arason et al., 2011; Mastin et al., 2009; Hirtl et al., 2019). These plume heights were used to calculate eruption rates based on the plume height/eruption rate relationship derived by Mastin et al. (2009). The total erupted mass was then scaled based on work by Gudmundsson et al. (2012) such that the total ash mass ejected over the eruptive phases agreed with the 190 Tg estimate for fine ash stated (Hirtl et al., 2019). The bimodal, silicic (S2) ESP particle size distribution (Table 3.3) was used to populate the ten volcanic ash bins in the model (Mastin et al., 2009). The three hourly plume heights and eruption rates used in the study are presented in Figure 3.2.

In this study, all aggregation collision kernels were enabled, and water vapor emissions as described previously were added to the model domain at each time step. As mentioned earlier, the choice of a fractal dimension is hindered by a lack of experimental data. Folch et al. (2010) conducted linear regression analysis of repeated model run comparisons to tephra fallout measurements from eruptions originating at Mount Spurr and Mount Saint Helens. This study resulted in the use of a 2.99 fractal dimension. Due to a lack of experimental data on the development of volcanic ash fractal dimensions, and the fact that aggregate fractal dimensions are not necessarily constant with time, D_f was set at the upper bound of 3.0, providing the maximum, aggregation rate.

3.4 RESULTS

The newly implemented aggregation code was first assessed with a sensitivity study of a singular eruptive event, and then by application to the entire Phase I and Phase III eruption periods.

3.4.1 SENSITIVITY STUDY RESULTS

Varying the fractal dimension between 2.5 and 3.0 resulted in a range of aggregation rates. Figure 3.3 illustrates the change in domain mass from a single 9 hour eruption on May 5th at 00:00Z with a constant eruption rate of 4 x 10^6 kg s^{-1}. As expected, higher values of D_f result in higher rates of aggregation with the largest jumps in the aggregation rate between D_f = 3.0 and 2.8. To quantify the change in aggregation rate, volcanic ash lifetimes in terms of e-folding were calculated. This analysis is presented in Figure 3.4 and indicates a range of e-folding times from 72 hours with no aggregation code enabled to 15 hours with maximum aggregation considered (D_f = 3.0). Based on work by Folch et al. (2019), it is assumed that a true value of the fractal dimension likely lies near D_f = 2.99, which corresponds to a 79.5% difference in e-folding times. In terms of volcanic ash lifetime, on hourly timescales, there is no difference between D_f = 3.0 and 2.99.

Figure 3.5 shows the extent to which each kernel contributed to the overall change in the model domain's ash mass by enabling each kernel independently. Two fractal dimensions were considered, D_f = 2.5 and 3.0, and both affected each kernel's contribution to aggregation differently. The differential sedimentation kernel, A_{DS}, for example contributed to the majority of the change in domain mass over the course of the 96-hour model run ($\approx$ 99%) when D_f was set to 3.0, but contributed only 5% on average with D_f = 2.5. The Brownian kernel became the major contributor to aggregation in the case of D_f = 2.5, contributing to over 90% of the aggregation. This agrees with parametric studies of varying fractal dimensions by Costa et al. (2010), who noted this trade between A_{DS} and A_B when considering fine ash particles (<63 μm). Overall, fluid shear interactions were the minor contributor to aggregation for both fractal dimensions. While its contribution to aggregation approaches that of A_{DS} for D_f = 2.5, it is many orders of magnitude lower than A_B or A_{DS} for D_f = 3.0.

Figure 3.6 illustrates the percentage of total domain mass comprised of volcanic ash bins 7-10. Here, aggregation is run with D_f = 3.0. Larger bins (1-6) were not included due to the rapid

decrease in their domain mass as a result of their settling velocities. Figure 3.6 depicts a shift in the particle size distribution due to aggregation. The aggregation code results in less contribution from fine ash particles (bins 7, 8 and 9), resulting in a shift of the PSD towards bin 10. This is the result of the size of the particles since larger radii result in a larger probability cross section of collision and subsequent aggregate formation.

Coupling water emissions resulted in a very small increase in aggregation rate, lowering the total domain mass on the order of Mg hr^{-1}, much lower than the overall loss rate of ash due to aggregation on the order of Tg hr^{-1} (6 orders of magnitude). The sticking efficiency, Equation 6, is high (> 90%) for small particles (< 63 μm). As the residence time of large particles is very short, the sticking efficiency is applicable to the narrow range of particle sizes that persist in the domain (Bins 7-10, < 32.5 μm). These particle sizes correspond to a narrow range of sticking efficiencies (.87 to .97), regardless of the water vapor concentration.

3.4.2 EYJAFJALLAJÖKULL STUDY RESULTS

The ash cloud dynamics generated by WRF-Chem over the model period agree with other modeling studies of Eyjafjallajökull utilizing WRF-Chem (Hirtl et al., 2019; Webley et al., 2012). Figure 3.7 provides an example of the output from WRF-Chem for April 15 and 16, 2010. The dynamics of the ash clouds are apparent. The plume moves south and east towards the coasts of Scandinavia and northern Europe then splits into two plumes: one residing over Sweden and Finland and the other passing through multiple northern European countries.

Model output also agrees with airborne in situ measurements. DLR research aircraft conducted 13 flights on 11 different days that transected Eyjafjallajökull's ash clouds over the course of the Phase I and Phase III eruptions (Schumann et al., 2011). Predicted ash concentrations from WRF-Chem were compared to the in situ observational data from three of these flights: April 19 and May 16, and 17, 2010. WRF-Chem volcanic ash bins 8, 9 and 10 correspond to the particle size detection limits of the Grimm OPC and PMS FSSP aboard the Falcon aircraft and were thus chosen for comparisons.

Figure 3.8 presents time series plots of WRF-Chem output and DLR measurements. Figures 3.8(A), 3.8(C), and 3.8(E) cast the WRF-Chem output in mass concentration (g m^{-3}). Figures 3.8(B), 3.8(D) and 3.8(F) cast the WRF-Chem ash bin as number concentrations by using

an assumed particle density of 2500 kg m^{-3} (Brown et al., 2012) in order to make direct comparisons to the Grimm OPC and FSSP detectors.

Temporal changes in observed and modelled ash concentrations agreed moderately well for the April 19 flight (Figures 3.8A and 3.8B). Analysis of particle number densities in Figure 3.8B for 14 April shows 5 significant overestimations of volcanic ash by the non-aggregation enabled code, between 50-75% at 14:55 and 15:07, between 15:15-15:18, between 15:35-15:42 and between 16:55-17:06. These overestimations did not occur when the aggregation code was used. One peak concentration was observed at 15:30 UTC on April 19, which was not resolved by WRF-Chem (Figure 3.8B). Typical of any Eulerian air quality model, WRF-Chem tends to diffuse ash concentrations, an effect that is also dependent on the model resolution. Smaller domain grid cells permit better comparison with point observations, but decreases in grid cell sizes are computationally expensive.

Number density readings for May 15 (Figure 3.8(D)) contained more robust data than mass concentration (9(C)) and was therefore used in the analysis for this date. Here, a large overestimation of ash is calculated by WRF-Chem when not using the aggregation code. A peak of 290 particles cm^{-3} are observed in the unmodified code, almost 10 times higher than observed. With aggregation enabled, the WRF-Chem solution is much closer at a maximum of 45 particles cm^{-3}, showing a stark improvement.

On May 17 (Figures 3.8(E) and 3.8(F)), the aircraft performed a steep transect through a plume with larger ash particles. Almost no ash concentration was recorded at the lowest flight altitude reached during the middle of the flight at 16:40 UTC. At this same time, WRF-Chem predicted concentrations in excess of 400 g m^{-3}. Where the plume locations do agree, there is improved agreement between the aggregation enabled code and the airborne observations of mass concentration. For the entire time range, observations where the aggregation code produced mass readings in the same order of magnitude as those observed by DLR were counted. This total was then divided by the total flight time and resulted in an average 80% agreement of the data (78% for April 19, 78% for May 15 and 83% for May 17). This fell to an average of 62% when the code was run without aggregation, using the same methodology.

In addition to comparisons with Schumann et al. (2011) in situ measurements, WRF-Chem tephra fallout was also compared to field measurements of tephra collected by Stevenson et al., (2012) in the United Kingdom (UK). Figure 3.9 depicts the mass of tephra deposited in the model domain from all April 2010 eruptions in panel (A) and from May 2010 eruptions in panel (B). Stevenson et al. (2012) report three sampling periods that overlap with the model domain times in this study. For example, Stevenson et al. (2012) counted 218 grains of tephra per cm^2, at Benbecula in the Outer Hebrides (57.43N, 7.34W, Figure 3.9(A), white circle), with a mean diameter of 18 $\pm$ 7 μm while sampling between 13-20 May, 2010. Assuming an average density of 2,500 kg m^{-3} yields a tephra concentration between 20 and 45 mg m^{-2}, compared to 31 mg m^{-2} predicted by WRF-Chem with the aggregation code enabled during the same time range. Samples taken at Leicestershire (52.73°N, 1.16°W, Figure 3.9(B), white circle) between 25 April and 3 May, 2010 estimate a range of tephra mass on the ground between 51 and 119 mg m^{-2}, also near the WRF-Chem estimate of 41 mg m^{-2} (80% of observed mass) between those dates. Another sample from Lincolnshire (52.74N, 0.38W, Figure 3.9(B), white circle) covered a period from 24-30 April 2010. In this case, tephra fallout between 3 and 13 mg m^{-2} were measured, whereas WRF-Chem predicted a smaller value of 1.2 mg m^{-2} (40% of observed mass). The smaller estimates for the Lincolnshire and Leicestershire sites may be explained by the lack of model data covering 27 April – 3 May, as the last modeled hour was 00:00 UTC on 27 April. When considering WRF-Chem run without aggregation the fallout seen in these areas is minimal, with less than 1 mg m^{-2} observed.

The aggregation code altered the overall particle size distribution of the domain. To study this change, the model domain mass was analyzed from 14 to 18 May, 2010. This time frame represents the last 96 hours of modeled eruptions and includes a high degree of variability in the eruption rate and plume height (see Figure 3.2). The total domain mass is presented in Figure 3.10 without (A) and with (C) the aggregation code enabled. To analyze the PSD, the mass of each volcanic ash bin was divided by the total model domain mass. The resulting percentages are presented in Figure 3.10(B) and 11(D). The top panels, Figures 3.10(A) and 3.10(B), depict WRF-Chem output without the use of the aggregation code, whereas the lower panels, Figures 3.10(C) and 3.10(D), include the aggregation code. The short atmospheric lifetime of the large particles in bins 1-3 result in small masses during this time frame compared to smaller bins 4-10. As such, only bins 4-10 are depicted in Figure 3.10. Major changes in the eruption rates are annotated on the time axis with red marks.

Initially, the eruption rate is 7.36 x10^5 kg s^{-1} (7.949 Tg per 3 hours) before 09:00 UTC on 14 May. For this time period, ash bins 5, 6, 7 and 8 are the dominant sizes when run without aggregation. This is a result of their larger share of the erupted particles from the chosen S2 size distribution. When aggregation is included, the PSD is shifted towards the smaller bins 7, 8 and 9, indicating that the aggregation code calculates a general shift towards finer ash bins.

The eruption decreases to 1.09 x 10^5 kg s^{-1} (1.177 Tg per 3 hours) at a height of 5.6 km at 09:00 UTC (red mark 1 in Figure 3.10) and is variable thereafter until 06:00UTC on the 16th of May (red mark 2). At this point the eruption rate increases back to 7.36 x 10^5 kg s^{-1}. Here, between marks 2 and 3, the model solution without aggregation depicts bins 7 and 8 as the predominant sizes in the domain, whereas the solution including aggregation again shows a shift towards finer particles with bins 8 and 9 the dominant species. Between 00:00UTC and 15:00UTC on May 17 (marks 3 and 4), a period of high variability in eruption rate from a maximum of 7.36 x x10^5 kg s^{-1} to a minimum of 0.977 x10^5 kg s^{-1} occurs. In the non-aggregation enabled solution, bin 7 increases past bin 9 during this time period, however this is not seen in the aggregation enabled solution, again depicting a shift of the PSD towards finer ash particles.

3.5 Summary and Conclusions

To date, no operational volcanic ash transport and dispersion (VATD) model includes a fully coupled, online treatment of volcanic ash aggregation, leaving a process which can reduce ash lifetimes substantially as an uncertainty. Here, a simplified version of the Smoluchowski coagulation equation (Costa et al., 2010; Dekkers and Friedlander, 2002; Folch et al., 2010, 2016; Smoluchowski, 1917) was incorporated into the WRF-Chem model. This simplified method was chosen for its computational efficiency, allowing the aggregation rate to be calculated at each model time step in line with the atmospheric dynamics.

The effects of the aggregation code were assessed by applying it to a high resolution model study of the 2010 eruptions of Eyjafjallajökull, including a single study of a 9 hour test eruption. The effect of each particle collision kernel on the overall aggregation rate (Equation 2) was studied by enabling them independently. The degree to which each kernel affected aggregation depended on the choice of the fractal dimension, D_f. The differential sedimentation kernel provided the largest contribution by orders of magnitude when a fractal dimension of 3.0 was chosen; however,

the Brownian kernel dominated when a fractal dimension of 2.5 was chosen. This result suggests that vertical motion, when a fractal dimension near 3.0 is chosen, is the primary driving force behind particle interactions in the aggregation process, rather than random (Brownian) or horizontal (shear) motions. Additionally, analysis of the volcanic ash lifetime shows that varying the fractal dimension may greatly vary the lifetime, especially when considering fractal dimensions between 3.0 and 2.8.

The Eyjafjallajökull model study was assessed by comparison to aircraft in situ measurements taken by DLR as well as tephra fallout samples measured in the United Kingdom. By comparing WRF-Chem calculated volcanic ash mass concentrations using the aggregation code to those observed by DLR, an average 80% match in an order of magnitude was observed for the 3 flights analyzed. Additionally, non-aggregation enabled code calculated 20-50% higher volcanic ash concentrations on numerous occasions, where the aggregation enabled code did not. The aggregation-enabled WRF-Chem code tended not to overestimate volcanic ash, or to overestimate less than the non-aggregation-enabled version, potentially yielding more realistic ash concentrations which may benefit aircraft hazard mitigation forecasting.

As the plume transported over the United Kingdom, WRF-Chem predicted ash fallout in ranges that matched field measurements. Tephra fallout generated by WRF-Chem fell within observed values at one sample location, and predicted on average 60% of the fallout at two others. This suggests that WRF-Chem may be used to model not only the atmospheric transport of ash clouds, but the deposition of ash as well.

Importantly, these observations all suggest that two factors drive volcanic ash aggregation when including aggregation in the WRF-Chem code. First, volcanic ash concentration is noted to be the primary driving factor behind aggregation rate. The majority of model domain mass decreased near the vent where concentrations of ash are high. In addition, PSD analysis indicates that bins with higher portions of the eruption PSD undergo faster rates of ash aggregation. Bins with a larger share of the eruption PSD will aggregate faster due to their increased probability of collision. Second, vertical motions of ash falling through the atmosphere also drive the aggregation process through differential sedimentation for realistic ranges of fractal dimension (between 2.95 and 3.0).

The inclusion of this aggregation scheme into WRF-Chem provides research and operational meteorological communities a second VATD model that includes volcanic ash aggregation and is the first to run aggregation in an inline fashion where aggregation equations are solved at each model time step. This inline computation of volcanic ash yields many benefits. For example, the code identifies the driving forces behind volcanic ash aggregation, i.e. ash concentration and differential sedimentation rates, and allows for the study of the effects of water vapor concentration on the aggregation rate. In addition, it allows the study of changes in particle size distributions due to enhanced ash settling as a result of aggregation processes, which are of particular importance to remote sensing communities where the effective particle size directly impacts the spectral methods used for detection. The modified code also benefits the operational volcanic ash modeling community by providing another VATD model for use in aircraft hazard mitigation. Additionally, the modified code is computationally expedient. It ingests global models and runs volcanic ash dispersion and aggregation code while simultaneously calculating mesoscale atmospheric dynamics, eliminating the need for additional, offline dispersion runs. Ultimately, this study provides another step towards the inclusion of volcanic ash aggregation, an important physical process, into VATD models.

3.6 ACKNOWLEDGEMENTS

This publication is the result of research sponsored in part by the NOAA Cooperative Institute for Alaska Research (CIFAR) with funds from NOAA under cooperative agreement NA13OAR4320056 with the University of Alaska Fairbanks (UAF). The Alaska Space Grant Program supported this work. Computational time was provided by UAF Research Computing Systems at the Geophysical Institute and the Department of Defense High Performance Computing and Modernization Program. We are thankful to Dr. Alexa Van Eaton of the Cascades Volcano Observatory, United States Geological Survey, who provided a significant amount of guidance to understand the volcanic ash aggregation process better.

FIGURES

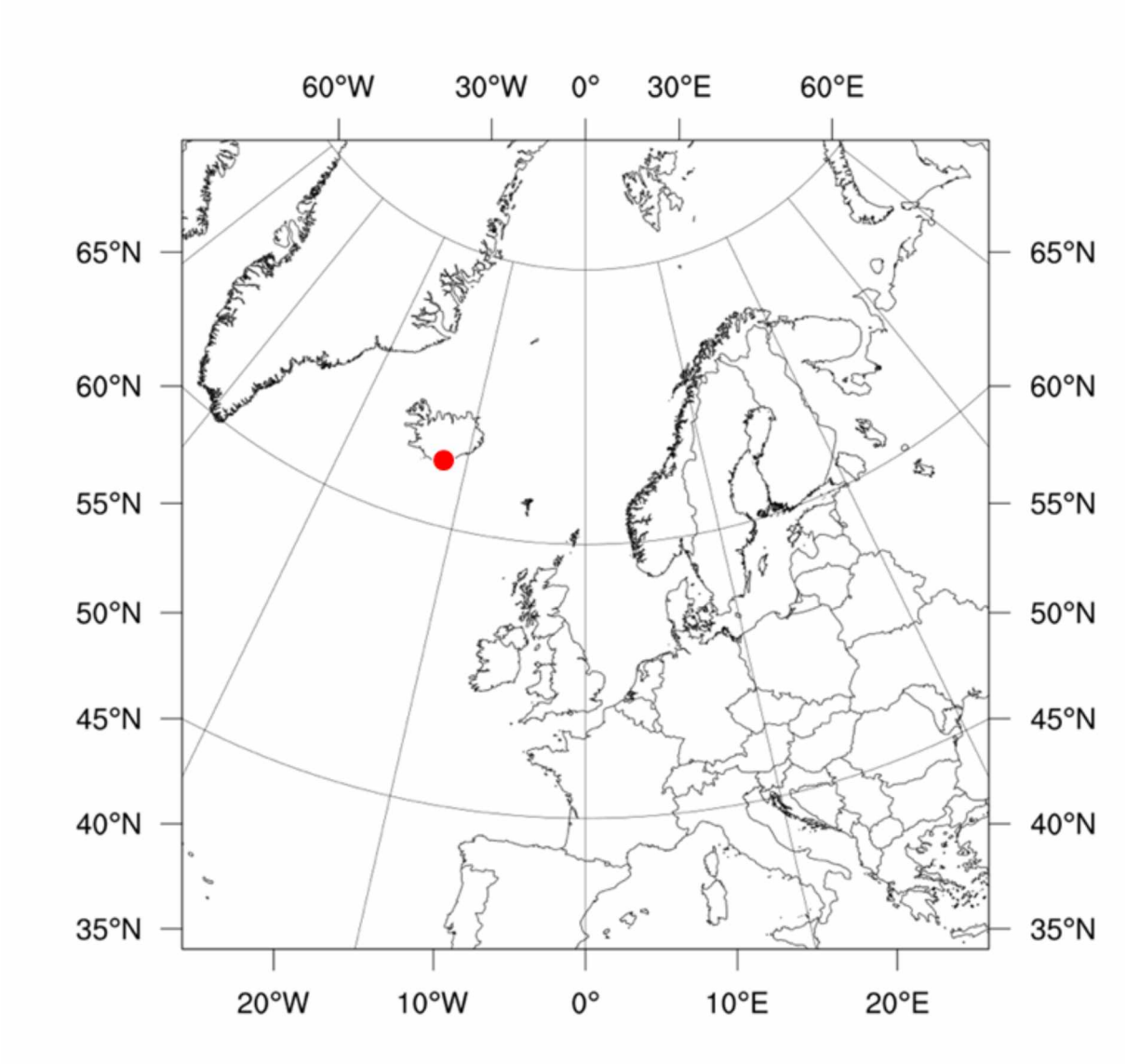

Figure 3.1 – WRF-Chem model domain used for simulations in Lambert Conformal projection with true latitude and longitude and center at 0°E/W, 50°N. Location of Eyjafjallajökull (63.62°N, 19.61°W) marked with red dot.

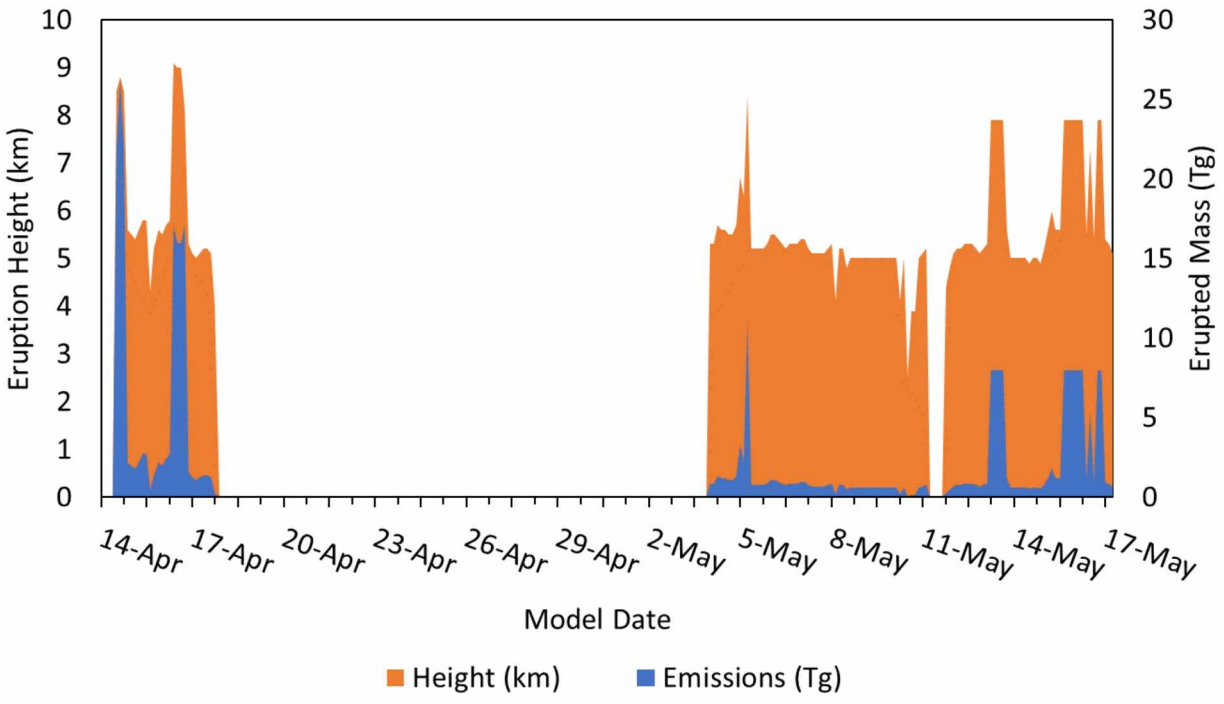

Figure 3.2 – Three hourly plume heights (KM) ASL (orange, km) and emitted mass (blue, Tg) used in the WRF-Chem modeling simulations (volc_d01.asc name list) for the eruption period April 12 until May 18, 2010. Values adapted from Hirtl et al., (2019) with dates as DD/MMM.

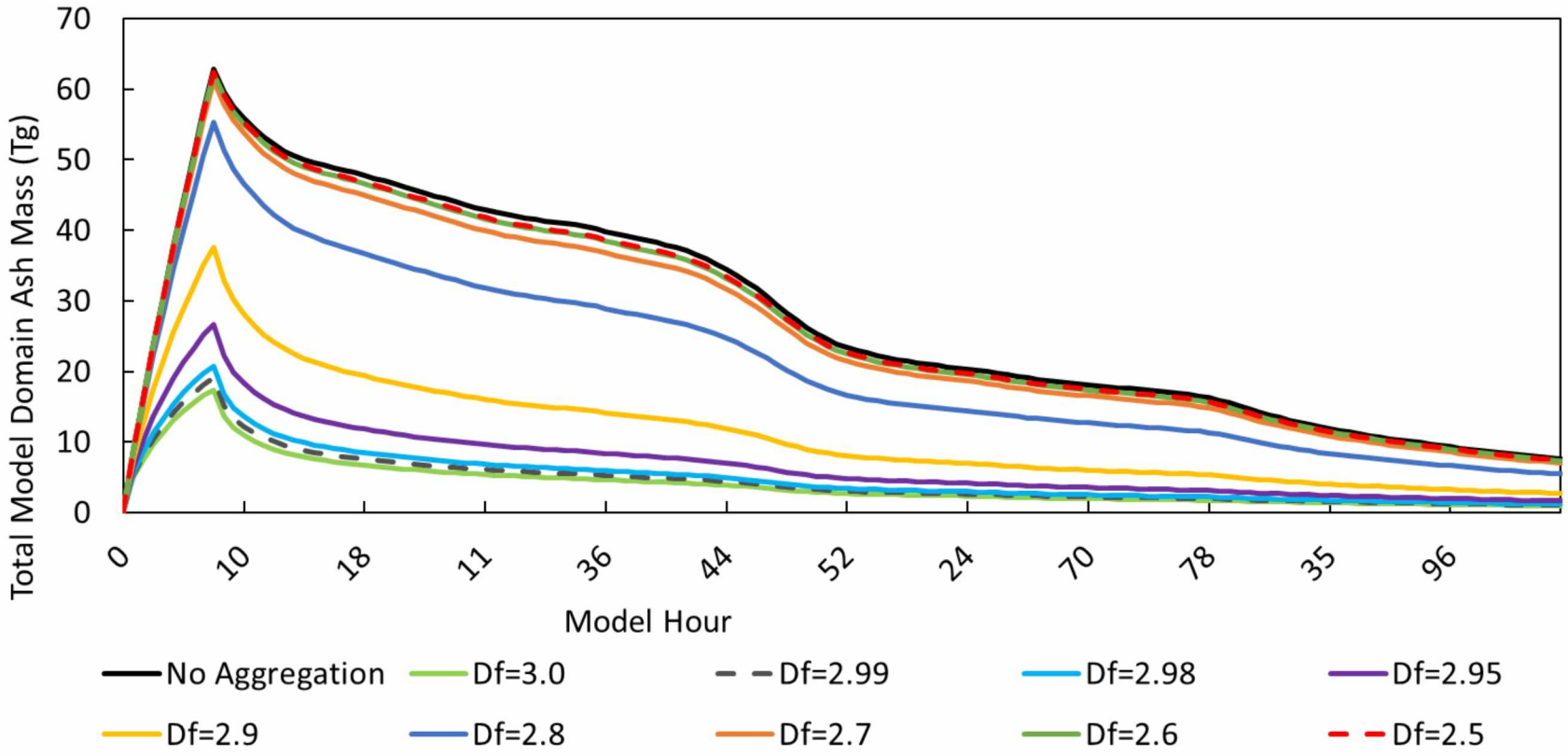

Figure 3.3 – Change in total domain ash mass, Tg, for a hypothetical eruption on May 5th, beginning 00:00UTC and ending 09:00UTC, for a range of fractal dimensions, D_f = {3.0, 2.99, 2.98, 2.95, 2.9, 2.8, 2.7, 2.6, 2.5}. Constant eruption rate = 4 x 10^6 kg s^{-1}. Time is given in hours since the onset of the eruption, 00:00UTC on May 5th.

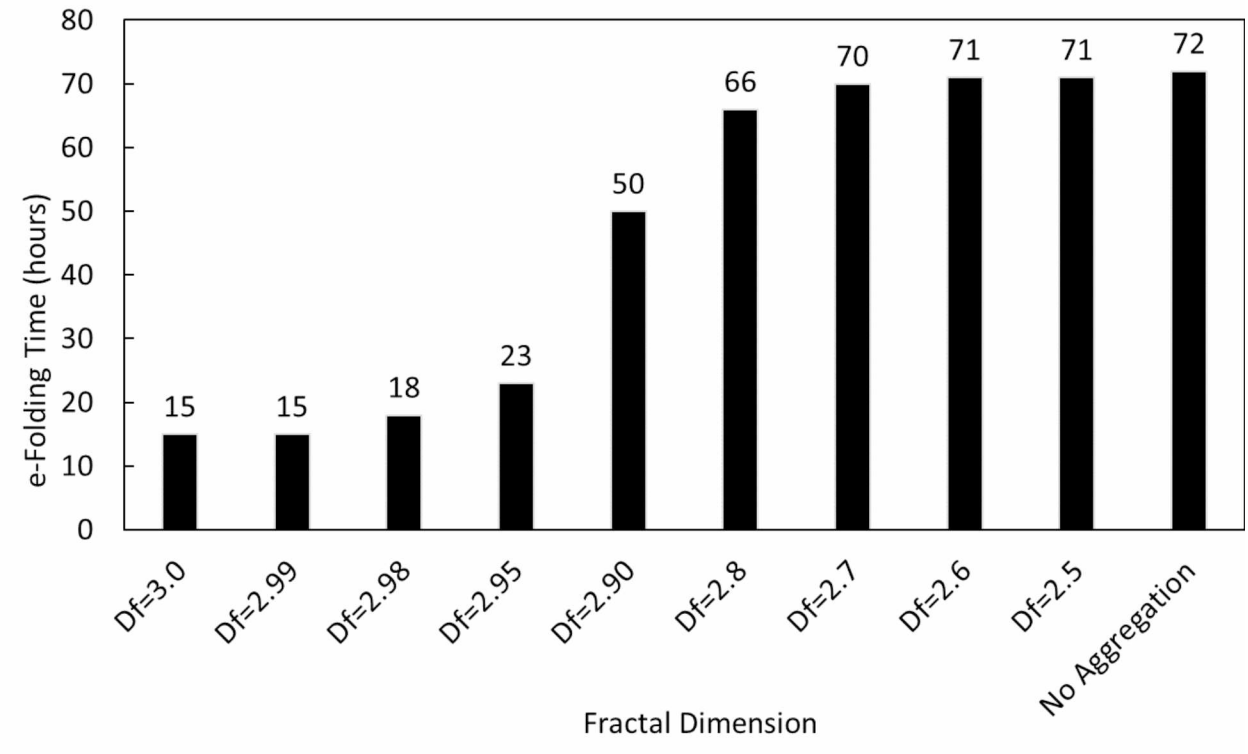

Figure 3.4 – Volcanic ash e-folding time in hours for a hypothetical eruption on May 5th, beginning 00:00Z and ending 09:00Z, for a range of fractal dimensions, D_f = {3.0, 2.99, 2.98, 2.95, 2.9, 2.8, 2.7, 2.6, 2.5}. Constant eruption rate = 4 x 10^6 kg s^{-1}.

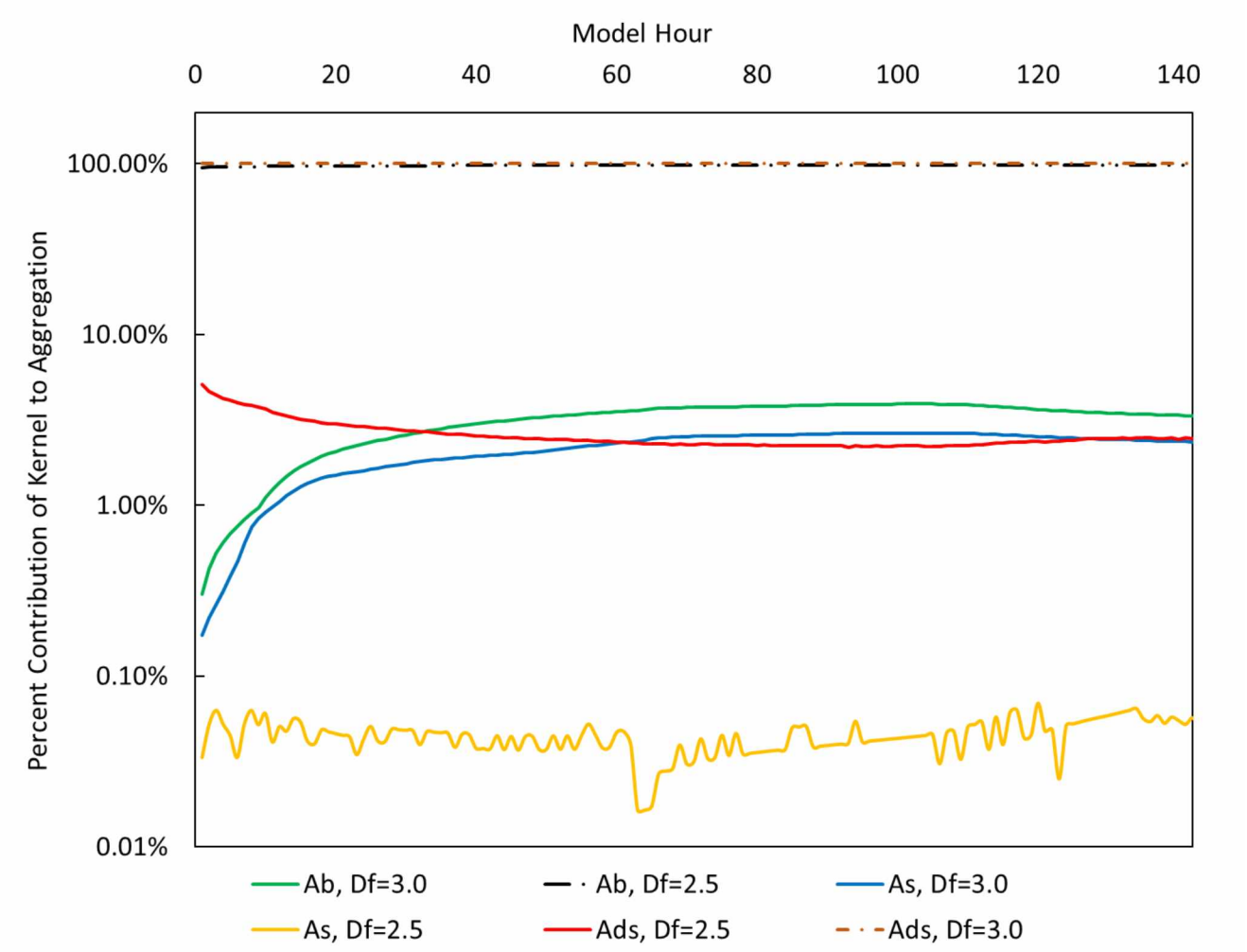

Figure 3.5 – Percentage of aggregation rate for each collision kernel (A_B = Brownian, A_S = Shear, A_{DS} = Differential Sedimentation) when considering a hypothetical eruption on May 5th, beginning 00:00UTC and ending 09:00UTC, for two fractal dimensions, D_f = {3.0, 2.5}. Constant eruption rate = 4 x 10^6 kg s^{-1}. Time is provided as hours since onset of eruption, 00:00UTC on May 5th.

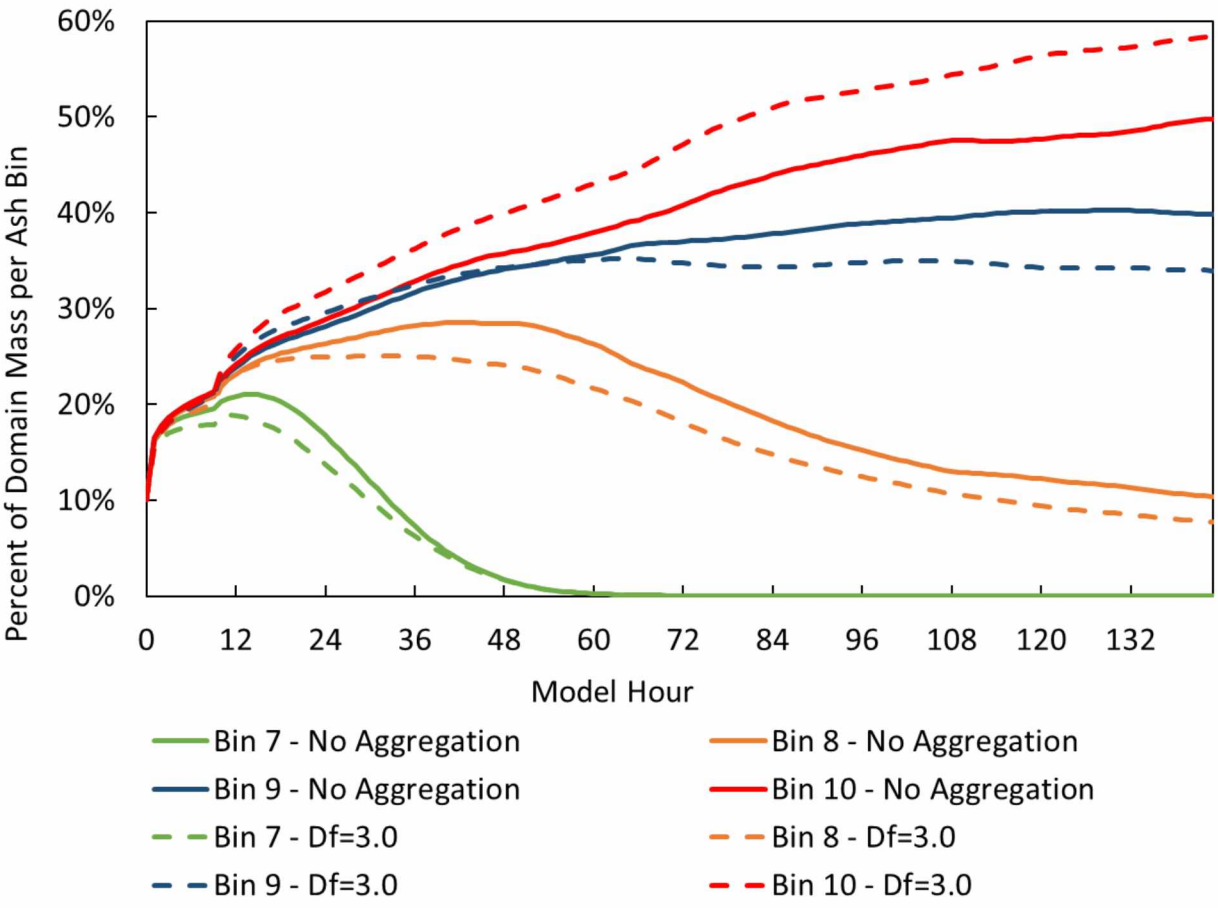

Figure 3.6 – Particle size distribution of volcanic ash bins 7 to 10 as percentages of total domain mass when considering a hypothetical eruption on May 5th, beginning 00:00Z and ending 09:00Z, and a fractal dimensions, D_f = 3.0. Constant eruption rate = 4 x 10^6 kg s^{-1}. Time is provided as hours since onset of eruption, 00:00UTC on May 5th.

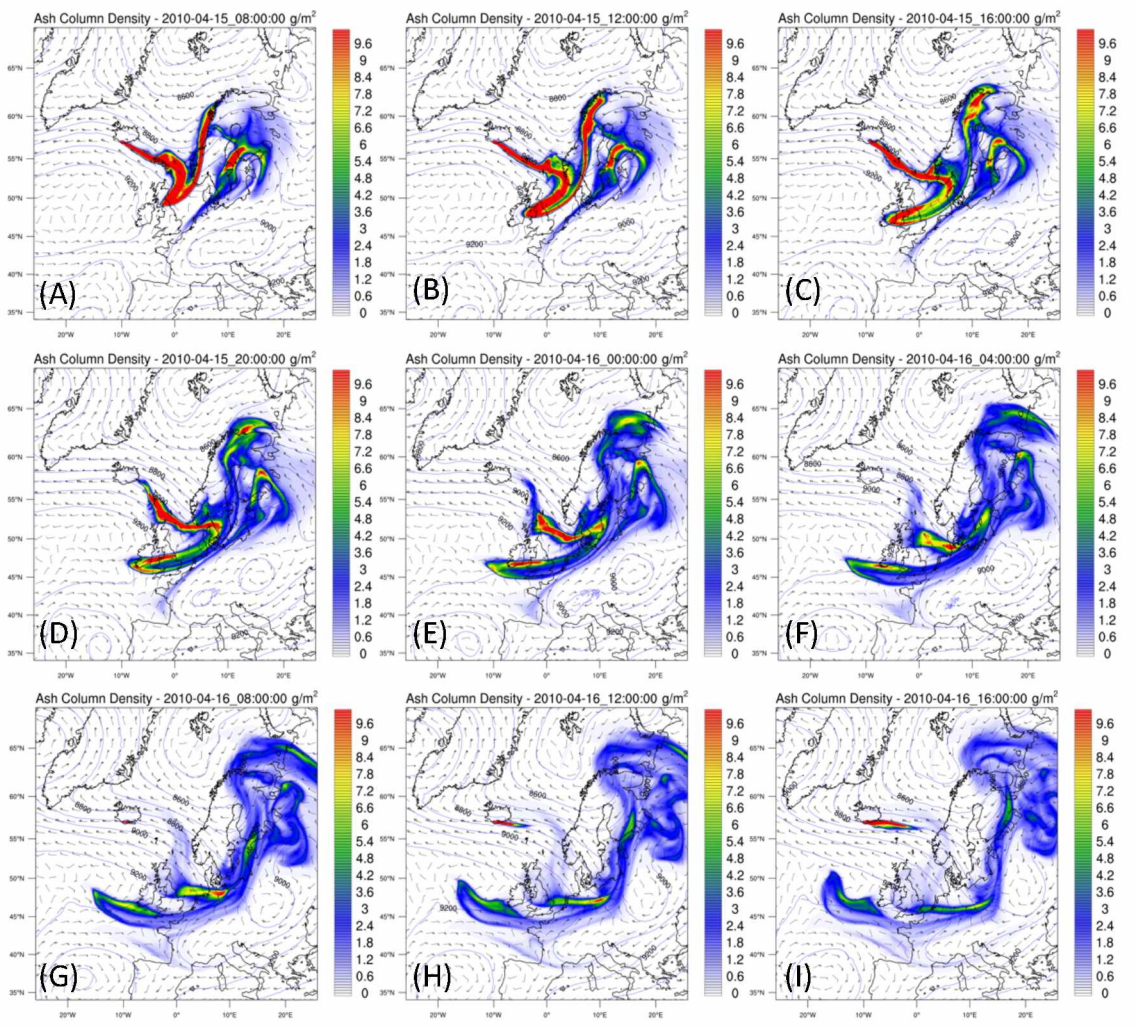

Figure 3.7 – WRF-Chem generated volcanic ash column densities for the Eyjafjallajökull eruption in April 2010 at four hour intervals, A = April 15 at 08 UTC, B = April 15 at 12 UTC, C = April 15 at 16 UTC, D = April 15 at 20 UTC, E = April 16 at 00 UTC, F = April 16 at 04 UTC, G = April 16 at 08 UTC, H = April 16 at 12 UTC, and I = April 16 at 16 UTC. Note each time output is at 00 hr.

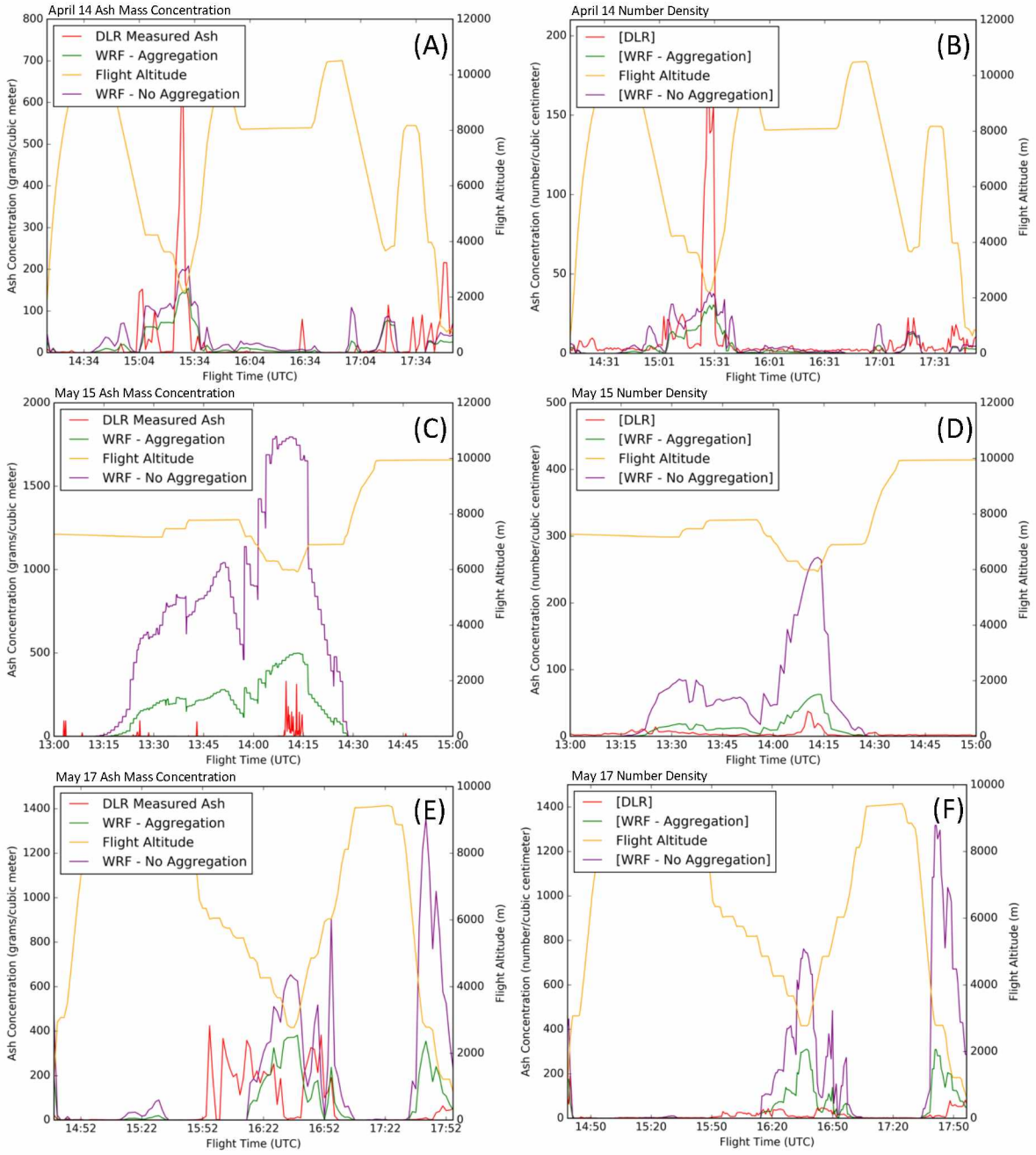

Figure 3.8 – Comparisons of WRF-Chem model output to in situ mass concentrations (left panels) and particle numbers (right panels) observed by DLR during April 19 (A and B), May 15 (C and D) and May 17 (E and F), 2010 flights.

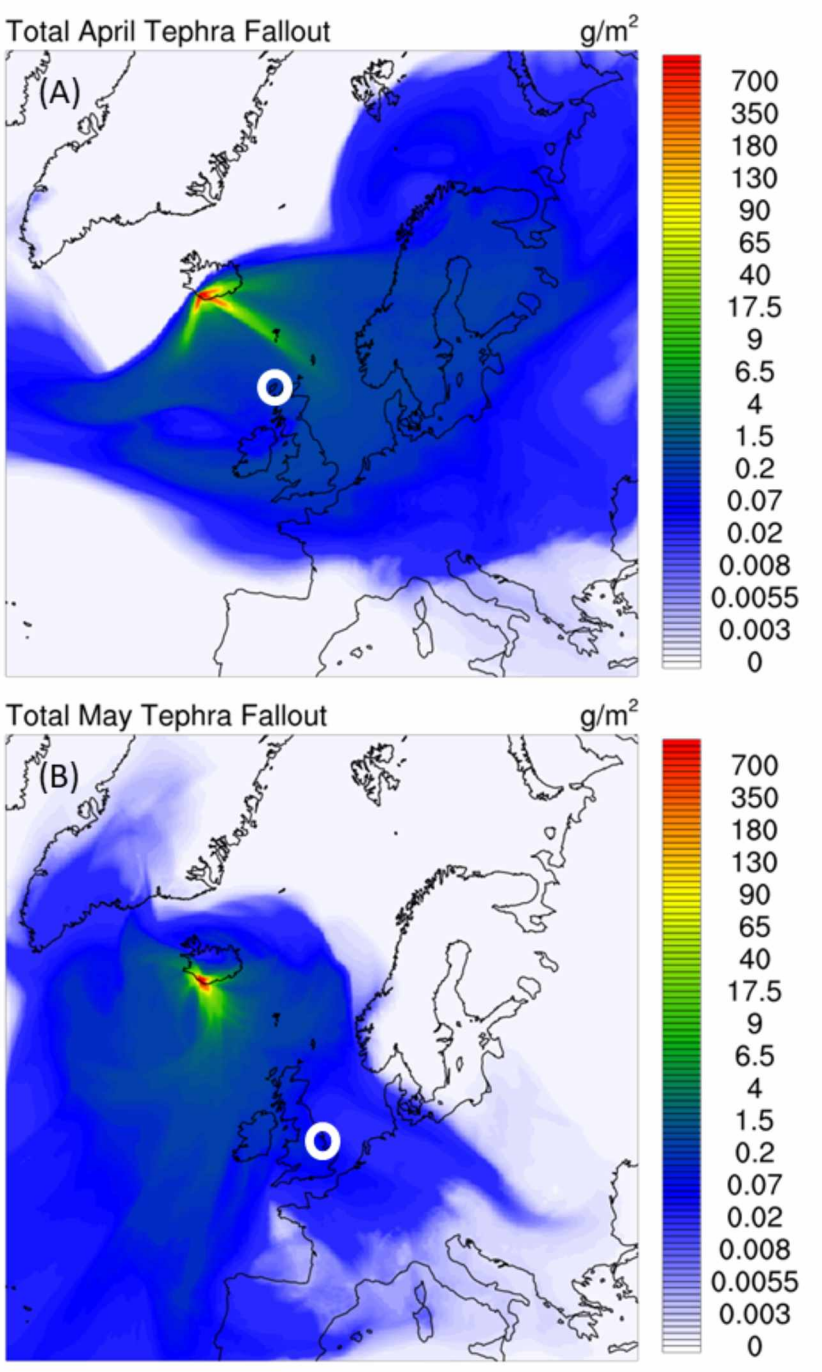

Figure 3.9 – Mass of tephra fallout deposited on model surface, lowest model level in WRF-Chem, for April (A,) and May (B) 2010 model simulations. White circle in (A) marks the Outer Hebrides and white circle in (B) marks Lincolnshire and Leicestershire, UK, corresponding to sample areas in Stevenson et al., (2012). Maximum domain fallout is 52 Mg m^{-2}.

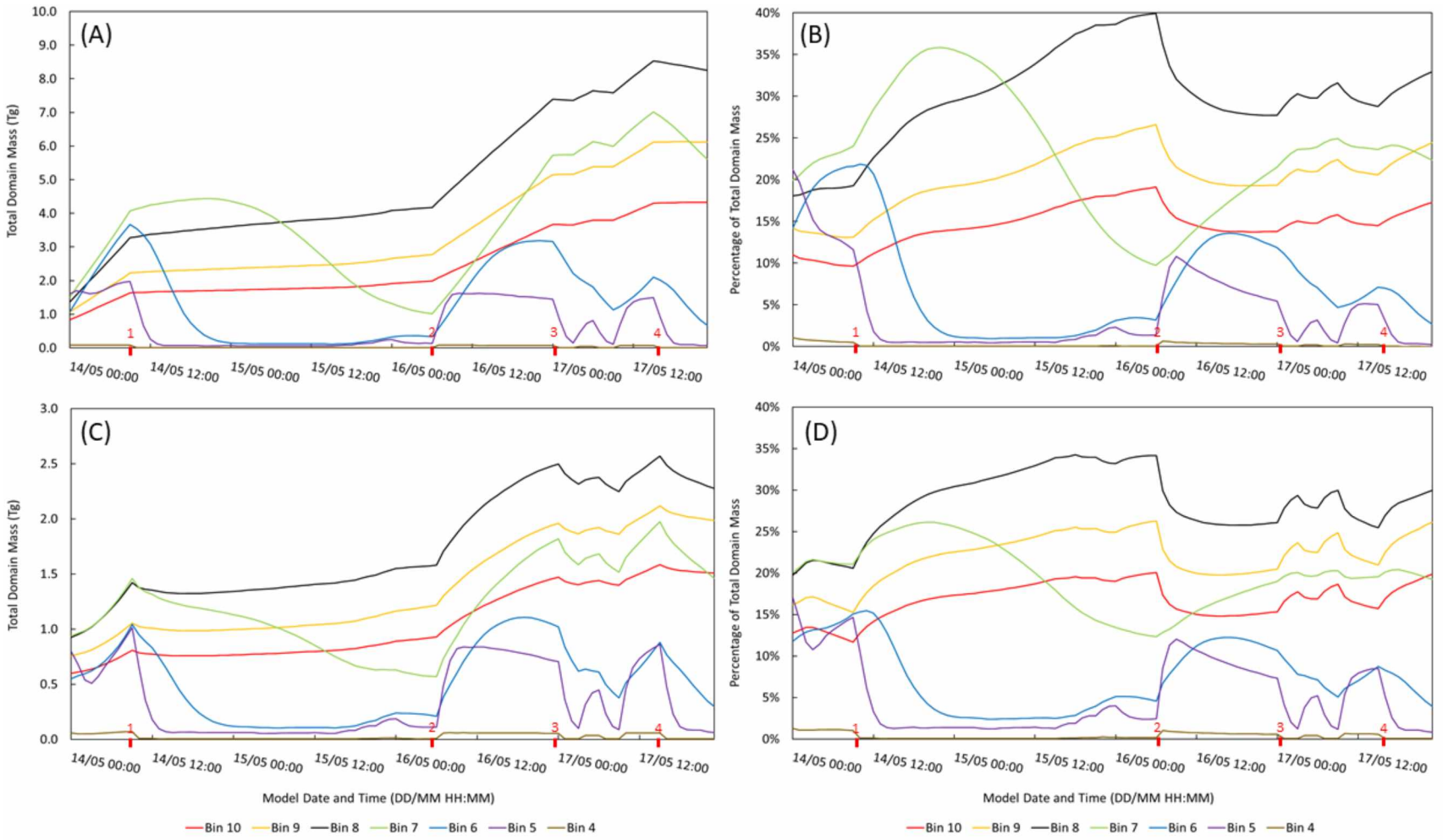

Figure 3.10 – Total domain ash mass (A, C) and percent contribution to domain mass (B, D) for the modeled period between 14 and 18 May, 2010 without (A, B – upper panels) and with (C, D – lower panels) aggregation code enabled. Red numbers on date/time axis denote major (> 10%) changes in the eruption rate.

TABLES

Table 3.1 – Derived coagulation kernel equations used in the calculation of ΔN. Units listed are those used natively in the calculation of the equations in the WRF-Chem driver files.

Kernel	Equation (#)	Variables and Units
Brownian Motion	$A_B = \frac{4kT}{3\mu}$ (3.2.3)	k_b – Boltzmann Constant - m^2 kg s^{-1} K^{-1} T – Temperature – K μ – Dynamic Viscocity - kg m^{-1} s^{-1} d – Diameter - m
Fluid Shear	$A_S = -\frac{2}{3}\xi^3 \Gamma_S$ (3.2.4)	Γ_s - Fluid Shear – s^{-1} d – Diameter – m ξ – Fractal dimension factor
Differential Sedimentation	$A_{DS} = \frac{\pi(\rho_p - \rho)g}{48\mu}\xi^4$ (3.2.5)	d – Diameter – m ξ – Fractal dimension factor ρ – Density of Air kg m^{-3} ρ_p – Density of primary particle kg m^{-3} V_d - Fall Velocity – m s^{-1}

Table 3.2 – Ash aggregation coefficients based on liquid water content, w/w, as described in Van Eaton et al., (2012).

Liquid Water Content (w/w)	Corresponding S value
0% (ice)	0.020
0-10%	0.008
10-15%	0.004
15-25%	0.002

Table 3.3 – Distribution of volcanic ash in model domain among 10 size bins.

Bin	Diameter	Percent Mass
1	1-2 mm	22.0
2	0.5-1 mm	5.0
3	0.25-0.5 mm	4.0
4	125-250 μm	5.0
5	62.5-125 μm	24.5
6	31.25-62.5 μm	12.0
7	15.625-31.25 μm	11.0
8	7.8125-15.625 μm	8.0
9	3.9065-7.8125 μm	5.0
10	<3.9065 μm	3.5

REFERENCES

Allard, P., Burton, M., Oskarsson, N., Michel, A. and Polacci, M.: Magmatic gas composition and fluxes during the 2010 Eyjafjallajökull explosive eruption: implications for degassing magma volumes and volatile sources, in Geophys. Res. Abstr, vol. 13., 2011.

Angell, J. K.: Comparison of stratospheric warming following Agung, El Chichon and Pinatubo volcanic eruptions, Geophys. Res. Lett., 20(8), 715–718, 1993.

Arason, P., Petersen, G. N. and Bjornsson, H.: Observations of the altitude of the volcanic plume during the eruption of Eyjafjallajökull, April–May 2010, Earth Syst. Sci. Data, 3(1), 9–17, doi:10.5194/essd-3-9-2011, 2011.

Boichu, M., Menut, L., Khvorostyanov, D., Clarisse, L., Clerbaux, C., Turquety, S. and Coheur, P.-F.: Inverting for volcanic SO2 flux at high temporal resolution using spaceborne plume imagery and chemistry-transport modelling: the 2010 Eyjafjallajökull eruption case-study, Atmospheric Chem. Phys., 13(17), 8569–8584, doi:10.5194/acp-13-8569-2013, 2013.

Bonadonna, C., Genco, R., Gouhier, M., Pistolesi, M., Cioni, R., Alfano, F., Hoskuldsson, A. and Ripepe, M.: Tephra sedimentation during the 2010 Eyjafjallajökull eruption (Iceland) from deposit, radar, and satellite observations, J. Geophys. Res. Solid Earth, 116(B12), B12202, doi:10.1029/2011JB008462, 2011.

Booth, B. and Walker, G. P. L.: Ash Deposits from the New Explosion Crater, Etna 1971, Philos. Trans. R. Soc. Lond. Math. Phys. Eng. Sci., 274(1238), 147–151, doi:10.1098/rsta.1973.0034, 1973.

Brown, R. J., Bonadonna, C. and Durant, A. J.: A review of volcanic ash aggregation, Phys. Chem. Earth Parts ABC, 45–46, 65–78, doi:10.1016/j.pce.2011.11.001, 2012.

Carey, S. N. and Sigurdsson, H.: Influence of particle aggregation on deposition of distal tephra from the May 18, 1980, eruption of Mount St. Helens volcano, J. Geophys. Res. Solid Earth, 87(B8), 7061–7072, doi:10.1029/JB087iB08p07061, 1982.

Casadevall, T. J.: The 1989–1990 eruption of Redoubt Volcano, Alaska: impacts on aircraft operations, J. Volcanol. Geotherm. Res., 62(1–4), 301–316, doi:10.1016/0377-0273(94)90038-8, 1994.

Chen, F. and Dudhia, J.: Coupling an Advanced Land Surface–Hydrology Model with the Penn State–NCAR MM5 Modeling System. Part I: Model Implementation and Sensitivity, Mon. Weather Rev., 129(4), 569–585, doi:10.1175/1520-0493(2001)129<0569:CAALSH>2.0.CO;2, 2001.

Chin, M., Rood, R. B., Lin, S.-J., Müller, J.-F. and Thompson, A. M.: Atmospheric sulfur cycle simulated in the global model GOCART: Model description and global properties, J. Geophys. Res., 105(D20), 24671–24,687, doi:10.1029/2000JD900384, 2000.

Cole-Dai, J.: Volcanoes and climate, Wiley Interdiscip. Rev. Clim. Change, 1(6), 824–839, doi:10.1002/wcc.76, 2010.

Cornell, W., Carey, S. and Sigurdsson, H.: Computer simulation of transport and deposition of the campanian Y-5 ash, J. Volcanol. Geotherm. Res., 17(1–4), 89–109, doi:10.1016/0377-0273(83)90063-X, 1983.

Costa, A., Folch, A. and Macedonio, G.: A model for wet aggregation of ash particles in volcanic plumes and clouds: 1. Theoretical formulation, J. Geophys. Res. Solid Earth, 115(B9), B09201, doi:10.1029/2009JB007175, 2010.

Dekkers, P. J. and Friedlander, S. K.: The Self-Preserving Size Distribution Theory: I. Effects of the Knudsen Number on Aerosol Agglomerate Growth, J. Colloid Interface Sci., 248(2), 295–305, doi:10.1006/jcis.2002.8212, 2002.

Devenish, B. J., Thomson, D. J., Marenco, F., Leadbetter, S. J., Ricketts, H. and Dacre, H. F.: A study of the arrival over the United Kingdom in April 2010 of the Eyjafjallajökull ash cloud using ground-based lidar and numerical simulations, Atmos. Environ., 48, 152–164, doi:10.1016/j.atmosenv.2011.06.033, 2012a.

Devenish, B. J., Francis, P. N., Johnson, B. T., Sparks, R. S. J. and Thomson, D. J.: Sensitivity analysis of dispersion modeling of volcanic ash from Eyjafjallajökull in May 2010, J. Geophys. Res. Atmospheres, 117(D20) [online] Available from: http://onlinelibrary.wiley.com/doi/10.1029/2011JD016782/full (Accessed 25 April 2016b), 2012.

Folch, A., Costa, A. and Macedonio, G.: FALL3D: A computational model for transport and deposition of volcanic ash, Comput. Geosci., 35(6), 1334–1342, doi:10.1016/j.cageo.2008.08.008, 2009.

Folch, A., Costa, A., Durant, A. and Macedonio, G.: A model for wet aggregation of ash particles in volcanic plumes and clouds: 2. Model application, J. Geophys. Res. Solid Earth, 115(B9), B09202, doi:10.1029/2009JB007176, 2010.

Folch, A., Costa, A. and Macedonio, G.: FPLUME-1.0: An integrated volcanic plume model accounting for ash aggregation, Geosci. Model Dev. Discuss., 8(9), 8009–8062, doi:10.5194/gmd-9-431-2016, 2016.

Gilbert, J. S. and Lane, S. J.: The origin of accretionary lapilli, Bull. Volcanol., 56(5), 398–411, doi:10.1007/BF00326465, 1994.

Gudmundsson, M. T., Thordarson, T., Höskuldsson, Á., Larsen, G., Björnsson, H., Prata, F. J., Oddsson, B., Magnússon, E., Högnadóttir, T., Petersen, G. N., Hayward, C. L., Stevenson, J. A. and Jónsdóttir, I.: Ash generation and distribution from the April-May 2010 eruption of Eyjafjallajökull, Iceland, Sci. Rep., 2, 572, doi:10.1038/srep00572, 2012.

Harris, A. J. L., Gurioli, L., Hughes, E. E. and Lagreulet, S.: Impact of the Eyjafjallajökull ash cloud: A newspaper perspective: Impact of the Eyjafjallajökull Ash Cloud, J. Geophys. Res. Solid Earth, 117(B9), doi:10.1029/2011JB008735, 2012.

Hirtl, M., Stuefer, M., Arnold, D., Grell, G., Maurer, C., Natali, S., Scherllin-Pirscher, B. and Webley, P.: The effects of simulating volcanic aerosol radiative feedbacks with WRF-Chem during the Eyjafjallajökull eruption, April and May 2010, Atmos. Environ., 198, 194–206, doi:10.1016/j.atmosenv.2018.10.058, 2019.

Hong, S.-Y., Noh, Y. and Dudhia, J.: A New Vertical Diffusion Package with an Explicit Treatment of Entrainment Processes, Mon. Weather Rev., 134(9), 2318–2341, doi:10.1175/MWR3199.1, 2006.

Jacobson, M. Z.: Fundamentals of atmospheric modeling, 2nd ed., Cambridge university press., 2005.

James, M. R., Lane, S. J. and Gilbert, J. S.: Density, construction, and drag coefficient of electrostatic volcanic ash aggregates, J. Geophys. Res. Solid Earth 1978–2012, 108(B9), doi:10.1029/2002JB002011, 2003.

Jullien, R. and Botet, R.: Aggregation and fractal aggregates, Ann Telecomm, 41, 343, 1987.

Keiding, J. K. and Sigmarsson, O.: Geothermobarometry of the 2010 Eyjafjallajökull eruption: New constraints on Icelandic magma plumbing systems, J. Geophys. Res. Solid Earth, 117(B9), doi:10.1029/2011JB008829, 2012.

Kristiansen, N. I., Stohl, A., Prata, A. J., Bukowiecki, N., Dacre, H., Eckhardt, S., Henne, S., Hort, M. C., Johnson, B. T., Marenco, F., Neininger, B., Reitebuch, O., Seibert, P., Thomson, D. J., Webster, H. N. and Weinzierl, B.: Performance assessment of a volcanic ash transport model mini-ensemble used for inverse modeling of the 2010 Eyjafjallajökull eruption, J. Geophys. Res. Atmospheres, 117(D20), doi:10.1029/2011JD016844, 2012.

Lee, C. and Kramer, T. A.: Prediction of three-dimensional fractal dimensions using the two-dimensional properties of fractal aggregates, Adv. Colloid Interface Sci., 112(1–3), 49–57, doi:10.1016/j.cis.2004.07.001, 2004.

Lin, J., Brunner, D., Gerbig, C., Stohl, A., Luhar, A. and Webley, P.: Lagrangian Modeling of the Atmosphere, American Geophysical Union., 2012.

Mastin, L. G., Guffanti, M., Servranckx, R., Webley, P., Barsotti, S., Dean, K., Durant, A., Ewert, J. W., Neri, A., Rose, W. I., Schneider, D., Siebert, L., Stunder, B., Swanson, G., Tupper, A., Volentik, A. and Waythomas, C. F.: A multidisciplinary effort to assign realistic source parameters to models of volcanic ash-cloud transport and dispersion during eruptions, J. Volcanol. Geotherm. Res., 186(1–2), 10–21, doi:10.1016/j.jvolgeores.2009.01.008, 2009.

Mastin, L. G., Bonadonna, C., Folch, A., Stunder, B. J., Webley, P. W. and Pavolonis, M. J.: Summary of data on well-documented eruptions for validation of volcanic ash transport and dispersal models, VHub.org [online] Available from: https://vhub.org/resources/4044/download/summary_table_2016.06.11.htm (Accessed 19 September 2016), 2014.

Miller, T. P. and Casadevall, T. J.: Volcanic ash hazards to aviation, Encycl. Volcanoes, 915–930, 2000.

NCAR: NCEP FNL Operational Model Global Tropospheric Analyses, continuing from July 1999, [online] Available from: https://rda.ucar.edu/datasets/ds083.2/ (Accessed 7 February 2019), 2000.

Peckham, S. E., Grell, G., McKeen, S., Barth, M., Pfister, G., Wiedinmyer, C., Fast, J. D., Gustafson, W. I., Zaveri, R. A. and Easter, R. C.: WRF/Chem Version 3.9 User's Guide, US Department of Commerce, National Oceanic and Atmospheric Administration, Oceanic and Atmospheric Research Laboratories, Global Systems Division. [online] Available from: https://ruc.noaa.gov/wrf/wrf-chem/Users_guide.pdf, 2018.

Prata, A. J. and Prata, A. T.: Eyjafjallajökull volcanic ash concentrations determined using Spin Enhanced Visible and Infrared Imager measurements, J. Geophys. Res. Atmospheres 1984–2012, 117(D20), doi:10.1029/2011JD016800, 2012.

Rose, W. I. and Durant, A. J.: Fine ash content of explosive eruptions, J. Volcanol. Geotherm. Res., 186, 32–39, doi:10.1016/j.jvolgeores.2009.01.010, 2009.

Rose, W. I. and Durant, A. J.: Fate of volcanic ash: Aggregation and fallout, Geology, 39(9), 895–896, doi:10.1130/focus092011.1, 2011.

Schumacher, R. and Schmincke, H.-U.: Models for the origin of accretionary lapilli, Bull. Volcanol., 56(8), 626–639, doi:10.1007/BF00301467, 1995.

Schumann, U., Weinzierl, B., Reitebuch, O., Schlager, H., Minikin, A., Forster, C., Baumann, R., Sailer, T., Graf, K., Mannstein, H., Voigt, C., Rahm, S., Simmet, R., Scheibe, M., Lichtenstern, M., Stock, P., Ruba, H., Schauble, D., Tafferner, A., Rautenhaus, M., Gerz, T., Ziereis, H., Krautstrunk, M., Mallaun, C., Gayet, J. F., Lieke, K., Kandler, K., Ebert, M., Weinbruch, S., Stohl, A., Gasteiger, J., Gross, S., Freudenthaler, V., Wiegner, M., Ansmann, A., Tesche, M., Ólafsson,

H. and Sturm, K.: Airborne observations of the Eyjafjalla volcano ash cloud over Europe during air space closure in April and May 2010, Atmos Chem Phys, 11(5), 2245–2279, 2011.

Smoluchowski, M.: Investigation of a Mathematical Theory on the Coagulation of Colloidal Suspensions, Z Phys. ChemGer, 92, 155, 1917.

Sorem, R. K.: Volcanic ash clusters: Tephra rafts and scavengers, J. Volcanol. Geotherm. Res., 13(1), 63–71, doi:10.1016/0377-0273(82)90019-1, 1982.

Sparks, R. J. S., Burski, M. I., Carey, S. N., Gilbert, J. S., Glaze, L. S., Siquerdsson, H. and Woods, A. W.: Volcanic Plumes, John Wiley and Sons, Sussex, England., 1997.

Stevenson, J. A., Loughlin, S., Rae, C., Thordarson, T., Milodowski, A. E., Gilbert, J. S., Harangi, S., Lukács, R., Højgaard, B., Árting, U., Pyne-O'Donnell, S., MacLeod, A., Whitney, B. and Cassidy, M.: Distal deposition of tephra from the Eyjafjallajökull 2010 summit eruption, J. Geophys. Res. Solid Earth, 117(B9), doi:10.1029/2011JB008904, 2012.

Stockwell, W. R., Middleton, P., Chang, J. S. and Tang, X.: The second generation regional acid deposition model chemical mechanism for regional air quality modeling, J. Geophys. Res., 95(D10), 16343–16,367, doi:10.1029/JD095iD10p16343, 1990.

Stohl, A., Prata, A. J., Eckhardt, S., Clarisse, L., Durant, A., Henne, S., Kristiansen, N. I., Minikin, A., Schumann, U., Seibert, P., Stebel, K., Thomas, H. E., Thorsteinsson, T., Tørseth, K. and Weinzierl, B.: Determination of time-and height-resolved volcanic ash emissions and their use for quantitative ash dispersion modeling: the 2010 Eyjafjallajökull eruption, Atmos Chem Phys, 11(9), 4333–4351, doi:10.5194/acp-11-4333-2011, 2011.

Stuefer, M., Freitas, S. R., Grell, G., Webley, P., Peckham, S., McKeen, S. A. and Egan, S. D.: Inclusion of ash and SO 2 emissions from volcanic eruptions in WRF-Chem: development and some applications, Geosci. Model Dev., 6(2), 457–468, doi:doi.org/10.5194/gmd-6-457-2013, 2013.

Taddeucci, J., Scarlato, P., Montanaro, C., Cimarelli, C., Bello, E. D., Freda, C., Andronico, D., Gudmundsson, M. T. and Dingwell, D. B.: Aggregation-dominated ash settling from the Eyjafjallajökull volcanic cloud illuminated by field and laboratory high-speed imaging, Geology, 39(9), 891–894, doi:10.1130/G32016.1, 2011.

Thomas, H. E. and Prata, A. J.: Sulphur dioxide as a volcanic ash proxy during the April–May 2010 eruption of Eyjafjallajökull volcano, Iceland, Atmos Chem Phys, 11(14), 6871–6880, 2011.

Thordarson, T. and Self, S.: Atmospheric and environmental effects of the 1783–1784 Laki eruption: A review and reassessment, J. Geophys. Res. Atmospheres, 108(D1), AAC 7-1-AAC 7-29, doi:10.1029/2001JD002042, 2003.

Van Eaton, A. R., Muirhead, J. D., Wilson, C. J. and Cimarelli, C.: Growth of volcanic ash aggregates in the presence of liquid water and ice: an experimental approach, Bull. Volcanol., 74(9), 1963–1984, 2012.

Van Eaton, A. R., Mastin, L. G., Herzog, M., Schwaiger, H. F., Schneider, D. J., Wallace, K. L. and Clarke, A. B.: Hail formation triggers rapid ash aggregation in volcanic plumes, Nat. Commun., 6, 7860, doi:10.1038/ncomms8860, 2015.

Waitt, R. B., Hansen, V. L., Sarna-Wojcicki, A. M. and Wood, S. H.: Proximal air-fall deposits of eruptions (of Mount St. Helens) between May 24 and August 7, 1980 - stratigraphy and field sedimentology., US Geol. Surv. Prof. Pap., 1250, 617–628, 1981.

Wallace, K. L., Schaefer, J. R. and Coombs, M. L.: Character, mass, distribution, and origin of tephra-fall deposits from the 2009 eruption of Redoubt Volcano, Alaska—Highlighting the significance of particle aggregation, J. Volcanol. Geotherm. Res., 259, 145–169, doi:10.1016/j.jvolgeores.2012.09.015, 2013.

Webley, P. W., Steensen, T., Stuefer, M., Grell, G., Freitas, S., Pavolonis, M.: Analysing the Eyjafjallajökull 2010 eruption using satellite remote sensing, lidar and WRF-Chem dispersion and tracking model, J. Geophys. Res. Atmospheres, 117(D20), doi:10.1029/2011JD016817, 2012.

Young, C. L., Sokolik, I. N. and Dufek, J.: Regional radiative impact of volcanic aerosol from the 2009 eruption of Mt. Redoubt, Atmospheric Chem. Phys., 12(8), 3699–3715, doi:10.5194/acp-12-3699-2012, 2012.

CHAPTER 4 – NEAR REAL-TIME VOLCANIC ASH FORECASTING WITH THE WEATHER RESEARCH FORECASTING WITH CHEMISTRY (WRF-CHEM) MODEL

ABSTRACT

The Weather Research Forecasting with Chemistry (WRF-Chem) model was modified to be used as a near real-time volcanic ash transport and dispersion (VATD) model. A suite of scripts was developed to review websites maintained by the world's Volcanic Ash Advisory Centers (VAAC) such that advisories and warnings trigger an automatic launch of the model based on the advisory or warning text. Furthermore, the model was modified such that it includes 10 user defined model members at 5 different heights and 2 particle sizes, thus covering a range of initial conditions with one model run. Automatic post processing scripts were developed to generate volcanic ash concentration plots with suggested no fly zones in red, total column volcanic ash density plots and an overall skill score of the model data that is established by comparing model output to available hyperspectral satellites in the appropriate area of coverage. This automated model suite was applied to the June 21, 2019 eruption of Raikoke in the Kurile Islands. The model generated output with a lag time of 1.5 hours, which accounts for lag between the eruption onset and production of the Tokyo VAAC warning. The skill score in this case was 64% with a standard deviation of 13%, established by comparing pixels from Himawari-8 brightness temperature differences to model domain ash column densities. The near real-time turnaround of this product suggests it may be used as an additional source of information alongside operational VATD models.

4.1 INTRODUCTION

Volcanic ash and sulfur dioxide plumes pose numerous hazards to aviation communities. Ash in particular may cause seizing of jet engines, decrease visibility, damage the fuselage of aircraft, and potentially clog fuel lines (Blong, 1984; Miller and Casadevall, 2000). These ash-aviation hazards sometimes lead to extensive economic impacts. The 2010 eruption of Eyjafjallajökull Volcano in Iceland, for example, closed air space over Europe for two weeks resulting in over €3.3 billion in economic losses (Harris et al., 2012; Marzzocchi et al., 2010).

National defense readiness may also be impacted when volcanoes erupt near large military installations. The 1991 eruption of Mount Pinatubo in the Philippines, for example, covered Clark Air Force Base in volcanic ash resulting in extensive damage to facilities (Casadevall et al., 1996). Alaska, a state with over 50 recently active volcanoes (Miller et al., 1998), is also home to over a dozen national defense sites (Hildreth, 2001), and is particularly vulnerable to large eruptions. The 2009 Redoubt Volcano eruption dispersed ash far into the interior of the state and interrupted civilian and military air traffic (Bull and Buurman, 2013; Webley et al., 2013).

Expedient identification, proper communication between communities, and accurate forecasting of volcanic plume characteristics and transport are vital to aviation safety and hazard mitigation. Over the past two decades, the International Civil Aviation Organization (ICAO) has established protocols for the identification of volcanic eruptions, the tracking and forecasting of their ash plumes, and methods to deliver plume transport forecasts and information to the appropriate agencies in order to mitigate associated hazards (International Civil Aviation Organization, 2004). These protocols require input from a number of scientific communities, reflecting the interdisciplinary nature of forecasting volcanic ash transport. To help coordinate responses to volcanic eruptions, the ICAO established nine Volcanic Ash Advisory Centers (VAACs). These nine centers, shown in Figure 4.1, are responsible for analyzing volcanic eruptions, tracking resulting ash clouds within their respective airspace and providing advisories and guidance to the public.

The VAACs rely on a number of inputs to generate their advisory products. For example, near real-time satellite remote sensing data provide important information regarding the current state of volcanic ash plumes and clouds (Miller and Casadevall, 2000; Webley and Mastin, 2009). Seismographic measurements help constrain volcanic eruption onset time (Brenguier et al., 2008; Chouet and Matoza, 2013; Herrmann, 2013; Sparks, 2003; Sparks et al., 2012) . Additionally, numerical weather prediction (NWP) and volcanic ash transport and dispersion (VATD) models are routinely used to forecast the transport of volcanic ash clouds (Peterson and Dean, 2008). VATD models such as Puff, Hybrid Single Particle Lagrangian Integrated Trajectory Model (HYSPLIT) and FLEXible PARTicle dispersion model (FLEXPART) are used as operational tools at various VAAC centers and observatories around the world (Searcy et al., 1998; Draxler and Rolph 2003; Stohl et al. 2011 respectively). For example, the Alaska Volcano Observatory

(AVO) uses Ash3D, the U.S. Air Force and Washington VAACs use HYSPLIT, and the Anchorage VAAC uses Puff. For a list of VATD examples, refer to Table 1.2.

Volcanic ash undergoes dispersion via numerous atmospheric and microphysical processes that complicate modeling efforts (Brown et al., 2012). For example, the condensation of entrained water may increase the convective buoyancy of a plume via the release of latent heat, increasing the height of the eruption by many kilometers above their otherwise dry air height maxima (Sparks et al., 1997; Woods, 1993). Increased plume heights may result in increased transport of volcanic ash due to higher wind speeds aloft. In addition, ice nucleation not only increases plume buoyancy through latent heat release but also may enhance the removal of volcanic ash through increased aggregation rates, such as in the case of the Mount St. Helens eruption (Brown et al., 2012; Durant et al., 2008; Rose and Durant, 2011). Atmospheric conditions such as the height of the tropopause, wind shear and turbulence also affect the transport and lifetime of volcanic ash (Carey and Sparks 1986; Tupper et al. 2009).

Many VATD models are capable of capturing and representing these complex physical processes in their downwind forecasts of the ash cloud locations and concentrations. For example, the Active Tracer High Resolution Atmospheric Model, or ATHAM, is a non-hydrostatic model that fully conserves mass and thus supports the study of volcanic ash sources and sinks (Graf et al., 2002) but is computationally very expensive when compared to operational VATD models (Oberhuber et al., 1998). Fall3D is another model that is capable of capturing wet volcanic ash aggregation when used alongside NWP models, and thus allows for the forecasting and prediction of volcanic ash fallout (Carey and Sparks 1986; Folch, Costa, and Macedonio 2009). Additionally, there is the Weather Research Forecasting with Chemistry (WRF-Chem) model, a non-hydrostatic, fully compressible, air chemistry model that is also capable of modeling volcanic ash and sulfur dioxide (SO_2) (e.g. Stuefer et al. 2013; Grell et al. 2005; Peckham et al. 2018; Egan et al. 2015). The fully coupled nature of the WRF-Chem physics and chemistry routines to the dynamics solver allows their impacts on local meteorology to be captured at each model time step.

WRF-Chem has been used to model dispersion of the SO_2, such as in a model study of the cloud generated by the 2007 eruption of Kasatochi Volcano, Alaska. In this case, coupled chemistry routines helped establish an atmospheric lifetime of SO_2. As discussed in Chapter 3 of this manuscript, aggregation processes have been coupled to the model solver. Application of

aggregation to the 2010 eruption of Eyjafjallajökull showed that aggregation processes may reduce the lifetime of volcanic ash by up to 80%, greatly reducing the total duration of the hazard posed. Recently, Hirtl et al. (2019) demonstrated that including ash radiative feedback parameterizations while also modeling Eyjafjallajökull improved model solutions when compared to radiosonde data. In this case, differences up to 2 m s^{-1} wind speeds were realized, which affects the distance ash may travel before settling. Additionally, including radiative feedbacks allowed the model to capture inversion events. Lapse rate inversions may affect the buoyancy and vertical profile of volcanic ash plumes, further affecting downwind transport. This coupled nature makes WRF-Chem a good candidate for near real time modeling of volcanic ash and SO_2 dispersion and chemistry.

All VATD models, including WRF-Chem, require a set of initial conditions in order to predict the dispersion of volcanic ash after an eruptive event. These eruption source parameters (ESP) are often derived from a mix of remote sensing observations, from warnings and alerts provided by VAACs or volcano observatories, or through the use of well-established, tabulated eruption types and particle size distributions (Mastin et al., 2009; Webley et al., 2009). These ESP terms provide information about the expected total mass and plume height of a volcanic eruption, and the distribution of mass to be assigned to ash particle size bins in VATD models. The uncertainty associated in these parameters can propagate into the model output, but in many cases may be the only source of eruption information when direct or remote measurements are unavailable (Webley and Mastin, 2009; Webley, 2017).

This study details modifications to WRF-Chem in order to augment it for use as a near real time VATD tool. This is accomplished in two ways. First, the model code is updated to include ten different initial conditions with varying heights and particle sizes such that ten different sets of model output are available from one model run. Second, an automated process is developed such that the model automatically queues based on receipt of alerts from user specified VAACs, volcano observatories or other sources. The following Section 4.2 (Model Modifications) discusses the modifications made to WRF-Chem that enable the use of these ten different initial conditions and describes the automation methodology used. Section 4.3 (Case Study – Raikoke Eruption) details the application of this newly automated, near real time WRF-Chem tool to the 2019 eruption of Raikoke in the Kurile Islands. Section 4.4 (Discussion) provides analysis of the Raikoke eruption

output from this case study. Finally, Section 4.5 (Conclusions) concludes with closing remarks on the model's application for near real-time ash cloud dispersion and its possible use in hazard mitigation and decision making.

4.2 Model Modifications

In this modified version of WRF-Chem the original emissions and chemistry drivers have been removed and replaced with new code that generates 10 sets of model solutions in a single run. Each solution corresponds to one of 5 user defined plume heights, and one of two user defined particle sizes. These two factors, plume height and particle size, were chosen as they are sources of great uncertainty in model forecasts. Plume heights, for example, experience different dynamical effects as synoptic features change with altitude. Additionally, particle size affects the residence time of ash as larger particles have smaller residence times than fine ash particles.

Each of the five plume heights are initialized following the approaches in Hirtl et al. (2019) using a linear eruption column with eruption rates and durations specified at explicit heights. A single height is read into the model from an eruption source parameter name list. This same name list includes four height offsets, two above and two below, the height specified. In this study, these height offsets are set at the default values of 0.3, 0.7, 1.0, 1.5 and 3.0 times the input height, although these may be modified by the user as needed.

The WRF-Chem volcanic ash package (known as chemistry option 402) includes ten different volcanic ash size bins (Table 4.1) that correspond to the Φ size distribution as developed by Krumbein (1934). To capture the effects of both proximal and distal volcanic ash settling, WRF-Chem was modified to initialize each of the five plume heights into two particle size bins which may be specified by the user prior to compilation of the code. In this study, particle sizes corresponding to WRF-Chem bins 8 and 10 were chosen. These particles settle at different velocities, due to their size, and therefore have different atmospheric lifetimes. For example, bin 10, the finest ash bin in WRF-Chem, corresponds to $\Phi > 8$, or particles less than 3.9065 μm. From previous modeling studies in Chapter 3 of this manuscript, particles of this size have an e-folding time on the order of 120 hours, on average. Therefore, it takes 5 days for the model domain mass in bin 10 to decrease to 37% of the original mass. Bin 8, on the other hand, corresponds to $\Phi = 6$-7, or particles of between 7.8125 and 15.625 μm in diameter. These larger particles settle faster

with an atmospheric lifetime of less than 2 days (46 hours), resulting in both proximal and distal deposition. The selection of these two bins therefore covers both proximal, short lived ash clouds as well as distal, long lived clouds.

A naming convention was developed to ease the discussion of the 10 model members (Table 4.2). The first letter of the member name represents the size of the particle with s corresponding to the smaller and l corresponding to the larger. The last letter(s) in CAPS represent the height offset with LL the lowest, LM the lower middle, M the center level, UM the upper middle and UU the highest.

The modified WRF-Chem near real time code was also setup to initialize automatically based on certain triggering events (see workflow in Figure 4.2). Scripts were built to routinely analyze VAAC websites and Rich Site Summaries (RSS) feeds (Guffanti and Miller, 2013) as well as ingest text alerts from various partner agencies. A sample of these scripts are available for download using "git" commands and the repository located at github.com/sdegan-USN/real_time_wrf. The scripts parse through text from these sources and search for terms that suggest an eruption is either imminent or has already occurred. For example, a VAAC alert with the word ORANGE, indicating a heighted volcanic unrest, triggers the start of a model simulation for the volcano listed in the alert. Additional scripts may be created and custom tailored by users and incorporated into the beginning of the model initialization cascade that follows.

A triggering event results in the creation of a new WRF-Chem volcanic run directory along with the input files required by the model. These files are generated using the WRF Preprocessing System (or WPS) version 3.9. The WPS generates a model domain using GFS meteorological fields and geographical static data available at the University Center for Academic Research Advanced Research WRF website (Peckham et al., 2018). The startup scripts automatically launch WPS and generate a model domain of 400 by 400 grid cells with 32 pressure levels at a 7.5 km spatial resolution, centered on the volcano in question. These model domain specifications are listed in Table 4.3.

The eruption source parameters are written to the "volc_d01.asc" name list based on the source of the data. If a data source, such as a VAAC alert, provides an estimated plume height, this will be used to calculate the five plume heights for the WRF-Chem simulations. If no height

estimate is provided or is unavailable, tabulated values from eruption source parameters developed by Mastin et al. (2009) and compiled by Freitas et al. (2011) are used. The other four heights are calculated from the offsets specified by the user (defaults scaled by 0.3, 0.7, 1.5 and 3 times). Logic has been added to ensure ash is injected in the model level directly above the vent should the offset specify a subterranean emission height. The scripts then use the same tabulated eruption information to develop the remaining emissions inputs such as the eruption duration and mass emission rate.

After the automatic initialization, the model is run for 72 hours with a 24 hour spin up time preceding the model eruption time. WRF-Chem model output is stored in NetCDF format at 12-hour increments and post-processing of the model simulations begins with each completion of the 12-hourly output files. A post-processing suite of scripts, also available at the "real_time_wrf" repository, was created to aid in the visualization of the model solutions at user defined flight levels. In this study, four flight levels (FL) of interest to the US Navy were chosen. FL100 (10,000 feet a.s.l.) is a low altitude level that would be of interest for smaller commercial and recreational planes as well as flight routes as they approach and leave from an airport. FL330 (33,000 ft. a.s.l.) and FL350 (35,000 ft. a.s.l.) are commonly used for commercial jet planes and large military aircraft. FL420 (42,000 ft. a.s.l.) is used by private jets and military fighter jets and reconnaissance craft.

ICAO standards restrict flights to "enhanced flight operations" when volcanic ash concentrations exceed 2,000 μg m^{-3} and restrict any flight operations at concentrations of 2 g m^{-3} (Alexander, 2013; Casadevall, 1992; Miller and Casadevall, 2000). The automated WRF-Chem post processing products use these ICAO standards to generate outputs with areas of "enhanced flight operations" in yellow and areas with "restricted flight operations" in red. The use of this two-color scheme system, used by the US Navy, facilitates decision making to provide a sharp contour between safe (clear), hazardous (yellow), and restricted (red) flying conditions. Additionally, this color system is a simple and effective approach to visualize the hazards zones for volcanic eruptions and communicate the importance of their impact (De la Cruz-Reyna and Tilling, 2008).

4.3 Case Study Raikoke Eruption

Raikoke [48.29N, 153.25E], a small stratovolcano with a summit of only 551 m, sits in the middle of the Kurile Islands, south of Russia's Kamchatka peninsula. After 95 years of dormancy, the island volcano erupted powerfully with a series of 9 explosions beginning June 21 at 18:50UTC and produced plumes 10-13 km in height (Sennert, 2019). Toyko VAAC produced an initial warning (FVFE01 RJTD 211928 DTG 20190621/1928Z) 38 minutes later at 19:28UTC based on retrievals from Himawari-8 that indicated a plume affecting flight levels up to FL340 moving East-Northeast at 40 knots. The initial warning graphic for the referenced MANOP above is provided in Figure 4.3 and the initial forecast image is depicted in Figure 4.4.

Prata (1989a, b) developed methodologies for the detection of volcanic ash by establishing brightness temperature differences (BTD) between different infrared (IR) channels. These methods have been applied globally for the detection of volcanic ash on a variety of satellite platforms. Analysis of BTD between channels 14 and 15 (IR) from Himawari-8 retrievals produced animated imagery that captured the ash plume's movement as it traveled over the Bering Sea. Two BTD images from Himawari-8 are presented in Figure 4.5(A) and (B). Figures 4.5(A) and (B) depict an ash plume traveling east over a 48 hour period, eventually becoming entrained in upper level cyclonic turning evident in subpanel (B).

Preprocessing scripts crawl the Tokyo VAAC website for warnings every 5 minutes and thus came across the 19:28UTC warning at 19:30UTC on 21 June. The initial warning text did not include a discreet eruption height or rate and thus initialized the model using tabulated eruption source parameters. Raikoke has been assigned a Standard Mafic (M0) eruption type, corresponding to an eruption rate of 1×10^5 kg s^{-1} for a duration of 60 hours, and plume height of 7 km ASL (Mastin et al. 2009). The eruption onset was set to June 21 at 1900UTC based on the warning text.

The model initialized 8 model members, shown in Table 4.5. The lUU and sUU members were not initialized as their 21 km (7 km x 3) plume height would initialize the plume top past the top layer of the model. Importantly, two of the model members, sUM and lUM, were initialized at 10.5 km (7 km x 1.5) which is within the detected plume height of 10-13 km. The automated scripts submitted batch jobs to Air Force and Navy Department of Defense Supercomputing Resource Centers. The model was initialized at 00:00UTC on June 20, providing over 24 hours of model

spin up time for the meteorological fields to stabilize. These jobs requested 10 nodes of 36 cores each, and completed the run in 32 and 34 minutes, respectively and provided 48 hour forecasts from June 22 to June 24.

4.4 DISCUSSION

Post processing scripts automatically produce two products at the completion of the model run. The first are total ash column density plots in units of g m^{-2}. This integration requires, on average, 20-25 minutes to complete using the NCAR Command Language (NCL). Additionally, volcanic ash concentration plots at user defined flight levels are also generated in units of g m^{-3}. These unintegrated products require much less time and are available in minutes. This output is generated for each of the model members which in this case represented 8 separate sets of data.

Total column ash densities for the Raikoke eruption based on the sUM model run are presented in Figure 4.6. The sUM run was chosen since the 10.5 km plume height is close to the initial forecast height provided by the VAAC warning, and because the fine ash fraction will depict the afar ash transport whereas the lUM member will show proximal plume transport. In this case, the two only diverged in terms of concentration since the overall dynamics were stable throughout the atmospheric column.

As predicted by the Tokyo VAAC warning (Figure 4.4) the model predicted a tight packing of the plume as it traveled eastward over the North Pacific Ocean. The velocity of the plume was calculated by tracking the leading eastward model grid cell with mass and by assessing the wind speed vectors in the model output. These also agreed with the initial 40 knot assessment provided by the initial Tokyo VAAC warning and can be evidenced from the column density plots. For example, at 00:50Z on June 22, Toyko VAAC predicted the leading edge of the plume to be at 160°E, matching the output from WRF-Chem at 01:00UTC on the same date in Figure 4.6 (A). As time progresses, the plume continues to travel eastward until it becomes entrained in an upper level, cyclonic turning evident in Figure 4.5 (B).

An automated skill score algorithm compared the model output to retrievals from Himawari-8. This process involves first counting pixels in Himawari-8 data (Figure 4.5) that have BTD < 0K. The latitude and longitude of these pixels are then referenced to their corresponding WRF-Chem grid cells. If the corresponding WRF-Chem grid cell contains volcanic ash in excess

of the minimal ICAO advisory criteria, 2,000 $\mu g\ m^{-3}$ those cells are also counted. The two numbers are then divided and a percent match is generated. The time series of percent matches is presented in Figure 4.7. Overall, a 64% match was calculated over the 2 day forecast (00:00UTC June 22 to 00:00UTC June 25) with a standard deviation of 13%.

Volcanic ash concentrations at user specified flight levels were also generated. Flights over the North Pacific Ocean are usually around FL350 due to drag and fuel considerations. Figure 4.8 illustrates FL350 volcanic ash concentrations in units of $g\ m^{-3}$ using the red and yellow color scheme discussed previously. Inspection of Figure 4.8 shows similar dynamics of the plume as compared to the column density plots. The tight packing of the plume due to the fairly laminar motion of the wind fields resulted in an ash cloud at FL350 in excess of $2\ g\ m^{-3}$, resulting in the suggestion of no fly zones in red.

4.5 Conclusions

Decreasing computational costs are leading to an increase in the use of more computationally complex and robust meteorological products. Here, the WRF-Chem modeling environment (Grell et al., 2005) was automated to forecast volcanic emissions based on posted advisories from VAACs. The model was further and modified to include 10 different model initializations upon receipt of a volcanic eruption by one of the world's VAACs.

This automated, near real time WRF-Chem tool generated total column density and ash concentration plots with highlighted hazard areas and a final skill score for the June 21, 2019 eruption of Raikoke. The total duration from onset of the eruption to generation of the skill score was 1 hour and 35 minutes and includes a 38 minute delay between the eruption and the initial Toyko VAAC warning. This time is reduced to 1 hour and 10 minutes when only considering initial output of volcanic ash concentrations at user defined flight levels and decreases further to 32 minutes when not considering the delay between the eruption and VAAC warning. While the total time to generate the initial warnings, 1 hour and 10 minutes, is too long to be used operationally, it does provide robust output regarding ash concentrations, which is unique to an Eulerian, near real time VATD model. This near real time capability could augment faster particle dispersion models in volcanic ash hazard mitigation. Additionally, an automated methodology for establishing a skill score was developed by comparing brightness temperature differences to WRF-

Chem integrated colun densities. This skill score may aid end users in determining the usefulness of the output or be used as a flag for use in further automation algorithms.

The ash density products established no fly areas based on predicted ash concentrations above 2 g m^{-3} at FL350. This output could be useful to validate other flight restriction products. Importantly, time varying changes in the eruption source parameters may affect downwind concentrations, complicating the establishment of these no fly zones. As mentioned earlier, these scripts will not only begin modeling active eruptions, but will preemptively spin up based on alerts from VAACs of possible eruptions. Clear communication with any customers would be necessary to avoid confusion regarding preemptive modeling.

In addition, eight sets of model data were generated using only one model run. Despite an initialization based solely on location and eruption time, two of these members, lUM and sUM, corresponded to plume heights that were predicted by Tokyo VAAC of 10-13 km. This is a significant benefit of using this methodology where a spread of initial plume heights is used.

The output from this case highlights how the WRF-Chem model can now be used to investigate volcanic ash cloud transport in near real time, automatically. This capability to initialize a suite of simulations with multiple inputs demonstrates the usefulness of this automated WRF-Chem modeling environment that can be used in real-time during a volcanic crisis to support those decision-making organizations as well as those in the aviation community who may be impacted by the volcanic events and the dispersing cloud.

4.6 ACKNOWLEDGEMENTS

The result of this research was sponsored in part by the NOAA Cooperative Institute for Alaska Research (CIFAR) with funds from NOAA under cooperative agreement NA13OAR4320056 with the University of Alaska Fairbanks (UAF). Computational time was provided by the United States Department of Defense High Performance Computing Modernization Program, along with user support by the Navy and Air Force Department of Defense Supercomputing Resource Centers. Close collaboration with Dr. Jiang Zu at the University of Alaska Fairbanks led to improvements in the initial code through debugging and additional case studies. Dr. Christine Waigl at the University of Alaska Fairbanks aided in the development of this tool by applying it to other volcanic eruptions. Additionally, Mr. Steve Barlow

and Senior Airman Isaiah Martin at the Joint Typhoon Warning Center provided editing and feedback that aided the quality of this chapter.

FIGURES

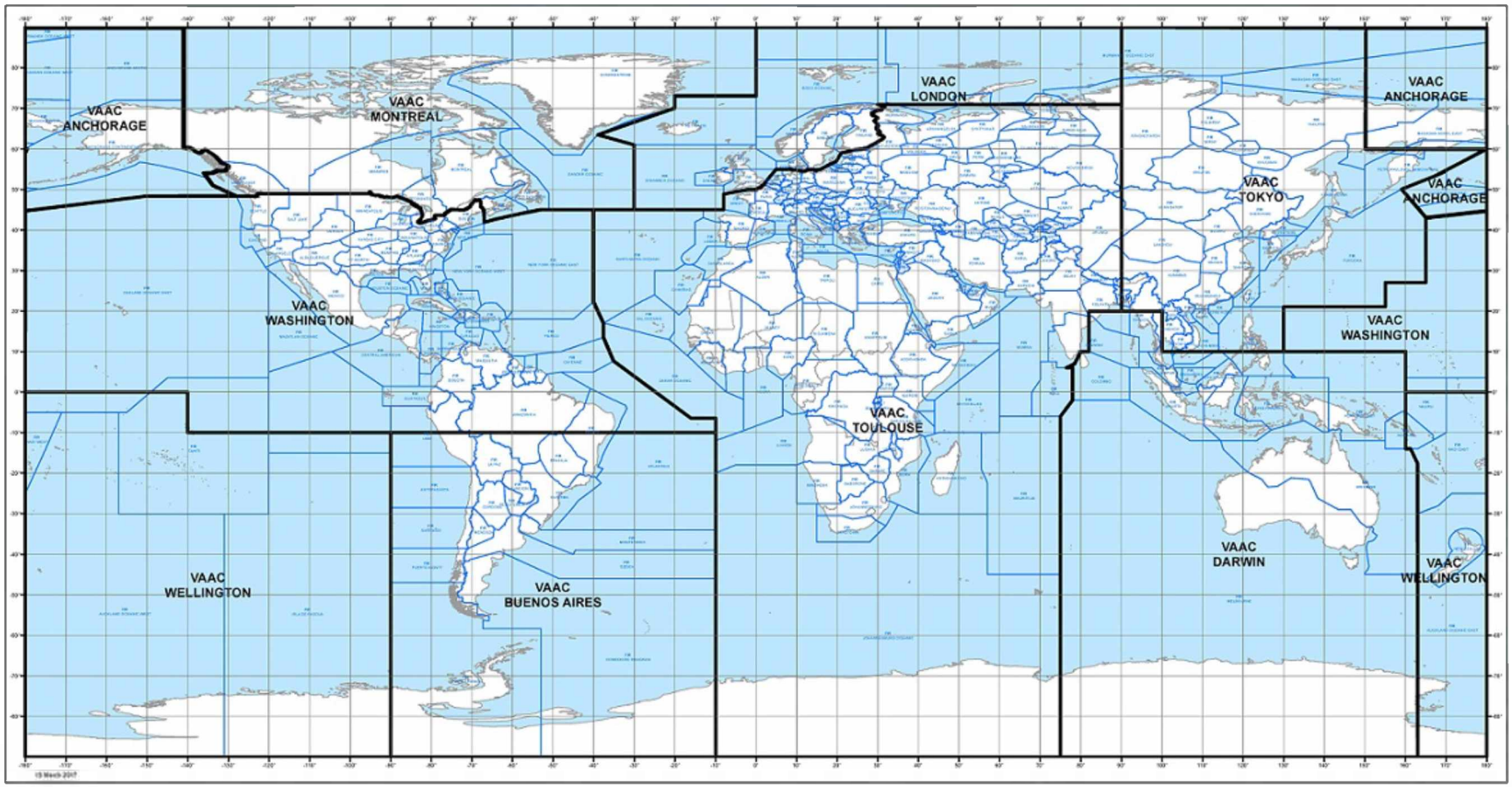

Figure 4.1 – Volcanic Ash Advisory Centers (VAACs) of the world and their respective areas of responsibility as defined by the International Civil Aviation Organization (ICAO). Image developed by ICAO and provided by the National Oceanic and Atmospheric Administration Office of Satellite and Product Operations.

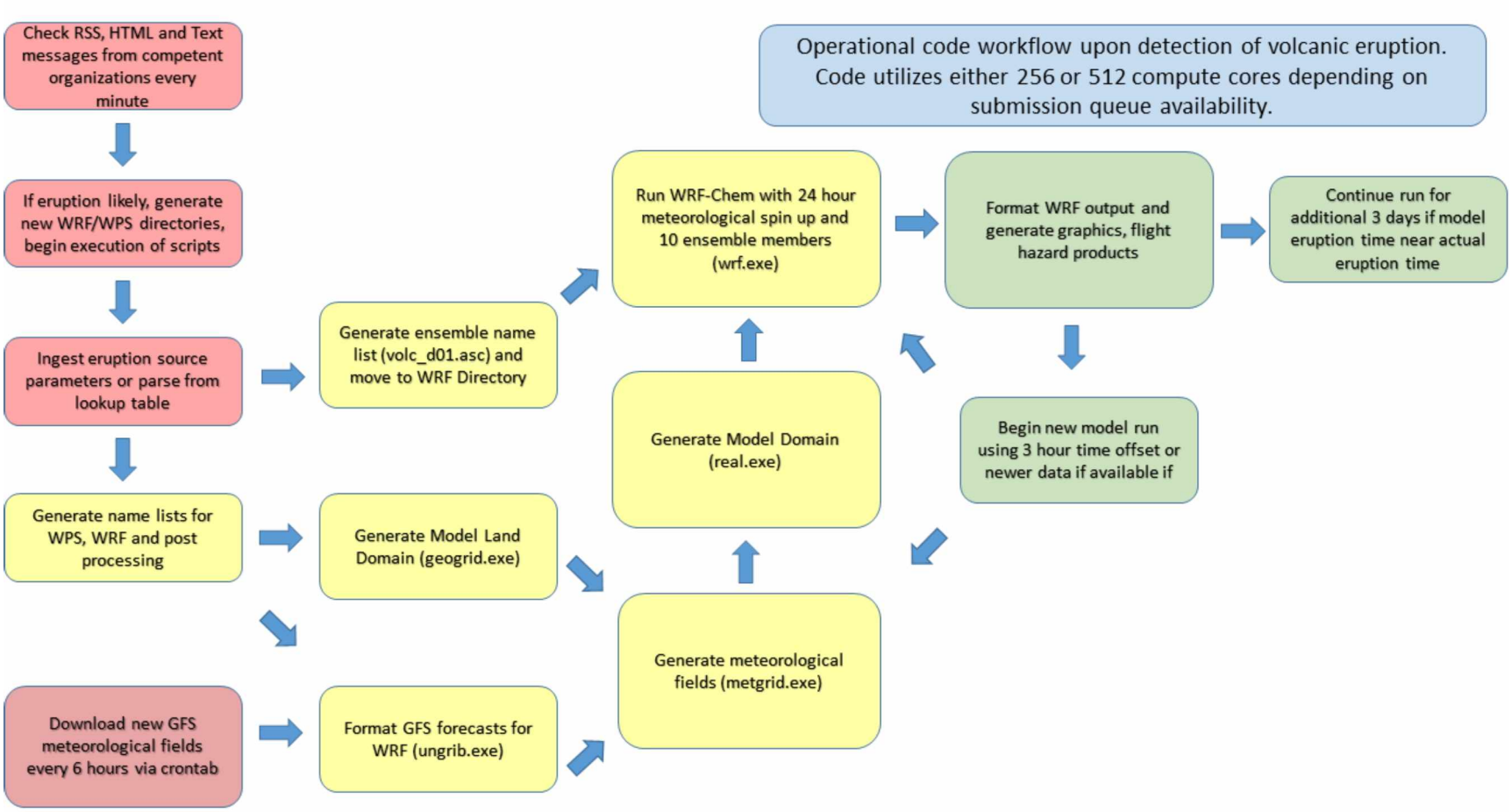

Figure 4.2 – Automated workflow illustrating the processing steps to generation of an automated WRF-Chem volcanic ash forecast. The process begins when text parsing scripts detect alert information from real-time RSS, HTML or e-mail sources. Red boxes indicate data ingest from outside sources, yellow indicate model initialization steps and green indicate model computation and product generation steps.

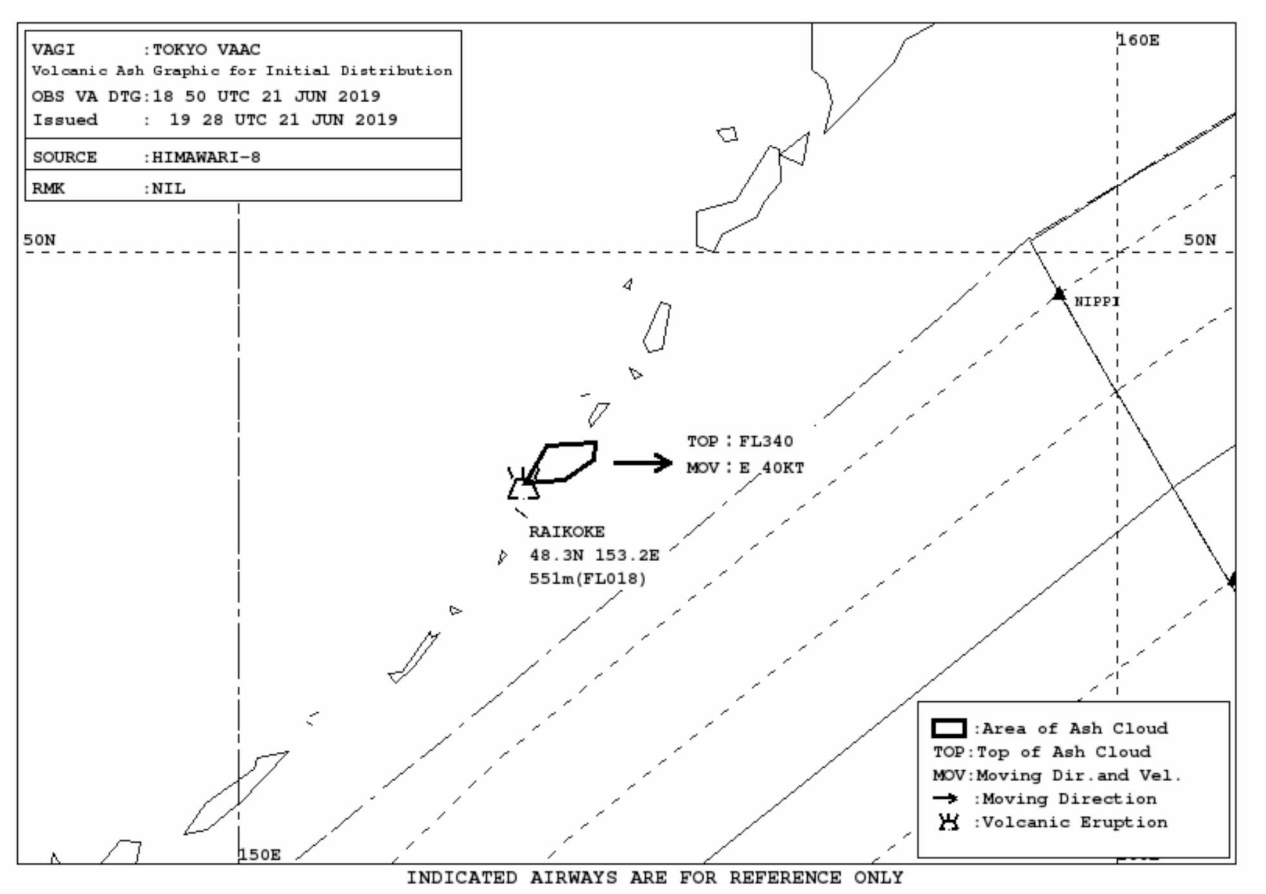

Figure 4.3 – Initial Volcanic Ash Advisory Graphic issued by Tokyo VAAC (RJTD) for the eruption of Raikoke on 22 June, 2019 at 1800 UTC. Reference MANOP FVFE01 RJTD 211928 for the full warning text, available at the Tokyo VAAC archive.

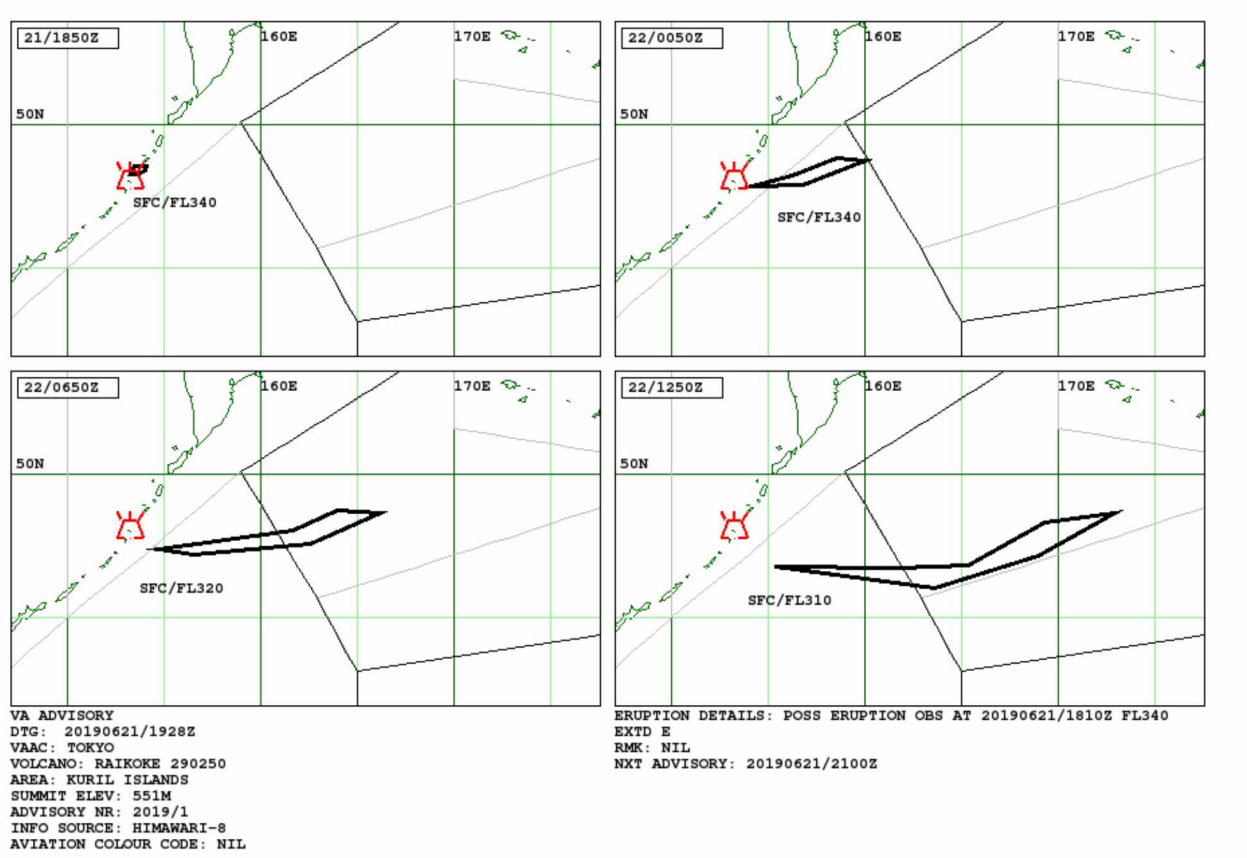

Figure 4.4 – Initial Volcanic Ash Advisory Forecast issued by Tokyo VAAC (RJTD) for the eruption of Raikoke on 22 June, 2019 at 1800 UTC. Reference MANOP FVFE01 RJTD 211928 for the full warning text, available at the Tokyo VAAC archive.

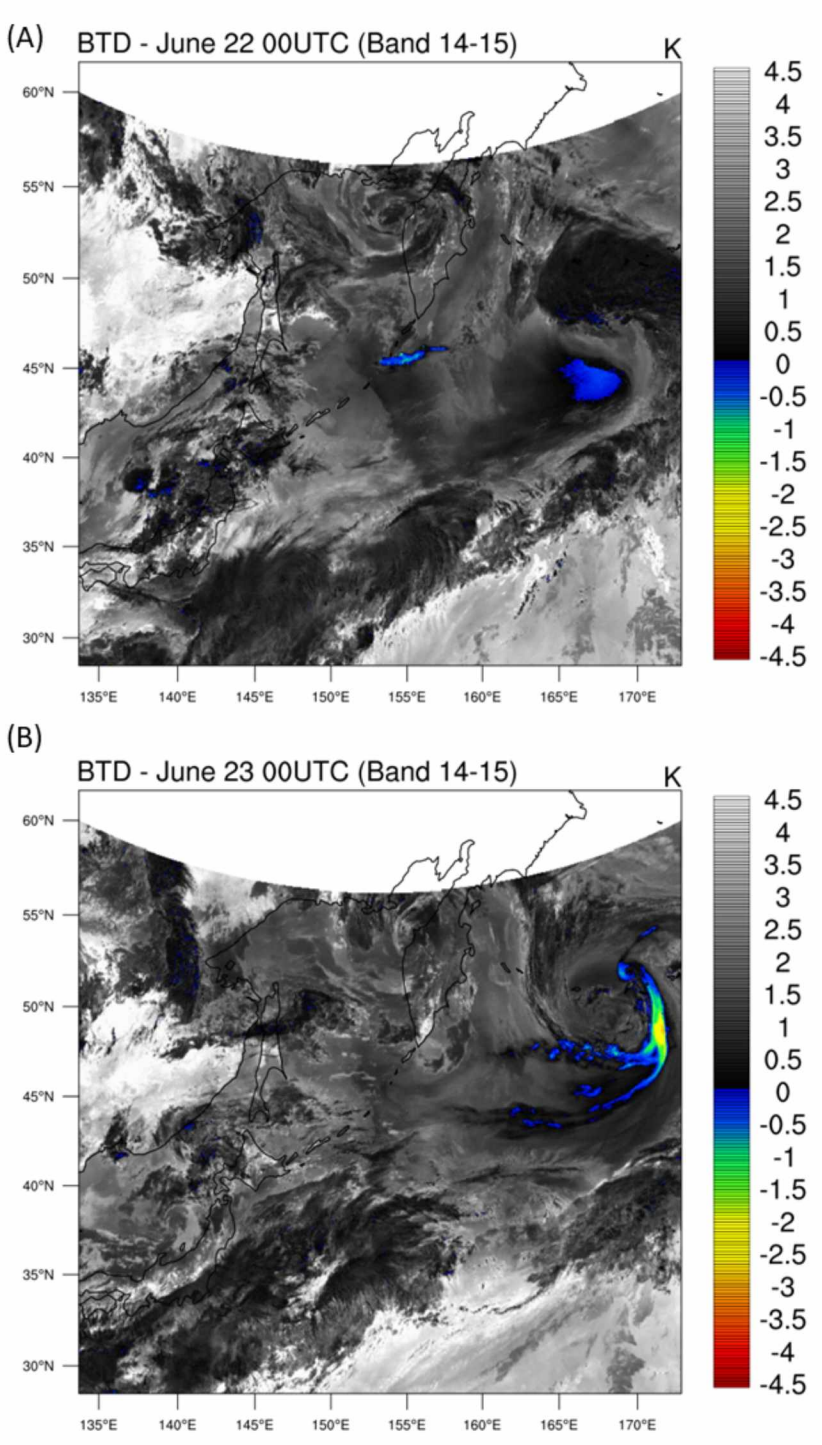

Figure 4.5 – Brightness Temperature Differences between Channels 14 and 15 from the geostationary Himawari-8 satellite IR sensor at 00:00UTC on June 22, 2019 (A) and 00:00UTC on June 23, 2019 (B).

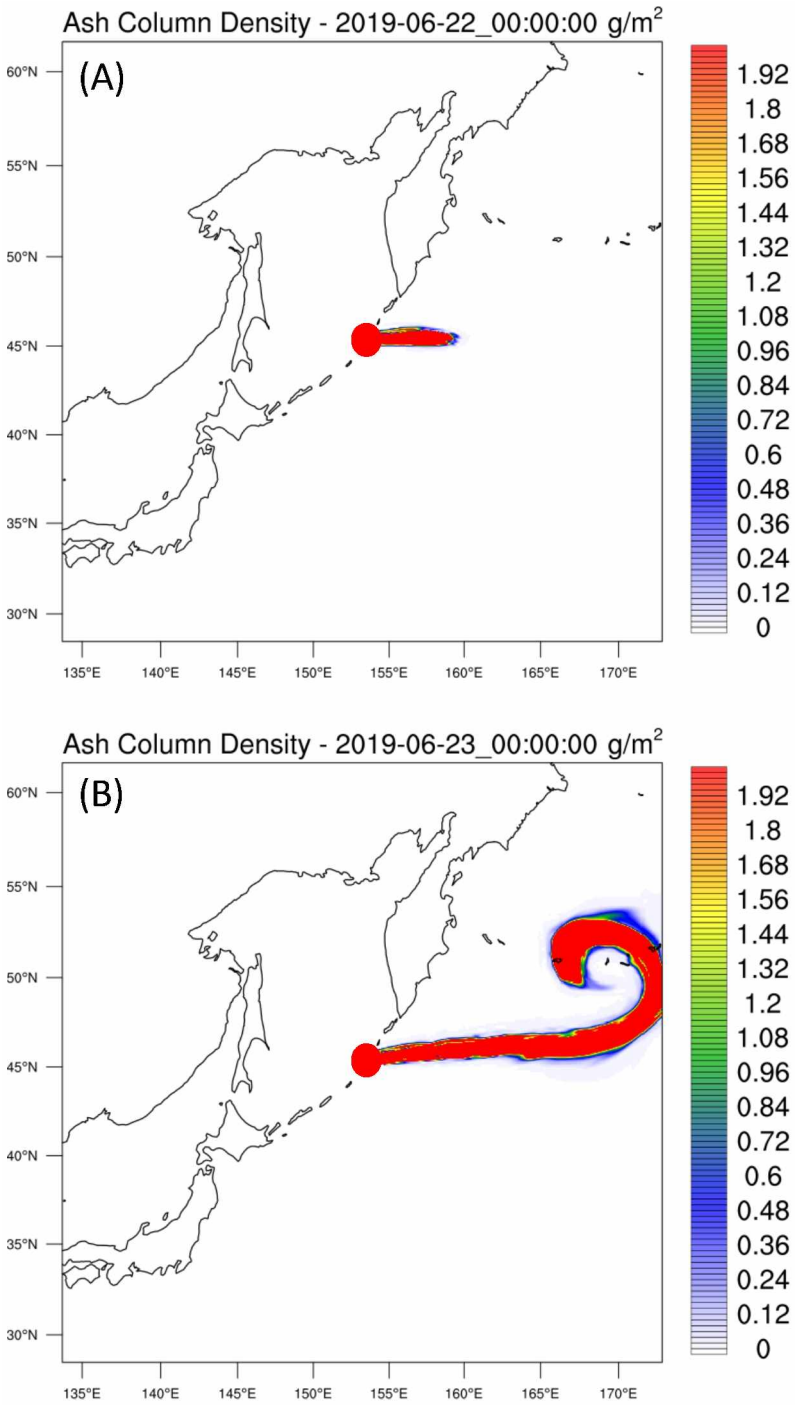

Figure 4.6 – Integrated ash column density in g m^2 for the 2019 Raikoke eruption at 00:00UTC on June 22 (A) and 00:00UTC on June 23 (B) from the sUM model member (10.5km initial eruption parameterization). Location of Raikoke marked with red circle.

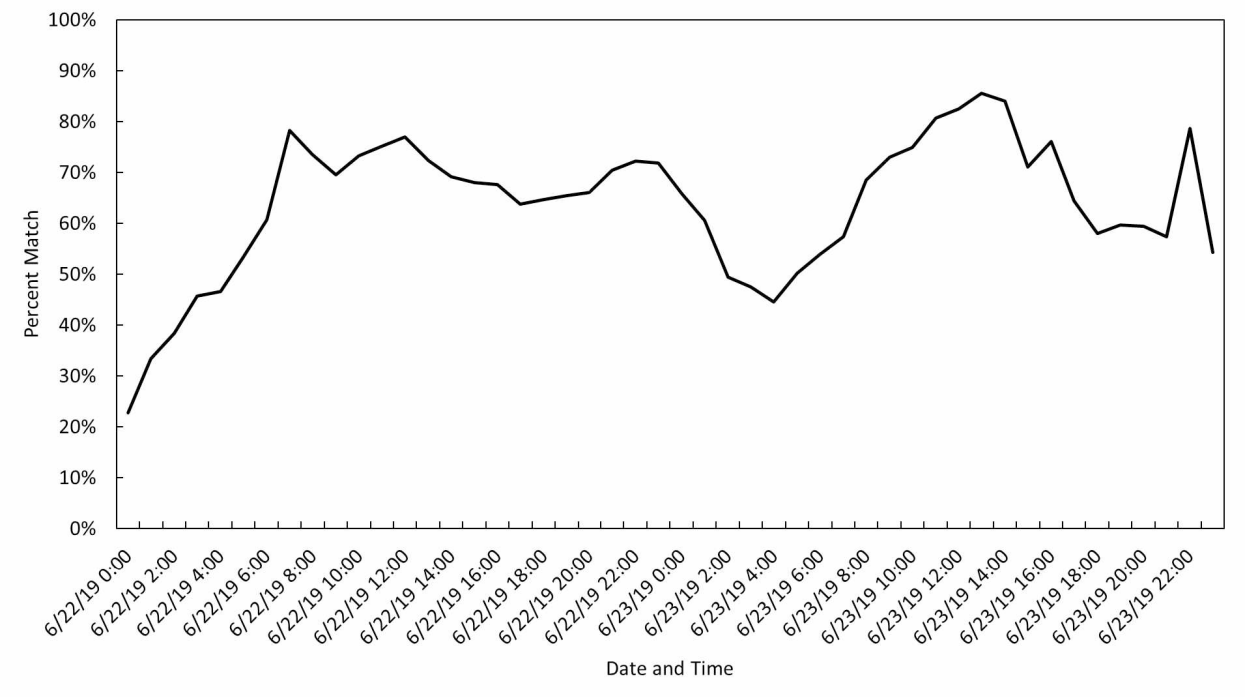

Figure 4.7 – Percentage of pixels from Himawari-8 with BTD < 0.5K that correlate to WRF-Chem model grid cells containing ash. Average match rate of 64 % and standard deviation of 13%.

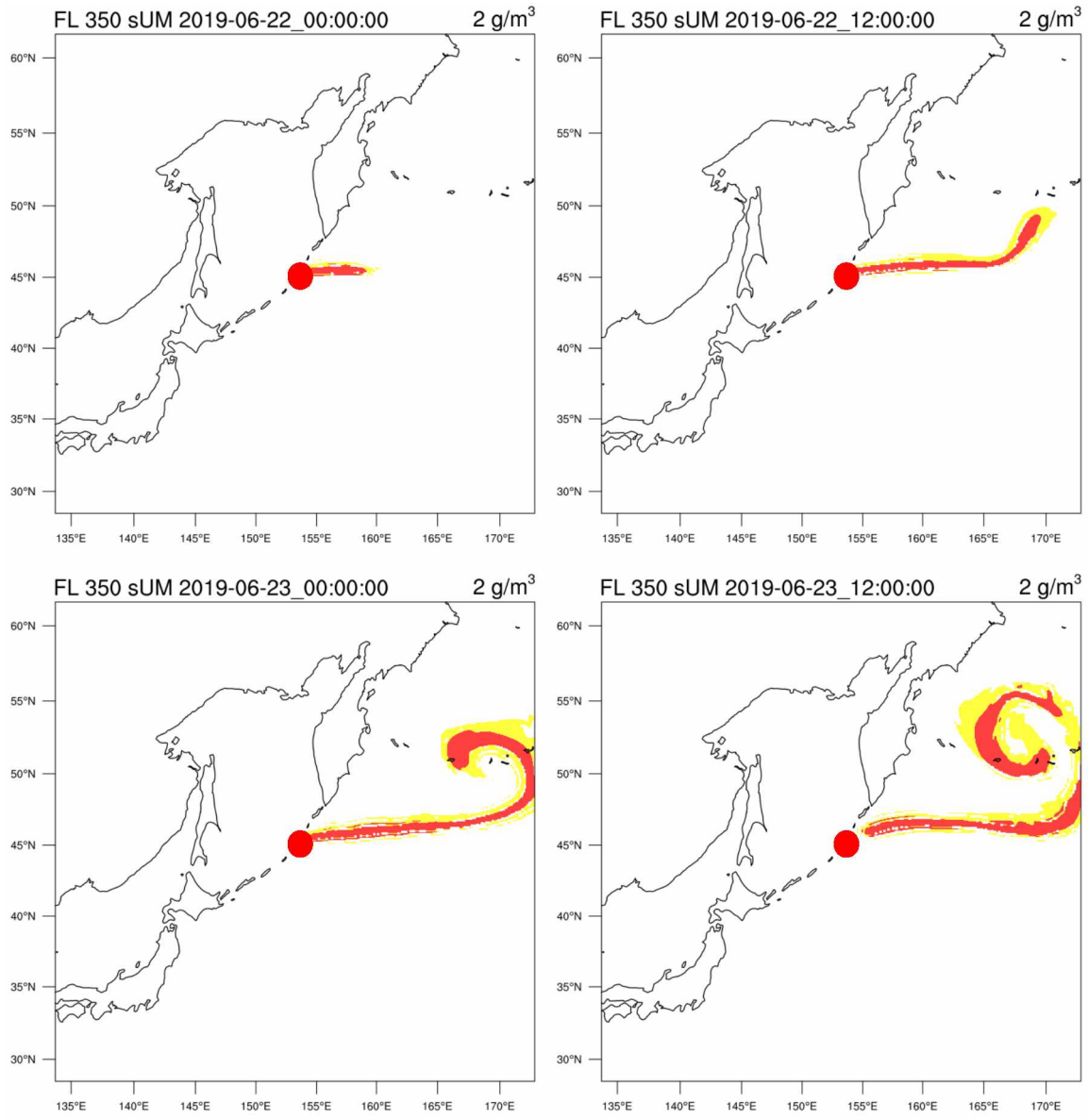

Figure 4.8 – Volcanic Ash Hazard product output for FL350 (approx. 10.7 km a.s.l.) based on sUM model members with areas enhanced flight operations in yellow and restricted, no fly zones in red. Domain is centered over Raikoke Volcano in the Kurile Islands.

TABLES

Table 4.1 – Particle size bins included in WRF-Chem and their respective particle diameters. Values are based on the Φ distribution of Krumbein (1934).

WRF bin #	Φ term	Particle size (dia.)
1	<0	1-2 mm
2	0-1	0.5-1 mm
3	1-2	0.25-0.5 mm
4	2-3	125-250 μm
5	3-4	62.5-125 μm
6	4-5	31.25-62.5 μm
7	5-6	15.625-31.25 μm
8	6-7	7.8125-15.625 μm
9	7-8	3.9065-7.8125 μm
10	>8	<3.9065 μm

Table 4.2 – Naming convention for WRF-Chem volcanic modeling members.

Model height	Particle sizes 7.8125-15.625 μm (l)	Particle sizes < 3.9065 μm (s)
Upper	lUU	sUU
Upper Mid	lUM	sUM
Middle	lM	sM
Lower Mid	lLM	sLM
Lowest	lLL	sLL

Table 4.3 – Default model domain settings for automated WRF-Chem forecasts. Model domains are always centered on the latitude and longitude of the volcano. The number of computational cores selected is based on compute node availability.

Number of Grid Cells	400 East-West x 400 North-South
Grid Cell Resolution	7.5 km East-West x 7.5 km North-South
Map Projection	Lambert Conformal Conic
Number of η levels	32, exponentially spaced
Processors Reserved	512 or 256 cores

Table 4.4 – Naming convention and plume heights for WRF-Chem volcanic modeling members for Raikoke 2019 real-time simulations.

Model plume height (a.s.l.)	**Particle sizes 7.8125-15.625 µm (l)**	**Particle sizes < 3.9065 µm (s)**
21,000 m	lUU	sUU
10.5 m	lUM	sUM
7,000 m	lM	sM
3,710 m	lLM	sLM
1,590 m	lLL	sLL

REFERENCES

Alexander, D.: Volcanic ash in the atmosphere and risks for civil aviation: A study in European crisis management, Int. J. Disaster Risk Sci., 4(1), 9–19, doi:10.1007/s13753-013-0003-0, 2013.

Anon: Kasatochi, Aleutian Islands : Natural Hazards, [online] Available from: http://earthobservatory.nasa.gov/NaturalHazards/view.php?id=9005&eocn=image&eoci=morenh (Accessed 7 October 2016), 2003.

AVO: Pavlof Eruption Description, [online] Available from: http://www.avo.alaska.edu/activity/report.php?id=336999&mode=hans&type=8 (Accessed 21 November 2016), 2016.

Bailey, J. E., Dean, K. G., Dehn, J. and Webley, P. W.: Integrated satellite observations of the 2006 eruption of Augustine Volcano: Chapter 20 in The 2006 eruption of Augustine Volcano, Alaska, USGS Numbered Series, U.S. Geological Survey. [online] Available from: http://pubs.er.usgs.gov/publication/pp176920 (Accessed 10 July 2019), 2010.

Blong, R. J.: Volcanic hazards. A sourcebook on the effects of eruptions, [online] Available from: http://www.osti.gov/energycitations/product.biblio.jsp?osti_id=7057586 (Accessed 29 October 2012), 1984.

Brenguier, F., Shapiro, N. M., Campillo, M., Ferrazzini, V., Duputel, Z., Coutant, O. and Nercessian, A.: Towards forecasting volcanic eruptions using seismic noise, Nat. Geosci., 1(2), 126–130, doi:10.1038/ngeo104, 2008.

Brown, R. J., Bonadonna, C. and Durant, A. J.: A review of volcanic ash aggregation, Phys. Chem. Earth Parts ABC, 45–46, 65–78, doi:10.1016/j.pce.2011.11.001, 2012.

Bull, K. F. and Buurman, H.: An overview of the 2009 eruption of Redoubt Volcano, Alaska, J. Volcanol. Geotherm. Res., 259, 2–15, doi:10.1016/j.jvolgeores.2012.06.024, 2013.

Carey, S. and Sparks, R. S. J.: Quantitative models of the fallout and dispersal of tephra from volcanic eruption columns, Bull. Volcanol., 48(2–3), 109–125, doi:10.1007/BF01046546, 1986.

Casadevall, T. J.: Volcanic Haazards and Aviation Safety: Lessons of the Past Decade, United States Geological Survey. [online] Available from: http://www.aerohabitat.org/airmanshiponline/marzo2003/21-Volcanic%20Hazards%20and%20Aviation%20Safety.pdf, 1992.

Casadevall, T. J., Delos Reyes, P. J. and Schneider, D. J.: The 1991 Pinatubo eruptions and their effects on aircraft operations, Fire Mud Erupt. Lahars Mt. Pinatubo Philipp., 625–636, 1996.

Chouet, B. A. and Matoza, R. S.: A multi-decadal view of seismic methods for detecting precursors of magma movement and eruption, J. Volcanol. Geotherm. Res., 252, 108–175, doi:10.1016/j.jvolgeores.2012.11.013, 2013.

De la Cruz-Reyna, S. and Tilling, R. I.: Scientific and public responses to the ongoing volcanic crisis at Popocatépetl Volcano, Mexico: Importance of an effective hazards-warning system, J. Volcanol. Geotherm. Res., 170(1), 121–134, doi:10.1016/j.jvolgeores.2007.09.002, 2008.

Dean, K., Webley, P. W., Lovick, J., Puchrik, R., Bailey, J. E., Dehn, J. and Valcic, L.: Alaska Volcano Observatory's satellite remote sensing of the Okmok and Kasatochi 2008 eruptions, AGU Fall Meet. Abstr., 1, 0265, 2008.

Dehn, J., Dean, K. G., Engle, K. and Izbekov, P.: Thermal precursors in satellite images of the 1999 eruption of Shishaldin Volcano, Bull. Volcanol., 64(8), 525–534, doi:10.1007/s00445-002-0227-0, 2002.

Draxler, R. R. and Rolph, G. D.: HYSPLIT (HYbrid single-particle Lagrangian integrated trajectory) model access via NOAA ARL READY. NOAA Air Resources Laboratory, Silver Spring, MD, Dostupno Na Httpready Arl Noaa GovHYSPLIT Php 06 06 2010, 2003.

Durant, A. J., Shaw, R. A., Rose, W. I., Mi, Y. and Ernst, G. G. J.: Ice nucleation and overseeding of ice in volcanic clouds, J. Geophys. Res. Atmospheres, 113(D9), D09206, doi:10.1029/2007JD009064, 2008.

Egan, S. D., Stuefer, M., Webley, P., Cahill, C. F. and Dehn, J.: WRF-Chem modeling of sulfur dioxide emissions from the 2008 Kasatochi Volcano, Ann. Geophys., 57(0), doi:10.4401/ag-6626, 2015.

Folch, A., Costa, A. and Macedonio, G.: FALL3D: A computational model for transport and deposition of volcanic ash, Comput. Geosci., 35(6), 1334–1342, doi:10.1016/j.cageo.2008.08.008, 2009.

Freitas, S. R., Longo, K. M., Alonso, M. F., Pirre, M., Marecal, V., Grell, G., Stockler, R., Mello, R. F., Sánchez Gácita, M.: PREP-CHEM-SRC-1.0: a preprocessor of trace gas and aerosol emission fields for regional and global atmospheric chemistry models, Geosci. Model Dev., 4(2), 419-433, doi:doi.org/10.5194/gmd-419-2011, 2011.

Graf, H.-F., Herzog, M., Oberhuber, J. M., Textor, C. and Trentmann, J.: ATHAM - ActiveTracer High Resolution Atmospheric Model Manual, Max-Planck-Institute for Meteorology., 2002.

Grell, G. A., Peckham, S. E., Schmitz, R., McKeen, S. A., Frost, G., Skamarock, W. C. and Eder, B.: Fully coupled "online" chemistry within the WRF model, Atmos. Environ., 39(37), 6957–6975, doi:10.1016/j.atmosenv.2005.04.027, 2005.

Guffanti, M. and Miller, T. P.: A volcanic activity alert-level system for aviation: review of its development and application in Alaska, Nat. Hazards, 69(3), 1519–1533, doi:10.1007/s11069-013-0761-4, 2013.

Guffanti, M. and Tupper, A.: Chapter 4 - Volcanic Ash Hazards and Aviation Risk, in Volcanic Hazards, Risks and Disasters, edited by J. F. Shroder and P. Papale, pp. 87–108, Elsevier, Boston., 2015.

Harris, A. J. L., Gurioli, L., Hughes, E. E. and Lagreulet, S.: Impact of the Eyjafjallajökull ash cloud: A newspaper perspective: Impact of the Eyjafjallajökull Ash Cloud, J. Geophys. Res. Solid Earth, 117(B9), doi:10.1029/2011JB008735, 2012.

Herrmann, R. B.: Computer Programs in Seismology: An Evolving Tool for Instruction and Research, Seismol. Res. Lett., 84(6), 1081–1088, doi:10.1785/0220110096, 2013.

Hildreth, S. A.: National Missile Defense and Alaska, Congressional Research Service, Library of Congress., 2001.

Hirtl, M., Stuefer, M., Arnold, D., Grell, G., Maurer, C., Natali, S., Scherllin-Pirscher, B. and Webley, P.: The effects of simulating volcanic aerosol radiative feedbacks with WRF-Chem during the Eyjafjallajökull eruption, April and May 2010, Atmos. Environ., 198, 194–206, doi:10.1016/j.atmosenv.2018.10.058, 2019.

International Civil Aviation Organization: Handbook on the International Airways Volcano Watch (IAVW). Operational procedures and contact list, 2004.

Krumbein, W. C.: Size frequency distributions of sediments, J. Sediment. Res., 4(2) [online] Available from: http://archives.datapages.com/data/sepm/journals/v01-32/data/004/004002/0065.htm (Accessed 24 April 2016), 1934.

Mastin, L. G., Guffanti, M., Servranckx, R., Webley, P., Barsotti, S., Dean, K., Durant, A., Ewert, J. W., Neri, A., Rose, W. I., Schneider, D., Siebert, L., Stunder, B., Swanson, G., Tupper, A., Volentik, A. and Waythomas, C. F.: A multidisciplinary effort to assign realistic source parameters to models of volcanic ash-cloud transport and dispersion during eruptions, J. Volcanol. Geotherm. Res., 186(1–2), 10–21, doi:10.1016/j.jvolgeores.2009.01.008, 2009.

Mazzocchi, M., Hansstein, F. and Ragona, M.: The 2010 volcanic ash cloud and its financial impact on the European airline industry, in CESifo Forum, vol. 11, pp. 92–100, Ifo Institute for Economic Research at the University of Munich., 2010.

Miller, T. P. and Casadevall, T. J.: Volcanic ash hazards to aviation, Encycl. Volcanoes, 915–930, 2000.

Miller, T. P., McGimsey, R. G., Richter, D. H., Riehle, J. R., Nye, C. J., Yount, M. E. and Dumoulin, J. A.: Catalog of the historically active volcanoes of Alaska, US Geol. Surv. Open-File Rep., 98(582), 104, 1998.

Oberhuber, J. M., Herzog, M., Graf, H. F., & Schwanke, K. (1998). Volcanic plume simulation on large scales. Journal of Volcanology and Geothermal Research, 87(1-4), 29-53.

Peckham, S. E., Grell, G., McKeen, S., Barth, M., Pfister, G., Wiedinmyer, C., Fast, J. D., Gustafson, W. I., Zaveri, R. A. and Easter, R. C.: WRF/Chem Version 3.9 User's Guide, US Department of Commerce, National Oceanic and Atmospheric Administration, Oceanic and Atmospheric Research Laboratories, Global Systems Division. [online] Available from: https://ruc.noaa.gov/wrf/wrf-chem/Users_guide.pdf, 2018.

Peterson, R. A. and Dean, K. G.: Forecasting exposure to volcanic ash based on ash dispersion modeling, J. Volcanol. Geotherm. Res., 170(3–4), 230–246, doi:10.1016/j.jvolgeores.2007.10.003, 2008.

Prata, A. J.: Observations of volcanic ash clouds in the 10-12 μm window using AVHRR/2 data. *Int. J. of Remote Sensing*, *10*(4-5), 751-761, 1989a

Prata, A. J.: Infrared radiative transfer calculations for volcanic ash clouds. Geophys. Res. Let., 16(11), 1293-1296, 1989b

Rose, W. I. and Durant, A. J.: Fine ash content of explosive eruptions, J. Volcanol. Geotherm. Res., 186, 32–39, doi:10.1016/j.jvolgeores.2009.01.010, 2009.

Rose, W. I. and Durant, A. J.: Fate of volcanic ash: Aggregation and fallout, Geology, 39(9), 895–896, doi:10.1130/focus092011.1, 2011.

Searcy, C., Dean, K. and Stringer, W.: PUFF: A high-resolution volcanic ash tracking model, J. Volcanol. Geotherm. Res., 80(1), 1–16, 1998.

Sennert, S. K.: Report on Raikoke (Russia, Kurile Islands) - 19 June-25 June, Smithsonian Institute and US Geological Survey., 2019.

Sparks, R. J. S., Burski, M. I., Carey, S. N., Gilbert, J. S., Glaze, L. S., Siquerdsson, H. and Woods, A. W.: Volcanic Plumes, John Wiley and Sons, Sussex, England., 1997.

Sparks, R. S. J.: Forecasting volcanic eruptions, Earth Planet. Sci. Lett., 210(1), 1–15, doi:10.1016/S0012-821X(03)00124-9, 2003.

Sparks, R. S. J., Biggs, J. and Neuberg, J. W.: Monitoring Volcanoes, Science, 335(6074), 1310–1311, doi:10.1126/science.1219485, 2012.

Stohl, A., Sodemann, H., Eckhardt, S., Frank, A., Seibert, P. and Wotawa, G.: The Lagrangian particle dispersion model FLEXPART version 8.2, FLEXPART User Guide [online] Available from: http://folk.nilu.no/~flexpart/flexpart/flexpart82.pdf (Accessed 7 October 2016), 2011.

Stuefer, M., Freitas, S. R., Grell, G., Webley, P., Peckham, S., McKeen, S. A. and Egan, S. D.: Inclusion of ash and SO 2 emissions from volcanic eruptions in WRF-Chem: development and some applications, Geosci. Model Dev., 6(2), 457–468, doi:doi.org/10.5194/gmd-6-457-2013, 2013.

Tupper, A., Textor, C., Herzog, M., Graf, H.-F. and Richards, M. S.: Tall clouds from small eruptions: the sensitivity of eruption height and fine ash content to tropospheric instability, Nat. Hazards, 51(2), 375–401, doi:10.1007/s11069-009-9433-9, 2009.

Webley, P.: Role of Uncertainty in Decision Support for Volcanic Ash Cloud Modeling, Nat. Hazard Uncertain. Assess., 43–56, 2017.

Webley, P. and Mastin, L.: Improved prediction and tracking of volcanic ash clouds, J. Volcanol. Geotherm. Res., 186(1–2), 1–9, doi:10.1016/j.jvolgeores.2008.10.022, 2009.

Webley, P., Patra, A., Bursik, M., Pitman, E. B., Dehn, J., Singh, T., Singla, P., Jones, M. D., Madankan, R. and Stefanescu, E. R.: Building an Uncertainty Modeling Framework for Real-Time VATD, Nat. Hazard Uncertain. Assess., 57–87, 2017.

Webley, P. W., Stunder, B. J. B. and Dean, K. G.: Preliminary sensitivity study of eruption source parameters for operational volcanic ash cloud transport and dispersion models — A case study of the August 1992 eruption of the Crater Peak vent, Mount Spurr, Alaska, J. Volcanol. Geotherm. Res., 186(1–2), 108–119, doi:10.1016/j.jvolgeores.2009.02.012, 2009.

Webley, P. W., Steensen, T., Stuefer, M., Grell, G., Freitas, S. and Pavolonis, M.: Analyzing the Eyjafjallajökull 2010 eruption using satellite remote sensing, lidar and WRF-Chem dispersion and tracking model, J. Geophys. Res., 117, D00U26, 2012.

Webley, P. W., Lopez, T. M., Ekstrand, A. L., Dean, K. G., Rinkleff, P., Dehn, J., Cahill, C. F., Wessels, R. L., Bailey, J. E., Izbekov, P. and Worden, A.: Remote observations of eruptive clouds and surface thermal activity during the 2009 eruption of Redoubt volcano, J. Volcanol. Geotherm. Res., 259, 185–200, doi:10.1016/j.jvolgeores.2012.06.023, 2013.

Woods, A. W.: Moist convection and the injection of volcanic ash into the atmosphere, J. Geophys. Res. Solid Earth, 98(B10), 17627–17636, doi:10.1029/93JB00718, 1993.

CHAPTER 5 – DISSERTATION CONCLUSIONS

Volcanic ash modeling has been established as a priority for aircraft hazard mitigation. Various communities, from private pilots to commercial entities to military organizations, require observations on the transport and location of volcanic ash in order to operate safely. This dissertation research adapted the Weather Research Forecasting with Chemistry (WRF-Chem) model into an automated, near real-time Volcanic Ash Transport and Dispersion (VATD) model. Each chapter approached this goal through a differently methodology. Chapter 1 provided a brief background on volcanic ash and sulfur dioxide (SO_2) modeling. Chapter 2 discussed previous WRF-Chem modeling of volcanic ash and SO_2 and presented research on the use of the model to the 2009 eruption of Kasatochi volcano in Alaska. Here, WRF-Chem was observed to produce SO_2 column densities that agreed well with observations from remote sensing. Chapter 3 presented the research on the application of WRF-Chem to volcanic ash modeling. In addition, Chapter 3's research incorporated a new volcanic ash aggregation mechanism into the WRF-Chem code, adding an additional sink to atmospheric volcanic ash through this process. WRF-Chem simulations with and without this new aggregation code were studied and evaluated through intra-model analysis and comparisons to in situ measurements, remote sensing and field observations from the 2010 eruption of Eyjafjallajökull volcano in Iceland. WRF-Chem produced volcanic ash fields that somewhat agreed spatially and temporally with other methods. In addition, the newly added aggregation code produced mass concentrations closer to observed values than the unmodified code did. In Chapter 4, research focused on modifying the WRF-Chem code to transform it into a VATD model capable of generating near real-time volcanic ash hazard maps. The new automated, near real-time capability was applied to the 2019 eruption of Raikoke in Kurile Islands. An automated skill score algorithm was developed that showed a 64% match between remote sensing and model derived ash densities spatially and temporally. The following paragraphs summarize the key findings taken from the entirety of these chapters, and discusses future directions of this work.

5.1 Ability of WRF-Chem to Model Volcanic Ash and Sulfur Dioxide

Each of the dissertation chapters assessed WRF-Chem's ability to model volcanic ash and sulfur dioxide accurately. In the case of SO_2, WRF-Chem modeled the SO_2 cloud generated from the eruption of Kasatochi volcano in 2009. As discussed, SO_2 is often used as a proxy for volcanic ash when brightness temperature differences in the infrared spectrum are difficult to generate due to a lack of thermal contrast (Carn et al., 2008, 2009; Thomas and Prata, 2011). In these cases, hyperspectral instruments built for ozone observations may be used as SO_2 is often collocated with ash. In these cases, knowing the concentration of SO_2 may be important for threshold detection as the concentration of SO_2 decreases with time due to dilution and conversion to sulfate. WRF-Chem in the Kasatochi case modeled SO_2 plume transport as well as the conversion of SO_2 to sulfate. This approach is able to provide operational forecasters with observations on the location and concentration of volcanic SO_2 clouds, which in turn may help them constrain areas of remote sensing to model derived locations, streamlining the dissemination of aircraft hazard mitigation recommendations (Carn et al., 2009). Moreover, concentration measurements, which are accurately modeled by capturing SO_2 conversion, provides useful data regarding detection limits. Importantly, Chapter 2 also concludes that the WRF-Chem model is particularly sensitive to the initial plume height used. When plume height was varied, different outcomes were noticed. As the plume height deviated from the actual plume height, agreement with Ozone Monitoring Instrument column retrievals also diverged.

WRF-Chem modeled volcanic ash plumes and clouds from Eyjafjallajökull and Raikoke volcanos in this dissertation. In the case of Eyjafjallajökull (Chapter 3), WRF-Chem generated volcanic ash cloud locations that agreed with previous studies of the ash cloud transport (Arason et al., 2011; Bolić and Sivčev, 2011; Francis et al., 2012; Gudmundsson et al., 2012; Prata and Prata, 2012; Thomas and Prata, 2011; Webley et al., 2012). This result was to be expected as WRF-Chem had been applied to this case previously and generated similar results (Hirtl et al., 2019; Stuefer et al., 2013; Webley et al., 2012). WRF-Chem had not been applied to the Raikoke case previously, but also produced ash cloud locations that agreed with remote sensing observations.

The interesting result of the Eyjafjallajökull case study was WRF-Chem's ability to produce atmospheric ash concentrations that were similar to in situ ash cloud concentrations measured in Schumann et al., (2011). The ash concentrations agreed over 85% of the time within

an order of magnitude in concentration, showing not only good temporal and spatial agreement, but good agreement in concentration as well. This suggests that WRF-Chem, as run in Chapter 4 with aggregation enabled, can produce ash concentration area maps that may be used not only to establish guidelines for aircraft safety, but for research purposes as well, such as the validation of remote sensing methods. WRF-Chem also produced tephra fallout that was on the same order of magnitude as field measurements that were taken in the United Kingdom (Stevenson et al., 2012). Ash fall can be a hazard to facilities and people on the ground (Casadevall, 1992; Miller and Casadevall, 2000). This ash fall prediction capability can benefit customers with sensitive ground-based facilities, such as airlines and the military.

5.2 Factors of Aggregation in Volcanic Ash Modeling

Volcanic ash aggregation is known to occur in many, if not all, volcanic plumes, mostly due to a wet type aggregation where liquid water enhances the sticking efficiency of ash particles (Brown et al., 2012; Gilbert and Lane, 1994; James et al., 2002, 2003; Van Eaton et al., 2012, 2015). The aggregation process enhances the sizes of volcanic ash particles and in return increases their fall velocities, decreasing overall atmospheric lifetime (Brown et al., 2012; Rose and Durant, 2011). Traditionally, Volcanic Ash Transport and Dispersion (VATD) models do not account for ash aggregation processes, with the exception of the Fall3D model (Folch et al., 2009, 2010). This means that for most VATD models, the sole sink of volcanic ash in the atmosphere is through settling routines, which may overestimate the lifetime of ash.

In Chapter 3, the WRF-Chem code was modified to include volcanic ash aggregation as an additional mass sink by adding a simplified version of the Smoluchowski Coagulation Equation (Costa et al., 2010; Folch et al., 2010; Smoluchowski, 1917). A few important conclusions arose from this study.

The Smoluchowski equation is not a purely atmospheric coagulation equation. It describes the physics of colliding particles and their rate of aggregation in any medium. To study how it behaved in a numerical weather prediction environment, each collision mechanism (referred to as collision kernels in Chapter 3) was studied independently. Parameterizations included collisions due to Brownian (random) motion, shear and sedimentation. Using this methodology, Chapter 3 concludes that only differential sedimentation needs to be accounted for in aggregation

mechanisms applied to volcanic ash in numerical weather prediction models. Particle interactions due to differential sedimentation are many orders of magnitude higher than those due to Brownian or shear interactions. It may be sufficient to only enable the calculation of a differential sedimentation collision kernel, instead of all three. This approach could decrease computational time and still provide useful model output.

Chapter 3 also concluded that there is a link between ash particle size and mass on the aggregation rate when calculated with the simplified Smoluchowski equation. In an initial assessment of the model, the eruption particle size distribution was kept constant, populating each particle size bin with the same amount of mass. Here, little difference in the resulting particle size distribution (PSD) was noticed after the eruption ended. When the model was applied to the case of Eyjafjallajökull volcano, a bimodal S2 PSD was used, varying the mass that was input into each particle size bin by a different percentage. As the model progressed, the resulting PSD changed to a greater extent that it did in the initial test case (Compare Figures 3.5 and 3.12). Comparing these two test results suggests that the simplified form of the Smoluchowski Equation is more sensitive to mass concentration than particle size when considering changes in the resulting PSD.

The code modifications in Chapter 3 were coupled to water vapor concentrations. Water vapor was added to the test model and the sensitivity of the new code to this coupling was measured (see Figure 3.2). While there was enhanced aggregation (measured through a loss of domain mass) due to enabling coupled water vapor emissions, it was a small factor (less than 1% change in mass). The effect of water vapor on the aggregation rate decreased with time as well due to the dilution of emissions in the surrounding environment.

The aggregation case study also confirms that the majority of aggregation (in the case of these model case studies over 50% of aggregation) occurs near the volcano in the eruptive plume where masses are highest. This result agrees with many observational studies that indicate a majority of volcanic ash aggregation and fallout occur in the proximal plume and cloud (Brown et al., 2012; Rose and Durant, 2011; Van Eaton et al., 2015). This initial decrease in mass is an important process to capture since underestimating it produces ash concentrations that are much larger than what are actually feasible. This overestimation of ash concentration is then a hinderance to ash forecasting and aircraft hazard mitigation.

5.3 Feasibility of WRF-Chem as a VATD Model

Chapter 4 transformed the WRF-Chem model into an automated, near real-time VATD model. Ten model members were added to the code covering two different particle sizes, and therefore two different settling velocities, and 5 different eruptive plume heights. The code was compiled on a Department of Defense computer cluster and nested in a set of Python and bash scripts that automated simulations of volcanic ash plumes from either possible or detected volcanic eruptions. These scripts digest e-mail, text and HTML data from a variety of sources to detect these possible or actual eruptions.

On June 21, 2019, the model initialized a plume originating at Raikoke volcano in the Kurile Islands. Despite initializing the plume with only tabulated plume data, the automated code included one model run member that had a plume height in range of observed values. This member produced volcanic ash advisory pictures with areas of "enhanced flight measures" marked in yellow and no fly zones marked in red, as is customary with military color code usage.

The important conclusion from this study is that despite a lack of initial "reliable" data, this multi-height method produced one member that generated ash locations tracking alongside remote sensing data. This model member produced an actionable product that could be chosen from others once a plume height had been established through remote sensing. This result indicates that WRF-Chem can be used in an operational setting as an augmentation tool for hazard mitigation and may do so with reduced uncertainty and computational requirements by running 10 members simultaneously.

5.4 Future Directions of WRF-Chem in Atmospheric Emissions Modeling

The modified, automated, near real-time WRF-Chem code developed in Chapter 4 is already being assessed by the United States Navy for use in aircraft hazard mitigation. The goal of this dissertation is to aid in this process by applying it to multiple eruptive cases.

This work also already in the process of moving past volcanic ash hazard mitigation and on towards nuclear fallout and chemical weapons dispersion modeling and mitigation. The greatest benefit of WRF-Chem is the ability to capture changes in atmospheric chemical species as their concentrations change in time. Furthermore, the model is highly customizable due to its modular

format and consistent use of C and Fortran with higher level Message Passing Interface directives above each chemistry and physics package.

Radionuclide modeling is currently conducted with Lagrangian models, some of which track changes in nuclides, i.e. conversion through alpha and beta decay and spontaneous fission, as they transport. The most common example is the UK Met Office Next Generation Atmospheric Dispersion Model Generation III (NAME III) (Jones et al., 2007). WRF-Chem is being adapted for use in this area as well. In addition to modeling the concentration and conversion of radionuclides from nuclear accidents or terrorist use of nuclear material, WRF-Chem will be modified to capture radionuclide activities and account for their total neutron, gamma, beta and alpha fluxes in any given area. This capability is of particular interest to the United States Navy who operates nuclear reactors ashore and afloat, and who participated in the hazard mitigation of the Fukushima nuclear accident in 2011 (Stone, 2011).

Syria's use of chemical weapons against military and civilian populations in 2013 renewed interest and study in the area of chemical weapons hazard mitigation (Pita and Domingo, 2014). While WRF-Chem can already calculate changes in chemical concentration due to dilution, it is also feasible to add chemistry routines to WRF-Chem that could capture the conversion of chemical weapons via oxidation, photolysis and wet deposition. This effort will require additional analysis of the planetary boundary layer physics used by WRF-Chem as these emissions are often low to the ground. Reaction libraries in the same form as those of the Regional Acid Deposition Model II used in Chapter 2 (Stockwell et al., 1990) may need to be developed for chemicals of interest, as in some cases they may not currently be available.

5.5 Final Conclusions

This dissertation assessed and modified the WRF-Chem model's use for volcanic ash and SO_2 dispersion modeling. The work as a whole concludes that WRF-Chem, especially when enabled with a modeled plume height and particle size methodology, can predict the location of volcanic ash and SO_2 clouds temporally and spatially, even when there is uncertainty in the initial conditions. In addition, this work concludes that VATD models should include some form of volcanic ash aggregation mechanism. This mechanism should at least account for the interaction of ash particles due to differential settling velocities. WRF-Chem will continue to be used for

research, and with the help of this work, will find continued acceptance as a VATD model for use in aircraft hazard mitigation, and eventually radionuclide and chemical weapons mitigation.

REFERENCES

Arason, P., Petersen, G. N. and Bjornsson, H.: Observations of the altitude of the volcanic plume during the eruption of Eyjafjallajökull, April–May 2010, Earth Syst. Sci. Data, 3(1), 9–17, doi:10.5194/essd-3-9-2011, 2011.

Bolić, T. and Sivčev, Ž.: Eruption of Eyjafjallajökull in Iceland, Transp. Res. Rec. J. Transp. Res. Board, 2214, 136–143, doi:10.3141/2214-17, 2011.

Brown, R. J., Bonadonna, C. and Durant, A. J.: A review of volcanic ash aggregation, Phys. Chem. Earth Parts ABC, 45–46, 65–78, doi:10.1016/j.pce.2011.11.001, 2012.

Carn, S. A., Krotkov, N. A., Fioletov, V., Yang, K., Krueger, A. J. and Tarasick, D.: Emission, transport and validation of sulfur dioxide in the 2008 Okmok and Kasatochi eruption clouds, in AGU Fall Meeting Abstracts, vol. 1, p. 07. [online] Available from: http://adsabs.harvard.edu/abs/2008AGUFM.A51J..07C (Accessed 29 October 2012), 2008.

Carn, S. A., Krueger, A. J., Krotkov, N. A., Yang, K. and Evans, K.: Tracking volcanic sulfur dioxide clouds for aviation hazard mitigation, Nat. Hazards, 51(2), 325–343, 2009.

Casadevall, T. J.: Volcanic Haazards and Aviation Safety: Lessons of the Past Decade, United States Geological Survey. [online] Available from: http://www.aerohabitat.org/airmanshiponline/marzo2003/21-Volcanic%20Hazards%20and%20Aviation%20Safety.pdf, 1992.

Costa, A., Folch, A. and Macedonio, G.: A model for wet aggregation of ash particles in volcanic plumes and clouds: 1. Theoretical formulation, J. Geophys. Res. Solid Earth, 115(B9), B09201, doi:10.1029/2009JB007175, 2010.

Folch, A., Costa, A. and Macedonio, G.: FALL3D: A computational model for transport and deposition of volcanic ash, Comput. Geosci., 35(6), 1334–1342, doi:10.1016/j.cageo.2008.08.008, 2009.

Folch, A., Costa, A., Durant, A. and Macedonio, G.: A model for wet aggregation of ash particles in volcanic plumes and clouds: 2. Model application, J. Geophys. Res. Solid Earth, 115(B9), B09202, doi:10.1029/2009JB007176, 2010.

Francis, P. N., Cooke, M. C. and Saunders, R. W.: Retrieval of physical properties of volcanic ash using Meteosat: A case study from the 2010 Eyjafjallajökull eruption, J. Geophys. Res. Atmospheres, 117(D20), doi:10.1029/2011JD016788, 2012.

Gilbert, J. S. and Lane, S. J.: The origin of accretionary lapilli, Bull. Volcanol., 56(5), 398–411, doi:10.1007/BF00326465, 1994.

Gudmundsson, M. T., Thordarson, T., Höskuldsson, Á., Larsen, G., Björnsson, H., Prata, F. J., Oddsson, B., Magnússon, E., Högnadóttir, T., Petersen, G. N., Hayward, C. L., Stevenson, J. A. and Jónsdóttir, I.: Ash generation and distribution from the April-May 2010 eruption of Eyjafjallajökull, Iceland, Sci. Rep., 2, 572, doi:10.1038/srep00572, 2012.

Hirtl, M., Stuefer, M., Arnold, D., Grell, G., Maurer, C., Natali, S., Scherllin-Pirscher, B. and Webley, P.: The effects of simulating volcanic aerosol radiative feedbacks with WRF-Chem during the Eyjafjallajökull eruption, April and May 2010, Atmos. Environ., 198, 194–206, doi:10.1016/j.atmosenv.2018.10.058, 2019.

James, M. R., Gilbert, J. S. and Lane, S. J.: Experimental investigation of volcanic particle aggregation in the absence of a liquid phase, J. Geophys. Res. Solid Earth, 107(B9), 2191, doi:10.1029/2001JB000950, 2002.

James, M. R., Lane, S. J. and Gilbert, J. S.: Density, construction, and drag coefficient of electrostatic volcanic ash aggregates, J. Geophys. Res. Solid Earth 1978–2012, 108(B9), doi:10.1029/2002JB002011, 2003.

Jones, A., Thomson, D., Hort, M. and Devenish, B.: The U.K. Met Office's Next-Generation Atmospheric Dispersion Model, NAME III, in Air Pollution Modeling and Its Application XVII, edited by C. Borrego and A.-L. Norman, pp. 580–589, Springer US., 2007.

Miller, T. P. and Casadevall, T. J.: Volcanic ash hazards to aviation, Encycl. Volcanoes, 915–930, 2000.

Pita, R. and Domingo, J.: The Use of Chemical Weapons in the Syrian Conflict, Toxics, 2(3), 391–402, doi:10.3390/toxics2030391, 2014.

Prata, A. J. and Prata, A. T.: Eyjafjallajökull volcanic ash concentrations determined using Spin Enhanced Visible and Infrared Imager measurements, J. Geophys. Res. Atmospheres 1984–2012, 117(D20), doi:10.1029/2011JD016800, 2012.

Rose, W. I. and Durant, A. J.: Fate of volcanic ash: Aggregation and fallout, Geology, 39(9), 895–896, doi:10.1130/focus092011.1, 2011.

Schumann, U., Weinzierl, B., Reitebuch, O., Schlager, H., Minikin, A., Forster, C., Baumann, R., Sailer, T., Graf, K., Mannstein, H., Voigt, C., Rahm, S., Simmet, R., Scheibe, M., Lichtenstern, M., Stock, P., Ruba, H., Schauble, D., Tafferner, A., Rautenhaus, M., Gerz, T., Ziereis, H., Krautstrunk, M., Mallaun, C., Gayet, J. F., Lieke, K., Kandler, K., Ebert, M., Weinbruch, S., Stohl, A., Gasteiger, J., Gross, S., Freudenthaler, V., Wiegner, M., Ansmann, A., Tesche, M., Ólafsson, H. and Sturm, K.: Airborne observations of the Eyjafjalla volcano ash cloud over Europe during air space closure in April and May 2010, Atmos Chem Phys, 11(5), 2245–2279, 2011.

Smoluchowski, M.: Investigation of a Mathematical Theory on the Coagulation of Colloidal Suspensions, Z Phys. ChemGer, 92, 155, 1917.

Stevenson, J. A., Loughlin, S., Rae, C., Thordarson, T., Milodowski, A. E., Gilbert, J. S., Harangi, S., Lukács, R., Højgaard, B., Árting, U., Pyne-O'Donnell, S., MacLeod, A., Whitney, B. and Cassidy, M.: Distal deposition of tephra from the Eyjafjallajökull 2010 summit eruption, J. Geophys. Res. Solid Earth, 117(B9), doi:10.1029/2011JB008904, 2012.

Stockwell, W. R., Middleton, P., Chang, J. S. and Tang, X.: The second generation regional acid deposition model chemical mechanism for regional air quality modeling, J. Geophys. Res., 95(D10), 16343–16,367, doi:10.1029/JD095iD10p16343, 1990.

Stone, R.: Fukushima Cleanup Will Be Drawn Out and Costly, Science, 331(6024), 1507–1507, doi:10.1126/science.331.6024.1507, 2011.

Stuefer, M., Freitas, S. R., Grell, G., Webley, P., Peckham, S., McKeen, S. A. and Egan, S. D.: Inclusion of ash and SO 2 emissions from volcanic eruptions in WRF-Chem: development and some applications, Geosci. Model Dev., 6(2), 457–468, doi:doi.org/10.5194/gmd-6-457-2013, 2013.

Thomas, H. E. and Prata, A. J.: Sulphur dioxide as a volcanic ash proxy during the April–May 2010 eruption of Eyjafjallajökull volcano, Iceland, Atmos Chem Phys, 11(14), 6871–6880, 2011.

Van Eaton, A. R., Muirhead, J. D., Wilson, C. J. N. and Cimarelli, C.: Growth of volcanic ash aggregates in the presence of liquid water and ice: an experimental approach, Bull. Volcanol., 74(9), 1963–1984, doi:10.1007/s00445-012-0634-9, 2012.

Van Eaton, A. R., Mastin, L. G., Herzog, M., Schwaiger, H. F., Schneider, D. J., Wallace, K. L. and Clarke, A. B.: Hail formation triggers rapid ash aggregation in volcanic plumes, Nat. Commun., 6, doi:10.1038/ncomms8860, 2015.

Webley, P. W., Steensen, T., Stuefer, M., Grell, G., Freitas, S. and Pavolonis, M.: Analyzing the Eyjafjallajökull 2010 eruption using satellite remote sensing, lidar and WRF-Chem dispersion and tracking model, J. Geophys. Res., 117, D00U26, 2012.

APPENDIX – DEVELOPED CODE

This appendix describes the changes that were made to the WRF-Chem Version 3.9.1 base code in order to accomplish the modeling in Chapters 3 and 4 of this dissertation. In addition, it provides sample scripts and name lists that can be used to automate WRF-Chem, as was described in Chapter 4.

New code was added to the existing WRF-Chem Fortran 90 base code in the case of module_volc_emiss_driver.F and module_vash_settling.F. To help clarify which lines of code are modifications, the font has been adjusted such that modifications to the code are in **bold** and original code and code provided by other authors is not. Lines beginning with the bang (!) sign, as is customary with Fortran 90 code, and (#) pound sign, as is customary for Linux Bourne again shell scripts, are comments. Where appropriate, these comments attempt to describe the purpose of the code following the comment, as well as to cite the relevant literature the code was derived from. For compilation instructions and model downloads, refer to the WRF-Chem Users Guide for Version 3.9.1 and model download page, which may be accessed at the following website address: https://www2.mmm.ucar.edu/wrf/users/downloads.html (current as of November 2019).

Filename: module_vash_settling.F

File location: ./WRFV3/chem

Description: This file is available for download via the WRF-Chem download site provided above. The modifications below add volcanic ash aggregation capability to WRF-Chem (see Chapter 3 of this manuscript) and allow the user to specify the particle size explicitly for use in the near real time WRF-Chem capability (See Chapter 4 of this manuscript).

```
MODULE MODULE_VASH_SETTLING

CONTAINS

! Added u and v variables from dry deposition driver - SDE 3/2/16

! This initial subrouting is minimally edited. Variables are declared here

! that are passed on to the vsettling routing where the bulk of the

!modifications and aggregation driver routines exist.

SUBROUTINE vash_settling_driver(dt,config_flags,t_phy,moist,          &
      chem,rho_phy,dz8w,p8w,p_phy,                                    &
      ash_fall,dx,g,u,v,                                              &
      ids,ide, jds,jde, kds,kde,                                      &
      ims,ime, jms,jme, kms,kme,                                      &
      its,ite, jts,jte, kts,kte                                       )
  USE module_configure
  USE module_state_description
  USE module_model_constants, ONLY: mwdry
  IMPLICIT NONE
  TYPE(grid_config_rec_type),  INTENT(IN   )    :: config_flags

  INTEGER,      INTENT(IN   ) ::                &
                      ids,ide, jds,jde, kds,kde,          &
                      ims,ime, jms,jme, kms,kme,          &
```

```
                        its,ite, jts,jte, kts,kte
  REAL, DIMENSION( ims:ime, kms:kme, jms:jme, num_moist ),              &
      INTENT(IN ) ::                          moist
  REAL, DIMENSION( ims:ime, kms:kme, jms:jme, num_chem ),               &
      INTENT(INOUT ) ::                          chem

! Added initialization for u and v vectors - SDE 3/2/16
  REAL,  DIMENSION( ims:ime , kms:kme , jms:jme ),                      &
       INTENT(IN   ) ::  t_phy,p_phy,dz8w,p8w,rho_phy,u,v
  REAL,  DIMENSION( ims:ime , jms:jme ), INTENT(INOUT   ) ::  ash_fall
  REAL, INTENT(IN   ) :: dt,dx,g
  integer :: nmx,i,j,k,kk,lmx,iseas,idust

! Initializing u_vect array for derreferencing - SDE 2/16/2016
  real*8, DIMENSION (1,1,kte-kts+1) :: tmp,airden,airmas,p_mid,delz,rh,u_vect
  REAL*8, DIMENSION (1,1,kte-kts+1) :: q_vapor
  real*8, DIMENSION (1,1,kte-kts+1,4) :: sea_salt
  REAL*8, DIMENSION (ims:ime, kms:kme, jms:jme, num_moist) :: t_moist
!srf
  real*8, DIMENSION (1,1,kte-kts+1,10) :: ash

! Added vector for ash density in case we want to give each bin a
! different ash density. Parameterized for 2500 g/m3 currently. SDE 12/2015
real*8, DIMENSION (10), PARAMETER :: den_ash(10)=(/2500.,2500.,2500.,2500.,2500.,
&                                    2500.,2500.,2500.,2500.,2500. /)
```

```
real*8, DIMENSION (10), PARAMETER :: reff_ash(10)=(/0.5000D-3,
                                    &! 1.00 mm diameter
                                    0.3750D-3,&! 0.75 mm
                                                        0.1875D-3,&!
                                                        93.750D-6,&!
                                                        46.875D-6,&!
                                                        23.437D-6,&!
                                                        11.719D-6,&!
                                                        05.859D-6,&!
                                                        02.930D-6,&!
                                                        00.975D-6 /)! 3.9 um
```

! Declaring phi values from -1 (2mm) to 8 (3.9065 um) - Krumbien et al. (1981)

```
  REAL*8, DIMENSION (10), PARAMETER :: diam(10)=(/2.0e-3,1.0e-3,0.5e-3,0.25e-
3,125.e-6,62.5e-6,31.25e-6,15.625e-6,7.8125e-6,3.9065e-6 /)
real*8, DIMENSION (10) :: bstl_ash
integer iash
! bstl is for budgets
  real*8 conver,converi
      converi=1.e9
      conver=1.e-9
      lmx=kte-kts+1
      do j=jts,jte
      do i=its,ite
      kk=0
      bstl_ash(:)=0.
      do k=kts,kte
```

! The following line ingests the water vapor emissions from the model chemistry grid.

t_moist(i,k,j,p_qv) = moist(i,k,j,p_qv) + chem(i,k,j,p_vh2o)

```
      kk=kk+1
      p_mid(1,1,kk)=.01*p_phy(i,kte-k+kts,j)
      delz(1,1,kk)=dz8w(i,kte-k+kts,j)
      airmas(1,1,kk)=-(p8w(i,k+1,j)-p8w(i,k,j))/g
      airden(1,1,kk)=rho_phy(i,k,j)
      tmp(1,1,kk)=t_phy(i,k,j)
      q_vapor(1,1,kk) = t_moist(i,k,j,p_qv) !SDE 2NOV18
      rh(1,1,kk) = .95
      rh(1,1,kk) = MIN( .95, t_moist(i,k,j,p_qv) / & !SDE 2NOV18
           (3.80*exp(17.27*(t_phy(i,k,j)-273.)/ &
           (t_phy(i,k,j)-36.))/(.01*p_phy(i,k,j))))
      rh(1,1,kk)=max(1.0D-1,rh(1,1,kk))
!     Initializing U vector for shear calculations - SDE 3/2/16
      u_vect(1,1,kk)=u(i,k,j)
      enddo
!ash settling
        iseas=0
        idust=0
           iash =1
       kk=0
       !u_vect = u(i,j,k)
       do k=kts,kte
       kk=kk+1
       ash(1,1,kk,1)=chem(i,k,j,p_vash_1)*conver
       ash(1,1,kk,2)=chem(i,k,j,p_vash_2)*conver
       ash(1,1,kk,3)=chem(i,k,j,p_vash_3)*conver
       ash(1,1,kk,4)=chem(i,k,j,p_vash_4)*conver
```

```
        ash(1,1,kk,5)=chem(i,k,j,p_vash_5)*conver
        ash(1,1,kk,6)=chem(i,k,j,p_vash_6)*conver
        ash(1,1,kk,7)=chem(i,k,j,p_vash_7)*conver
        ash(1,1,kk,8)=chem(i,k,j,p_vash_8)*conver
        ash(1,1,kk,9)=chem(i,k,j,p_vash_9)*conver
        ash(1,1,kk,10)=chem(i,k,j,p_vash_10)*conver
        enddo
! diam, u_vect and delz have been added by SDE 2/2016
         call vsettling(1, 1, lmx, 10, g, diam, u_vect, &
                 dx, ash, tmp, p_mid, delz, airmas, q_vapor, &
                 den_ash, reff_ash, dt, bstl_ash, rh, idust, iseas,iash)
        kk=0
        ash_fall(i,j)=ash_fall(i,j)+sum(bstl_ash(1:10))
        do k=kts,kte
        kk=kk+1
          chem(i,k,j,p_vash_1)=ash(1,1,kk,1)*converi
          chem(i,k,j,p_vash_2)=ash(1,1,kk,2)*converi
          chem(i,k,j,p_vash_3)=ash(1,1,kk,3)*converi
          chem(i,k,j,p_vash_4)=ash(1,1,kk,4)*converi
          chem(i,k,j,p_vash_5)=ash(1,1,kk,5)*converi
          chem(i,k,j,p_vash_6)=ash(1,1,kk,6)*converi
          chem(i,k,j,p_vash_7)=ash(1,1,kk,7)*converi
          chem(i,k,j,p_vash_8)=ash(1,1,kk,8)*converi
          chem(i,k,j,p_vash_9)=ash(1,1,kk,9)*converi
          chem(i,k,j,p_vash_10)=ash(1,1,kk,10)*converi
        enddo
!ash settling end
```

```
      enddo
      enddo
END SUBROUTINE vash_settling_driver
! The following subroutine (vsettling)
! u wind speed is added here for shear calculations - SDE 2/16/2016
        subroutine vsettling(imx,jmx, lmx, nmx,g0, diam, u_vect, &
                dx, tc, tmp, p_mid, delz, airmas, q_vapor, &
                den, reff, dt, bstl, rh, idust, iseas,iash)
!*******************************************************************************
!
!   Calculate the loss by settling, using an implicit method
!
!   Input variables:
!    SIGE(k)        - sigma coordinate of the vertical edges
!    PS(i,j)        - Surface pressure (mb)
!    TMP(i,j,k)     - Air temperature  (K)
!    CT(i,j)        - Surface exchange coeff for moisture
! *******************************************************************************
  IMPLICIT  NONE
  INTEGER, INTENT(IN) :: imx, jmx, lmx, nmx,iseas,idust,iash
  INTEGER :: ntdt
  REAL, INTENT(IN) :: dx,dt,g0 ! ,dyn_visc
  REAL*8,    INTENT(IN) :: tmp(imx,jmx,lmx), delz(imx,jmx,lmx), &
                    airmas(imx,jmx,lmx), rh(imx,jmx,lmx), &
                    den(nmx), reff(nmx), p_mid(imx,jmx,lmx), &
                    diam(nmx), q_vapor(imx,jmx,lmx)
  REAL*8, INTENT(INOUT) :: tc(imx,jmx,lmx,nmx)
```

```
  REAL*8, INTENT(IN)    :: u_vect(imx,jmx,lmx)
  REAL*8, INTENT(OUT)   :: bstl(imx,jmx,nmx)

  REAL*8    :: tc1(imx,jmx,lmx,nmx), dt_settl(nmx), rcm(nmx), rho(nmx)
  INTEGER :: ndt_settl(nmx)
  REAL*8    :: dzmin, vsettl, dtmax, pres, rhb, rwet(nmx), ratio_r(nmx)
  REAL*8    :: addmass,c_stokes, free_path, c_cun, viscosity, vd_cor,          growth_fac
  REAL,    PARAMETER :: dyn_visc = 1.5E-5
  INTEGER :: k, n, i, j, l, l2
  ! for sea-salt:
  REAL*8, PARAMETER :: c1=0.7674, c2=3.079, c3=2.573E-11, c4=-1.424
  ! for OMP:
  REAL*8 :: rwet_priv(nmx), rho_priv(nmx), dy
! the following variables were added for the
! ash Aggregation routine SDE - 12 / 2015
! The following two lines are used for the WRF-Chem debugger
  CHARACTER (LEN=80) :: message
  INTEGER   :: debug_level_yu

! Variables in the following line are as follows:
! ntot – The total number of particles in a computational slab. The
!      equation governing this variable was adapted from
!      Equation 10 in Costa et al. (2010) and Equation B1-B4 from
!      Folch et al. (2015). This is a summation of the variable
!      nbin that is declared and discussed later.
! dntot – The total change in the number of particles on the computational
!       slab due to aggregation. The equation governing this variable
```

```
!       was adapted from Equation 23 in Costa et al. (2010)
!       and Equation 24 in Folch et al. (2015) and corresponds
!       to Equation 3.2.2 in this manuscripts
! ab – This is the Brownian motion kernel, Ab, which is discussed in Chapter
!       3 of this manuscript and was adapted from Equations 14 and 15
!       from Costa et al. (2010) and Equation 41a from Folch et al.
!       (2015). It further corresponds to Equation 3.2.3
!       of this manuscript
! as – This is the shear kernel, As, which is discussed in Chapter of this
!     manuscript and was adapted from Equations 16 and 17 of
!     Costa et al. (2010) as well as Equation 41B of Foch et al. (2015). It
!     further corresponds to Equation 3.2.4 of this manuscript.
! ads – This is the differential sedimentation kernel, Ads, which is
!     discussed in Chapter 3 of this manuscript and was adapted from
!     Equations 20 and 21 of Costa et al. (2010) and Equation 41C of
!     Folch et al. (2015). It further corresponds to Equation 3.2.5 of this
!     manuscript
  REAL*8    :: ntot, dntot, ab, as, ads

! The following variables are calculated using the same equation as dntot
! above, but consider the change in number of primary particles due to
! each kernel. Only one kernel at a time is calculated using these variables
! for use in the sensitivity studies in Chapter 3 of this manuscript.
  REAL*8    :: dntotas, dntotab, dntotads
```

```
! The following variables are also used in the calculation of the
! number of primary particles going to form aggregates. The following
! is a description of each variable:
! alpha_sum – This is the sticking efficiency. The Equation governing this
!     variable was developed in Chapter 3 of this manuscript and corresponds
!     to Equation 3.2.7.
! alpha2_sum – This is a temporary variable used to calculate the overall
!     sticking efficiency of the IF/THEN statement that comes later.
! phi – This is used to calculate the solid volume fraction which is the
!     mass divided by the density. Its use arises from Equation 12 in
!     Costa et al. (2010) and Table 2 from Folch et al. (2015).
  REAL*8    :: alpha_sum, alpha2_sum, phi

! alpha – This is the direct calculation of Equation 3.2.7 for each of
!     the particle sizes.
! totmass – This is the sum of the massbin variable and represents the total
!     mass in a computational grid.
! pp – This is the density of volcanic ash. As discussed in Chapter 3
!     of this manuscript and in Costa et al. (2010) this
!     is an assumed value of 2500 kg m-3.
  REAL*8    :: alpha, totmass, pp

! nfrac – Used to calculate the fraction of mass that each bin
!     contributes to the overall grid cell mass.
! nbin – The number of particles of a particular volcanic ash bin
!     that is used to calculate ntot. Again, this number is calculated
!     based on Equation 10 in Costa et al. (2010) and Equations B1-B4
```

```
!     in Folch et al. (2015).
! massbin – The total mass of each volcanic ash bin in the computational
!     grid that is summed to create the earlier totmass variable.
! dmass – This variable is the back calculation of ntot. It is used to
!    calculate the total mass change of a computational grid using the
!    number of particles that left the grid to form aggregation (the
!    back conversion of the dntot variable). Again, this variable is
!    based on the Equations 10 and 23 in Costa et al. (2010) and
!    Equations 34 and B1-B4 in Folch et al. (2015).
  REAL*8, DIMENSION(10) ::  nfrac, nbin, massbin, dmass

! alpha_n – Corresponds to Equation 3.2.7 and is used to calculate the
!    individual sticking efficiency of each bin to every other bin.
!    This is computed independently since the sticking efficiency
!    is based on the particle size.
  REAL*8, DIMENSION(10) ::  alpha_n

! END OF DECLARATION OF VARIABLES FOR THE AGGREGATION ROUTINE
! Instead of passing the dy variable from the grid, we just reference
! dx. This requires the model to use a square model domain and this is
! mentioned in the text of Chapter 3.
  dy=dx

! Here we specify the fractal dimension. As mentioned in Chapter 3 of
! this manuscript, a fractal dimension of 3.0 was chosen for the bulk
! of the studies. The development of the fractal dimension is discussed
! in Chapter 3, as well as in Costa et al. (2010), Folch et al. (2010)
```

! and Dekkers and Friedlander (2002). The initialization of this variable

! in memory is in the previous subroutine.

df = 3.0

! An array of densities was initialized earlier and may be used, however

! we assume a density of 2,500 kg m^{-3} in this study based on

! Costa et al. (2010) and Folch et al. (2010) as well as the literature

! references that discuss this assumption in Chapter 3 of this manuscript.

pp = 2500.

! The following code is preexisting code that calculates the

! settling of volcanic ash particles and was not modified in this work.

```
! Settling routine stuff
 ! executable statements
! IF (type) /= 'dust' .AND. TRIM(aero_type) /= 'sea_salt') RETURN
 if(idust.ne.1.and.iseas.ne.1.and.iash.ne.1)return
 WHERE (tc(:,:,:,:) < 0.0) tc(:,:,:,:) = 1.0d-32
 dzmin = MINVAL(delz(:,:,:))
 IF (idust == 1)    growth_fac = 1.0
 IF (iseas == 1)    growth_fac = 3.0
 IF (iash  == 1)    growth_fac = 1.0
 DO k = 1,nmx
   ! Settling velocity (m/s) for each tracer (Stokes Law)
   ! DEN        density                  (kg/m3)
   ! REFF       effective radius           (m)
   ! dyn_visc   dynamic viscosity          (kg/m/s)
   ! g0         gravity                  (m/s2)
```

```
    ! 3.0        corresponds to a growth of a factor 3 of radius with 100% RH
    ! 0.5        upper limit with temp correction
    tc1(:,:,:,k) = tc(:,:,:,k)
    vsettl = 2.0/9.0 * g0 * den(k) * (growth_fac*reff(k))**2 / &
           (0.5*dyn_visc)
    ! Determine the maximum time-step satisfying the CFL condition:
    ! dt <= (dz)_min / v_settl
    ntdt=INT(dt)
    dtmax = dzmin / vsettl
    ndt_settl(k) = MAX( 1, INT( ntdt /dtmax) )
    ! limit maximum number of iterations
    IF (ndt_settl(k) > 12) ndt_settl(k) = 12
    dt_settl(k) = REAL(ntdt) / REAL(ndt_settl(k))

    ! Particles radius in centimeters
    IF (iseas.eq.1)rcm(k) = reff(k)*100.0
!srf    IF (idust.eq.1)then
    IF (idust.eq.1   .or. iash==1)then
        rwet(k) = reff(k)
        ratio_r(k) = 1.0
        rho(k) = den(k)
     endif
  END DO
  ! Solve the bidiagonal matrix (l,l)
!$OMP PARALLEL DO &
!$OMP DEFAULT( SHARED ) &
!$OMP PRIVATE( i,   j,   l,   l2, n,   k,   rhb, rwet_priv, ratio_r, c_stokes)&
```

```
!$OMP PRIVATE( free_path, c_cun, viscosity, rho_priv, vd_cor )
 ! Loop over latitudes
 DO j = 1,jmx
   DO k = 1,nmx
     IF (idust.eq.1 .or. iash==1) THEN
       rwet_priv(k) = rwet(k)
       rho_priv(k)  = rho(k)
     END IF
     DO n = 1,ndt_settl(k)
       ! Solve each vertical layer successively (layer l)
       DO l = lmx,1,-1
         l2 = lmx - l + 1
!        DO j = 1,jmx
         DO i = 1,imx
           ! Dynamic viscosity
           c_stokes = 1.458E-6 * tmp(i,j,l)**1.5/(tmp(i,j,l) + 110.4)
           ! Mean free path as a function of pressure (mb) and
           ! temperature (K)
           ! order of p_mid is top->sfc
           free_path = 1.1E-3/p_mid(i,j,l2)/SQRT(tmp(i,j,l))
           ! Slip Correction Factor
           c_cun = 1.0+ free_path/rwet_priv(k)* &
               (1.257 + 0.4*EXP(-1.1*rwet_priv(k)/free_path))
           ! Corrected dynamic viscosity (kg/m/s)
           viscosity = c_stokes / c_cun
           ! Settling velocity
           vd_cor = 2.0/9.0*g0*rho_priv(k)*rwet_priv(k)**2/viscosity
```

```
            ! Update mixing ratio
            ! Order of delz is top->sfc
            IF (l == lmx) THEN
              tc(i,j,l,k) = tc(i,j,l,k) / &
                  (1.0 + dt_settl(k)*vd_cor/delz(i,j,l2))
            ELSE
              tc(i,j,l,k) = 1.0/(1.0+dt_settl(k)*vd_cor/delz(i,j,l2))&
                  *(tc(i,j,l,k) + dt_settl(k)*vd_cor /delz(i,j,l2-1) &
                  * tc(i,j,l+1,k))
            END IF
          END DO
!       END DO
      END DO
    END DO
  END DO
END DO
!$OMP END PARALLEL DO

  DO n = 1,nmx
    DO i = 1,imx
      DO j = 1,jmx
        bstl(i,j,n) = 0.0
        addmass=0.
        DO l = 1,lmx
          addmass=addmass+(tc(i,j,l,n) - tc1(i,j,l,n)) * airmas(i,j,l)
          IF (tc(i,j,l,n) < 0.0) tc(i,j,l,n) = 1.0D-32
        END DO
```

```
        if(addmass.gt.0.)addmass=0
        bstl(i,j,n) = bstl(i,j,n) - addmass
      END DO
    END DO
  END DO

!*************************************************************************
!  Do loop for calculating aggregation at each i,j,k grid cell at time t
!  All loops including nmx begin at index 2, since vash_1 is not included
!  as it is used as the aggregation bin.
!*************************************************************************
!Loop definitions
!i,imx - grid cells in x
!j,jmx - grid cells in y
!j,lmx - grid cells in z - vertical
!time is passed by subroutine
    DO i = 1,imx
      DO j = 1,jmx
        DO l = 1,lmx

! The following line calculates the Brownian Kernel. This calculation
! is based on Equation 41a in Folch et al. (2015) and Equations 14 and 15
! in Costa et al. (2010).
          ab = ((-4./3.)*1.381e-23*tmp(i,j,l))/viscosity
```

```
! The following lines calculates the shear kernel. It is based on
! Equations 16 and 17 in Costa et al. (2010) and Equation 41b in
! Folch et al. (2015). The IF/ELSE statement is used to select which
! vertical layer to use. If the bottom layer is selected then the grid
! cell above is used. Otherwise grid cells below the current cell are used.
        IF (l.eq.1) THEN
          as = -(2./3.)*((ABS(u_vect(i,j,l)- &
              u_vect(i,j,l+1)))/delz(i,j,l))* &
              ((6./3.141592)**(1./3.))**(3.)
        ELSE
          as = -(2./3.)*((ABS(u_vect(i,j,l)-u_vect(i,j,l &
              -1)))/delz(i,j,l))* &
              ((6./3.141592)**(1./3.))**(3.)
        END IF

! The following lines calculate the differential sedimentation kernel
! based on Equations 21 and 22 from Costa et al. (2010) and Equation 41c
! from Folch et al. (2015). Note that the viscosity variable is defined
! and calculated in the original code and is not updated here. Also note
! that the hardcoded density, rather than the array of densities, is
! used, corresponding to 2,500 kg m-3. Again, the choice of this
! assumption is discussed in the Chapter 3 text.
        ads = ((-3.1416*(pp-50.)*9.81* &
            (((6./3.141592)**(1./3.))**(4.)))/(48.*viscosity))
```

```
! Initialize phi, ntot and totmass variables with 0 to avoid compiler errors.
        phi = 0.
        ntot = 0.
        totmass=0.

! The following code block loops over n ash bins (VASH_2 through VASH_10)
! and calculates the individual sticking efficiencies based on Equation
! 3.2.7 in this manuscript for each of the inter-bin collisions.
! This block acts as a lookup table, selecting which efficiency exponent in
! Table 3.3 is used for the calculation of alpha.  The values were created
! from a literature review conducted by Van Eaton et al. (2015) and
! is further discussed in Chapter 3. RH is a unitless percent, diameter
! is converted to meters via 10^6 conversion.
        DO n = 2, nmx
         IF(rh(i,j,l).lt.0.01)THEN
          alpha_n(n)=exp(-diam(n)*1.e6*0.02)
         ELSEIF(rh(i,j,l).ge.0.01.and.rh(i,j,l).le.0.10)THEN
          alpha_n(n)=exp(-diam(n)*1.e6*0.008)
         ELSEIF(rh(i,j,l).gt.0.10.and.rh(i,j,l).le.0.150)THEN
          alpha_n(n)=exp(-diam(n)*1.e6*0.004)
         ELSEIF(rh(i,j,l).gt.0.150.and.rh(i,j,l).le.0.25)THEN
          alpha_n(n)=exp(-diam(n)*1.e6*0.002)
         ELSEIF(rh(i,j,l).gt.0.25.and.rh(i,j,l).le.1.0)THEN
          alpha_n(n)=exp(-diam(n)*1.e6*0.00005)
         ELSE
```

```
! If there is an error getting the RH, we use a default value
! from Costa et al., 2010 assuming ice - This will greatly underestimate
! the aggregation.
            alpha_n(n)=0.09
          END IF
        END DO

! The following code block loops over n ash bins and ultimately calculates
! ntot, the total number of particles in a computational grid cell. The
! description of each of these variables is provided in comments above
! their initialization, but a brief description is provided again:
! 1) massbin - The mass of ash in each bin by converting the chemistry
!    grid mixing ratio (tc) of kg/kg to kg/m3 through multiplication to
!    the mixing ratio of the mass of air in the cell (airmas). Note
!    the airmas variable is calculated previously in the unmodified code.
!    The 10^3 factor brings units from grams to kg, which is required
!    to match the density of ash used (2,500 kg m^3).

        massbin(n)=(tc(i,j,l,n)*airmas(i,j,l))/10e3!kg/m3

! 2) totmass – The total mass by summing the mass in each bin (massbin)
        totmass = totmass + massbin(n) !kg/m3

! 3) phi – The solid volume fraction is calculated by dividing the total mass
!         by the density.
           phi = phi + (((tc(I,j,l,n)*airmas(I,j,l))/10.e3*pp)
```

```
! 4) nbin – Calculate the number of primary particles in each bin. Again,
!       this is calculated based on Equation 10 in Costa et al. (2010)
!       and Folch et al. (2015), Equations B1.4. "diam" here refers to
!       the diameter of each bins particles and was defined earlier.
          nbin(n)=((6.*massbin(n))/(3.141592*2600.))*&
          ABS((1/(diam(n-1)**3.))-(1/(diam(n)**3.)))

! 5) ntot – Calculate the total number of primary particles in each
!       Grid cell by summing the individual bins (nbin).
          ntot = ntot + nbin(n)
        END DO

! This is the end of the calculation of the number of primary particles.
! In calculating ntot above, we did not multiply by 1/3ln(2) as per
! Equations B1-4 in Folch et al. 2015 so this is done here:
        ntot = ntot * 1.107309 ! Where 1.107309 = 1/3ln(2)

! The following code block calculates the fraction of mass (nfrac) that each
! bin contributes to the overall grid cell particle concentration.
! This is then used to calculate the number of particles
! in each bin that will go to create aggregates. The DO loop begins
! with n = 2 since bin 1 has been repurposed as the aggregate bin.
        DO n = 2, nmx
```

```
! Here, this line divides the number of particles in each bin (nbin)
! by the total number of particles in the grid (ntot), thus calculating
! the fraction of those particles (nfrac) in the grid coming from each bin.
          nfrac(n) = nbin(n)/ntot
        END DO
! The sticking efficiency of each bin was calculated earlier (alpha_n).
! using the IF/THEN lookup table code block.
! The overall sticking efficiency (alpha) is calculated below by
! weighting each of the individual sticking efficiencies in the
! alpha_n array using the fraction of each bin making up the
! computational grid (nfrac).

! Here, alpha_sum and alpha2_sum are initialized for the following DO loop
! using 0 in order to avoid compiler warnings.
        alpha = 0.0
        alpha_sum=0.0
        alpha2_sum=0.0

! Calculate the numerator (alpha2_sum) and the denominator (alpha_sum).
! The calculation is algebraically simplified. The sticking efficiency
! of each bin is weighted by each bins overall contribution to the
! total number density of the grid cell.
        DO n = 2,nmx
         IF(n.eq.2)THEN
          alpha_sum=alpha_sum+(nfrac(n)*nfrac(n+1))
         ELSE
          alpha_sum=alpha_sum+(nfrac(n-1)*nfrac(n))
```

```
          END IF
          alpha2_sum=alpha_sum*alpha_n(n)
        END DO

! Calculate the total sticking efficiency by dividing the contribution
! of each bin's efficiency to the total.
        alpha = alpha2_sum/alpha_sum

! The next equation calculates the total number of primary particles
! going towards the formation of aggregates (dntot) and is based on
! Equation 23 in Costa et al. (2010) and Equation 34 in Folch et al. (2015)
! Again, ntot is the total number of primary particles available
! for aggregation on a particular computational space and originates from
! Equation 10 in Costa et al. (2010) and Equations 1-4B in
! Folch et al. (2015). The fractal dimension, df, is defined
! above in the variable declaration and the choice of the fractal
! dimension is discussed in Folch et al. (2010), Costa et al. (2010), and
! in Chapter 3 of this manuscript.
        dntot=((alpha*(ABS(ab*(ntot)*ntot))&
             +(ABS(as*(phi**(3./df))*(ntot**(2.-(3./df)))))&
             +(ABS(ads*(phi**(4./df))*(ntot**(2.-(4./df))))))*dt)

! These equations are for use in running the code with single
! kernels - Comment previous equation and use these instead to
! inspect AS, ADS and AB independently.
! dntot=alpha*(ABS(ab*(ntot)*ntot))*dt
! dntot=alpha*ABS(ads*(phi**(4./df))*(ntot**(2.-(4./df))))*dt
```

```
! dntot=alpha*ABS(as*(phi**(3./df))*(ntot**(2.-(3./df))))*dt

! The following code block converts the total number of primary particles
! going to form aggregates (dntot) to a total mass change of each bin (dmass)
! - this conversion is based on Equation 10 in Costa et al. (2010) and
! is the reverse calculation of ntot.
! The dmass variable needs to be converted to the same units as
! the "tc" variable (an original variable in the unmodified code) which
! is a mixing ratio so we append the conversion (airmas*10e-3) since
! dmass is in kg m^-3 and airmass is in g m^-3.
! Additionally, the nfrac variable is used to assess the fraction of the
! total bass loss attributed from each bin.
        DO n=2, nmx
          dmass(n)=((((1./6.)*dntot*pp*3.14*diam(n)**(3.))*1000)&
              /airmas(i,j,l))*nfrac(n)
        END DO

! The following do loop updates the mixing ratio (tc) by subtracting
! the mass from each bin and adding to VASH_1, the aggregation bin. Again
! the units match here as mixing ratios.
        DO n=2, nmx
          IF (dmass(n) < 0.0) dmass(n) = 1.0D-32
          tc(i,j,l,n)=tc(i,j,l,n)-dmass(n)
          IF (tc(i,j,l,n) < 0.0) tc(i,j,l,n) = 1.0D-32
          tc(i,j,l,1)=tc(i,j,l,1)+dmass(n)
        END DO
    END DO
```

END DO

END DO

END SUBROUTINE vsettling

END MODULE MODULE_VASH_SETTLING

References used in the commented portions of this file:

Costa, A., Folch, A. and Macedonio, G.: A model for wet aggregation of ash particles in volcanic plumes and clouds: 1. Theoretical formulation, J. Geophys. Res. Solid Earth, 115(B9), B09201, doi:10.1029/2009JB007175, 2010.

Dekkers, P. J. and Friedlander, S. K.: The Self-Preserving Size Distribution Theory: I. Effects of the Knudsen Number on Aerosol Agglomerate Growth, J. Colloid Interface Sci., 248(2), 295–305, doi:10.1006/jcis.2002.8212, 2002.

Folch, A., Costa, A., Durant, A. and Macedonio, G.: A model for wet aggregation of ash particles in volcanic plumes and clouds: 2. Model application, J. Geophys. Res. Solid Earth, 115(B9), B09202, doi:10.1029/2009JB007176, 2010.

Folch, A., Costa, A. and Macedonio, G.: FPLUME-1.0: An integrated volcanic plume model accounting for ash aggregation, Geosci. Model Dev. Discuss., 8(9), 8009–8062, doi:10.5194/gmd-9-431-2016, 2016.

Filename: module_volc_emiss_driver.F

File location: ./WRFV3/chem

Description: This file is available for download via the WRF-Chem download site provided above. The modifications below add the ability to model 5 different plume heights to WRF-Chem in a single run. For modifications to the particle sizes, see the code above listed in module_vash_settling.F. Text that is not bold face was developed by Marcus Hirtl and is described in:

> Hirtl, M., Stuefer, M., Arnold, D., Grell, G., Maurer, C., Natali, S., Scherllin-Pirscher, B. and Webley, P.: The effects of simulating volcanic aerosol radiative feedbacks with WRF-Chem during the Eyjafjallajökull eruption, April and May 2010, Atmos. Environ., 198, 194–206, doi:10.1016/j.atmosenv.2018.10.058, 2019.

```
Module module_volc_emiss_driver

CONTAINS

! Water vapor emissions were added using the p_ke_h2o variable.

SUBROUTINE volcemiss(emis_vol,ims,ime,kms,kme,&

                jms,jme,num_emis_vol,ni,nj,&

                julday_wrf,curr_secs,xlong,&

                xlat,z,i,j,kts,dx,p_e_vash1,&

                p_e_vash2,p_e_vash3,p_e_vash4,&

                p_e_vash5,p_e_vash6,p_e_vash7&,

                p_e_vash8,p_e_vash9,p_e_vash10&

                ,p_e_vso2,p_ke_h2o,z_at_w,&

                gmt,emissoptvol)

IMPLICIT NONE

INTEGER :: ims,ime,kms,kme,jms,jme,num_emis_vol,ni,nj,julday_wrf,emissoptvol

REAL :: emis_vol(ims:ime,kms:kme,jms:jme,num_emis_vol),&

     xlong(ims:ime,jms:jme),xlat(ims:ime,jms:jme)

REAL :: z(ims:ime,kms:kme,jms:jme)
```

```
REAL (KIND=8) :: curr_secs,secs
REAL :: kcurr_time
INTEGER :: k,i,j,kts
INTEGER :: hgt,timestep,ntimestep

! The H20_EMIS variable was added to be able to read in water vapor emissions
REAL,ALLOCATABLE :: ASH(:,:),SO2(:,:),ASH_EMIS(:),SO2_EMIS(:),H2O_EMIS(:)
INTEGER,ALLOCATABLE :: DATE(:),TIME(:),JULDAY(:),DURATION(:),TIMEW(:)
REAL,ALLOCATABLE :: HEIGHT(:)

! The HEIGHT_OFFSETS variable was added so that two levels above and two
! levels below the plume height couple be calculated for a total of
! 5 height levels.
REAL,ALLOCATABLE :: HEIGHT_OFFSETS(:)

! The k_u1, k_u2, k_d1, and k_d2 variables store the model vertical grid cell
! index that corresponds to the input height as well as the offsets.
INTEGER :: k_u1,k_u2,k_d1,k_d2
INTEGER :: year,month,day
INTEGER :: timestep_curr
INTEGER :: nlevels,ref_date
INTEGER :: nr_abschnitte_top,nr_abschnitte_unten
REAL :: volc_top,volc_unten
REAL,ALLOCATABLE :: VOLC_HEIGHTS_TOP(:),VOLC_HEIGHTS_BOTTOM(:)
REAL,ALLOCATABLE :: hohe_wrf_top(:),hohe_wrf_middle(:),&
```

```
            hohe_wrf_unten(:),volc_emiss_wrf(:)
REAL :: total_mass_extern,total_mass_wrf,mass_wrf_k
REAL :: total_mass_extern_so2,total_mass_wrf_so2,mass_wrf_k_so2
INTEGER :: kk
LOGICAL :: level_check
REAL :: HEIGHT_SURFACE
REAL :: area
REAL :: dx

! The p_ke_h2o variable was added to account for the water vapor emissions
! that will be read in via the volc_d01.asc name list.
INTEGER :: p_e_vash1,p_e_vash2,p_e_vash3,p_e_vash4,&
      p_e_vash5,p_e_vash6,p_e_vash7,p_e_vash8,&
      p_e_vash9,p_e_vash10,p_e_vso2,p_ke_h2o
INTEGER :: bi
INTEGER :: time_before_volc,time_wrf,time_after_volc
REAL :: OFFSET_EXT_WRF
REAL :: percen_mass_umbrel,base_umbrel,curr_hours
INTEGER :: ivolcano
REAL :: gmt
INTEGER :: gmtm,gmtp
REAL :: begday,beghr,begmin,endday,endhr,endmin
REAL,ALLOCATABLE :: erup_beg(:,:,:), erup_end(:,:,:),erup_hgt(:,:,:),&
            erup_ash(:,:,:)!,erup_so2(:,:,:),erup_h2o(:,:,:)
INTEGER :: ki
```

```
REAL :: so2_mass,h2o_flux,emiss_ash_mass
REAL :: emiss_ash_height,eh,erup_so2,erup_h2o
REAL :: ashz_above_vent
REAL :: z_at_w(ims:ime,kms:kme,jms:jme )
INTEGER :: k_final,k_initial
INTEGER :: kk4,x1,ko,kl
!REAL :: vert_mass_dist(kts:kme)
INTEGER :: p_ksbin1,p_ksbin2,p_ksbin3,p_ksbin4&
      ,p_ksbin5,p_ksbin6,p_ksbin7,p_ksbin8,&
      p_ksbin9,p_ksbin10
REAL :: VOLC_HOUR,VOLC_MIN,VOLC_SEC,VOLC_TIME

! This section of the code reads in the variables from the volc_d01.asc
! namelist. The following line opens the file.
OPEN(14,FILE="volc_d01.asc")

! The next line skips over the header information.
READ(14,*)

! The next line reads in the total number of timesteps that are used. This is
! automatically 3 days of 3 hourly rates for 24 total. This is set as a read
! in variable so that the user may specify their own value.
READ(14,*) ntimestep
percen_mass_umbrel=.75
base_umbrel=.25
```

```
ivolcano=0
area=dx*dx
! The number of height levels is hard coded at 5. This may be modified here.
nlevels=5
emis_vol=0
OFFSET_EXT_WRF=0

! The next line reads in the height offsets from volc_d01.asc. These are done
! as multipliers such that a value of 0.5 would mean half the height of the
! input plume height.
ALLOCATE(HEIGHT_OFFSETS(nlevels))
READ(14,*) (HEIGHT_OFFSETS(bi),bi=1,nlevels)

! The next lines read in the corresponding grid cells of the volcano. In the
! near real time WRF-Chem this is always set to 200, 200 as the volcano is
! always in the center of the domain of 400 x 400 grid cells (See Table 4.3
! in this manuscript).
READ(14,*) ni
READ(14,*) nj

! The next line skips over the second header line in the volc_d01.asc
! name list.
READ(14,*)

! The H20_EMIS variable was added to receive water vapor emissions. The
```

```
! following section allocates the variable and the following READ
! section ingests it from the volc_d01.asc file.
ALLOCATE(DATE(ntimestep),TIME(ntimestep),&
      HEIGHT(ntimestep),DURATION(ntimestep),&
      ASH_EMIS(ntimestep),SO2_EMIS(ntimestep),&
      H2O_EMIS(ntimestep),TIMEW(ntimestep))
      ALLOCATE(JULDAY(ntimestep))
DO timestep=1,ntimestep
  READ(14,*) DATE(timestep),TIME(timestep),&
         DURATION(timestep),HEIGHT(timestep)&
         ,ASH_EMIS(timestep),SO2_EMIS(timestep),&
         H2O_EMIS(timestep)

! The next block of code concerns the timing of the emissions and is
! original code by Marcus Hirtl.
  year=INT(DATE(timestep)/10000)
  ref_date=year*10000+0101
  JULDAY(timestep)=juldate(DATE(timestep),000000)-juldate(ref_date,000000)
  VOLC_HOUR=INT(TIME(timestep)/10000.)
  VOLC_MIN=INT((TIME(timestep)-VOLC_HOUR*10000.)/100.)
  VOLC_SEC=INT((TIME(timestep)-VOLC_HOUR*10000.-VOLC_MIN*100.))
  TIMEW(timestep)=VOLC_HOUR*3600.+VOLC_MIN*60.+VOLC_SEC
END DO
CLOSE(14)
! This is the end of reading the volc_d01.asc file.
```

```
secs=mod(gmt*3600.+curr_secs,86400.)

write(*,*) "PROBLEM2",julday_wrf,gmt,curr_secs,secs

write(*,*) "PROBLEM2"

! CHECK IF TIMES FIT BEG

timestep_curr=0

DO timestep=1,ntimestep-1 ! last time step in input file should have 0 emission as it should be the
end time for the last intervall

  time_before_volc=JULDAY(timestep)*100000.+TIMEW(timestep)

  time_wrf=julday_wrf*100000.+secs ! year*10000000000 should be here as well

  time_after_volc=JULDAY(timestep+1)*100000.+TIMEW(timestep+1)

END DO

emiss_ash_height = HEIGHT(timestep_curr)

eh=ASH_EMIS(timestep_curr)

emiss_ash_mass=eh*1.e9/area

erup_so2=SO2_EMIS(timestep_curr)


! The following line reads the current time steps water vapor

! emission rate

erup_h2o=H2O_EMIS(timestep_curr)

so2_mass=erup_so2*3600.*1.e9/64./area !molecular weight SO2 is 64


! The next line calculates the eruption rate to kg ^3.

h2o_flux=erup_h2o/area ! kg/s ---> kg/(m2s)

ashz_above_vent=emiss_ash_height - z_at_w(ni,kts,nj)

IF(ashz_above_vent.lt.0)THEN
```

```
  ashz_above_vent=0.0
ENDIF
! The following lines were added by Dr. Jiang Zhu jzhu (20190702) to
! initialize the 5 plume heights. This helps to avoid a segmentation
! fault in instances where the volcano height is smoothed by the
! model's terrain resolution.
k_d2=kts+1
k_d1=kts+1
k_final=kts+1
k_u1=kts+1
k_u2=kts+1

! The following DO loop determines the index of the model's vertical
! grid cell, k, that corresponds to the initial height. This will be
! the limit of the emissions routines later in the code for this height.
! The loop starts at the top of the model and iterates downward,
! kme (top cell number) to kts (bottom cell number) and tests if the
! height at that cell is higher or lower than the specified initial
! height, which is the 3rd index in the HEIGHT_OFFSETS array. It records
! the cell corresponding to the top of the plume as k_final.
DO k=kme-1,kts,-1
IF(z_at_w(ni,k,nj) < (emiss_ash_height*&
              HEIGHT_OFFSETS(3))) THEN k_final=k+1
   EXIT
  ENDIF
```

```
ENDDO



! The next do loop determines the model vertical grid cell corresponding
! to the first height offset above the original input plume using the
! same methodology as before.
DO k=kme-1,kts,-1
  IF(z_at_w(ni,k,nj) < (emiss_ash_height*&
                HEIGHT_OFFSETS(4))) THEN k_u1=k+1
    EXIT
  ENDIF
ENDDO

! The next do loop determines the model vertical grid cell corresponding
! to the second height offset above the original input plume using the
! same methodology as before.
DO k=kme-1,kts,-1
  IF(z_at_w(ni,k,nj) < (emiss_ash_height*&
                HEIGHT_OFFSETS(5))) THEN k_u2=k+1
    EXIT
  ENDIF
ENDDO
```

```
! The next do loop determines the model vertical grid cell corresponding
! to the first height offset below the original input plume using the
! same methodology as before.
DO k=kme-1,kts,-1
  IF(z_at_w(ni,k,nj) <= (emiss_ash_height*&
                  HEIGHT_OFFSETS(2))) THEN k_d1=k+1
    EXIT
  ENDIF
ENDDO

! The next do loop determines the model vertical grid cell corresponding
! to the second height offset below the original input plume using the
! same methodology as before.
DO k=kme-1,kts,-1
  IF(z_at_w(ni,k,nj) <= (emiss_ash_height*&
                  HEIGHT_OFFSETS(1))) THEN k_d2=k+1
    EXIT
  ENDIF
ENDDO

! The following IF/THEN statement ensures that volcanic ash
! will not be initialized below the vent and was added by Jiang Zu.
IF(z_at_w(ni,kts,nj) > (emiss_ash_height*&
```

HEIGHT_OFFSETS(1))) THEN k_d2=(kts+1)

ENDIF

```
do ko=1,kme
   emis_vol(ni,ko,nj,p_e_vash1)=0.0
   emis_vol(ni,ko,nj,p_e_vash2)=0.0
   emis_vol(ni,ko,nj,p_e_vash3)=0.0
   emis_vol(ni,ko,nj,p_e_vash4)=0.0
   emis_vol(ni,ko,nj,p_e_vash5)=0.0
   emis_vol(ni,ko,nj,p_e_vash6)=0.0
   emis_vol(ni,ko,nj,p_e_vash7)=0.0
   emis_vol(ni,ko,nj,p_e_vash8)=0.0
   emis_vol(ni,ko,nj,p_e_vash9)=0.0
   emis_vol(ni,ko,nj,p_e_vash10)=0.0
   !if(config_flags%emiss_opt_vol == !2)&
      emis_vol(ni,ko,nj,p_e_vso2)=vert_mass_dist(ko)*so2_mass

   if(emissoptvol == 2)emis_vol(ni,ko,nj,p_e_vso2)=0.0
```

! Added a line to store the water vapor emissions into the WRF-Chem

! chemistry grid via p_ke_h2o.

```
   if(emissoptvol == 2)emis_vol(ni,ko,nj,p_ke_h2o)=0.0
enddo
   emis_vol(ni,k_d2,nj,p_e_vash1)=emiss_ash_mass
   emis_vol(ni,k_d1,nj,p_e_vash2)=emiss_ash_mass
   emis_vol(ni,k_final,nj,p_e_vash3)=emiss_ash_mass
```

```
   emis_vol(ni,k_u1,nj,p_e_vash4)=emiss_ash_mass
   emis_vol(ni,k_u2,nj,p_e_vash5)=emiss_ash_mass
   emis_vol(ni,k_d2,nj,p_e_vash6)=emiss_ash_mass
   emis_vol(ni,k_d1,nj,p_e_vash7)=emiss_ash_mass
   emis_vol(ni,k_final,nj,p_e_vash8)=emiss_ash_mass
   emis_vol(ni,k_u1,nj,p_e_vash9)=emiss_ash_mass
   emis_vol(ni,k_u2,nj,p_e_vash10)=emiss_ash_mass
 do ko=1,k_final
   if(emissoptvol == 2)emis_vol(ni,ko,nj,p_e_vso2)=so2_mass

! Added a line to store the water vapor emissions into the WRF-Chem
! chemistry grid via p_ke_h2o.
   if(emissoptvol == 2)emis_vol(ni,ko,nj,p_ke_h2o)=h2o_flux
  enddo
end subroutine volcemiss
FUNCTION juldate(YYYYMMDD,HHMISS)
IMPLICIT NONE
integer, parameter :: double_k = selected_real_kind(15,307)
integer, parameter :: dp=double_k
INTEGER :: YYYYMMDD,YYYY,MM,DD,HH,MI,SS,HHMISS
INTEGER :: JULDAY,JY,JM,JA,IGREG
REAL (kind=dp) ::  JULDATE
PARAMETER (IGREG=15+31*(10+12*1582))
YYYY=YYYYMMDD/10000
MM=(YYYYMMDD-10000*YYYY)/100
```

```
DD=YYYYMMDD-10000*YYYY-100*MM
HH=HHMISS/10000
MI=(HHMISS-10000*HH)/100
SS=HHMISS-10000*HH-100*MI
IF (YYYY.EQ.0) PAUSE 'There is no Year Zero.'
IF (YYYY.LT.0) YYYY=YYYY+1
IF (MM.GT.2) THEN
  JY=YYYY
  JM=MM+1
ELSE
  JY=YYYY-1
  JM=MM+13
ENDIF
JULDAY=INT(365.25*JY)+INT(30.6001*JM)+DD+1720995
IF (DD+31*(MM+12*YYYY).GE.IGREG) THEN
  JA=INT(0.01*JY)
  JULDAY=JULDAY+2-JA+INT(0.25*JA)
ENDIF
JULDATE=DBLE(REAL(JULDAY))+DBLE(REAL(HH)/24.)+&
&DBLE(REAL(MI)/1440.)+DBLE(REAL(SS)/86400.)
END FUNCTION juldate
```

! The following subroutine is used to calculate the horizontal and

! vertical grid cells of the volcano in the model, however in the near

!real time version, they are hardcoded to 200,200 at the center.

```
SUBROUTINE getij(ni,nj)

integer :: ni,nj

ni=200

nj=200

end subroutine getij

END Module module_volc_emiss_driver
```

Filename: check.sh

File location: Domain Generator alerts folder

Description: This script is an example of how the real time WRF-Chem code is triggered to generate a model run upon receiving an alert via e-mail. This script is an example that may be tailored to parse through any number of sources of volcanic emissions alerts. It is intended to be run using a cron job in a Linux environment. In the case of this file, comments begin with the # (bang) symbol, which is customary for Linux Bourne again shell (bash) scripts.

```
#!/bin/bash
# Here, grep searches a email text file for the term HIGH. This can be applied to RSS feeds, HTML code, or
# text messages.
if cat *.eml | grep -q "Alert Confidence: HIGH"; then

# If the term HIGH in this case then the latitude, longitude and height of the plume are written to the
# domain.asc file that is read in by further scripts.
    grep Latitude *.eml | awk {'print $5'} > ../namelists/domain.asc
    grep Longitude *.eml | awk {'print $5'} >> ../namelists/domain.asc
    grep 'Mean Object Date' *.eml | awk {'print $4'} >> ../namelists/domain.asc
    grep 'Mean Object Date' *.eml | awk {'print $5'} >> ../namelists/domain.asc
    grep 'Maximum Height' *.eml | awk {'print $4'} >> ../namelists/domain.asc
    awk '/Volcanoes \(meeting alert/{getline; print}' *.eml >> ../namelists/domain.asc
    cp ../namelists/domain.asc ../volc_info
    mv *.eml ./archived
    cd /center1/VOLCWRF/VOLCWRF/operational_v2
# Since an alert was found, the Slurm script below is launched for the cluster to begin a run.
    sbatch Operational_WPS.slurm
```

```
    else
echo "NO ALERT"
    fi
```

Filename: generateWPSnamelist.py

File location: Name lists folder in near real time WRF-Chem directory.

Description: This Python 2.7 program automatically generates a name list for use in the WRF Pre-Processing System for an automatic WRF-Chem launch which is named namelist.wps. The name list template used to generate the name list follows this code.

```
#!/usr/bin/env python
import datetime
import csv
nametpl='namelist.wps'
data=[]
with open('domain.asc', 'rU') as source:
  reader = csv.reader(source)#, delimiter=' ')
  for row in reader:
    data.append(row)
today = datetime.date.today()
#tomorrow is timedelta of 2 days because we need
#the day after tomorrow at midnight for the last
#48 hour run to be complete.
tomorrow = today + datetime.timedelta(days=2)
yesterday = today + datetime.timedelta(days=-1)
datadict={}
datadict['year1']=str(yesterday.year)
datadict['year2']=str(tomorrow.year)
datadict['day1']=str(yesterday.day).zfill(2)
datadict['day2']=str(tomorrow.day).zfill(2)
datadict['month1']=str(yesterday.month).zfill(2)
datadict['month2']=str(tomorrow.month).zfill(2)
```

```
datadict['lat']=data[0][0]
datadict['lon']=data[1][0]
datadict['intervalSeconds']=str(21600)

namedict={}
name=[x.strip().split('(') for x in data[5]]
namedict['volcanoName']='%s' %name[0][0]
namedict['lat'] =data[0][0]
namedict['lon'] =data[1][0]
template=open('namelist.wps.tpl','rU').read()
fh=open(nametpl,'w')
fh.write(template%datadict)
fh.close
fh.close
```

Filename: WPSnamelist.tpl

File location: Name lists folder in near real time WRF-Chem directory.
Description: This Python template is used to automatically generate a name list for the WRF Pre-processing System in the event of an automatic launch.

```
 &share
  wrf_core = 'ARW',
  max_dom = 1,
  start_date = '%(year1)s-%(month1)s-%(day1)s_00:00:00',
  end_date   = '%(year2)s-%(month2)s-%(day2)s_00:00:00',
  interval_seconds = %(intervalSeconds)s,
  io_form_geogrid = 2,
 /
 &geogrid
  parent_id         =   1,   1,   2,   3,
  parent_grid_ratio =   1,   3,   3,   3,
  i_parent_start    =   1,  67,  67,  67,
  j_parent_start    =   1,  67,  67,  67,
  e_we              =  400, 199, 199, 199,
  e_sn              =  400, 199, 199, 199,
  geog_data_res     = '30s','30s','2s', '2s',
  dx = 10000,
  dy = 10000,
  map_proj = 'lambert',
  ref_lat   =  %(lat)s,
  ref_lon   =  %(lon)s,
  truelat1  =  %(lat)s,
  truelat2  =  %(lat)s,
  stand_lon =  %(lon)s,
```

```
 geog_data_path = '/center1/VOLCWRF/VOLCWRF/operational_v2/WPS_GEOG'
/
&ungrib
 out_format = 'WPS',
 prefix = 'FILE',
/
&metgrid
 fg_name = 'FILE'
 io_form_metgrid = 2,
/
&mod_levs
 press_pa = 201300 , 200100 , 100000 ,
            95000 ,  90000 ,
            85000 ,  80000 ,
            75000 ,  70000 ,
            65000 ,  60000 ,
            55000 ,  50000 ,
            45000 ,  40000 ,
            35000 ,  30000 ,
            25000 ,  20000 ,
            15000 ,  10000 ,
             5000 ,   1000
/
```

Filename: generateWRFnamelist.py

File location: Name lists folder in near real time WRF-Chem directory.
Description: This Python 2.7 program automatically generates a name list for use by WRF-Chem for an automatic launch. The name list template used to generate the name list follows this code. It generates two name lists, one namelist.input.day0 that is used to initialize the WRF meteorological fields and the other namelist.input.day1 that is used for the WRF-Chem run. The name list template follows this code.

```
#!/usr/bin/env python

import datetime

import csv

day0tpl='namelist.input.day0'

#day1NOChemtpl='namelist.input.day1NOchem'

day1Chemtpl='namelist.input.day1chem'

today = datetime.date.today()

tomorrow = today + datetime.timedelta(days=2)

yesterday = today + datetime.timedelta(days=-1)

day0dict={}

day0dict['yearLess1']=str(yesterday.year)

day0dict['dayLess1']=str(yesterday.day).zfill(2)

day0dict['monthLess1']=str(yesterday.month).zfill(2)

day0dict['yearLess2']=str(today.year)

day0dict['dayLess2']=str(today.day).zfill(2)

day0dict['monthLess2']=str(today.month).zfill(2)

day1dict={}

day1dict['year1']=str(today.year)

day1dict['day1']=str(today.day).zfill(2)

day1dict['month1']=str(today.month).zfill(2)

day1dict['year2']=str(tomorrow.year)

day1dict['month2']=str(tomorrow.month)
```

```
day1dict['day2']=str(tomorrow.day)
template=open('namelist.input.day0.tpl','rU').read()
fh=open(day0tpl,'w')
fh.write(template%day0dict)
fh.close
template3=open('namelist.input.day1chem.tpl','rU').read()
fh=open(day1Chemtpl,'w')
fh.write(template3%day1dict)
fh.close
```

Filename: namelist.input.day1chem.tpl

File location: Name lists folder in near real time WRF-Chem directory.
Description: This Python template is used to automatically generate a name list for WRF in the event of an automatic launch.

```
#!/usr/bin/env python

import datetime

import csv

day0tpl='namelist.input.day0'

day1Chemtpl='namelist.input.day1chem'

today = datetime.date.today()

tomorrow = today + datetime.timedelta(days=2)

yesterday = today + datetime.timedelta(days=-1)

day0dict={}

day0dict['yearLess1']=str(yesterday.year)

day0dict['dayLess1']=str(yesterday.day).zfill(2)

day0dict['monthLess1']=str(yesterday.month).zfill(2)

day0dict['yearLess2']=str(today.year)

day0dict['dayLess2']=str(today.day).zfill(2)

day0dict['monthLess2']=str(today.month).zfill(2)

day1dict={}

day1dict['year1']=str(today.year)

day1dict['day1']=str(today.day).zfill(2)

day1dict['month1']=str(today.month).zfill(2)

day1dict['year2']=str(tomorrow.year)

day1dict['month2']=str(tomorrow.month)

day1dict['day2']=str(tomorrow.day)

template=open('namelist.input.day0.tpl','rU').read()

fh=open(day0tpl,'w')
```

```
fh.write(template%day0dict)
fh.close

template3=open('namelist.input.day1chem.tpl','rU').read()
fh=open(day1Chemtpl,'w')
fh.write(template3%day1dict)
fh.close
```

Filename: generateVolcInfo.py

File location: Name lists folder in near real time WRF-Chem directory.
Description: This Python template generates the volc_d01.asc name list from the volc_d01.asc.tpl Python template (that follows this code).

```
#!/usr/bin/env python

import datetime

import csv

volcout='volc_d01.asc'

data=[]

with open('domain.asc', 'rU') as source:

  reader = csv.reader(source)#, delimiter=' ')

  for row in reader:

    data.append(row)

today = datetime.date.today()

erup_hour=[x.split(':') for x in data[3]]

tomorrow = today + datetime.timedelta(days=1)

tomorrow2 = today + datetime.timedelta(days=2)

yesterday = today + datetime.timedelta(days=-1)

datadict={}

datadict['i']=str(data[6][0])

datadict['j']=str(data[7][0])

datadict['year1']=str(yesterday.year)

datadict['year2']=str(today.year)

datadict['year3']=str(tomorrow.year)

datadict['year4']=str(tomorrow2.year)

datadict['day1']=str(yesterday.day).zfill(2)

datadict['day2']=str(today.day).zfill(2)

datadict['day3']=str(tomorrow.day).zfill(2)
```

```
datadict['day4']=str(tomorrow2.day).zfill(2)
datadict['month1']=str(yesterday.month).zfill(2)
datadict['month2']=str(today.month).zfill(2)
datadict['month3']=str(tomorrow.month).zfill(2)
datadict['month4']=str(tomorrow2.month).zfill(2)
datadict['lat']=data[0][0]
datadict['lon']=data[1][0]
datadict['intervalSeconds']=str(21600)
datadict['date1']=str(datadict['year1']+datadict['month1']+datadict['day1'])
datadict['date2']=str(datadict['year2']+datadict['month2']+datadict['day2'])
datadict['date3']=str(datadict['year3']+datadict['month3']+datadict['day3'])
datadict['date4']=str(datadict['year4']+datadict['month4']+datadict['day4'])
if int(erup_hour[0][0]) in range(0,3):
  datadict['height0'] = str(int(float(data[4][0])*1000))
else:
  datadict['height0'] = str(0).zfill(4)
if int(erup_hour[0][0]) in range(3,6):
  datadict['height1'] = str(int(float(data[4][0])*1000))
else:
  datadict['height1'] = str(0).zfill(4)
if int(erup_hour[0][0]) in range(6,9):
  datadict['height2'] = str(int(float(data[4][0])*1000))
else:
  datadict['height2'] = str(0).zfill(4)
if int(erup_hour[0][0]) in range(9,12):
  datadict['height3'] = str(int(float(data[4][0])*1000))
else:
```

```
  datadict['height3'] = str(0).zfill(4)
if int(erup_hour[0][0]) in range(12,15):
  datadict['height4'] = str(int(float(data[4][0])*1000))
else:
  datadict['height4'] = str(0).zfill(4)
if int(erup_hour[0][0]) in range(15,18):
  datadict['height5'] = str(int(float(data[4][0])*1000))
else:
  datadict['height5'] = str(0).zfill(4)
if int(erup_hour[0][0]) in range(18,21):
  datadict['height6'] = str(int(float(data[4][0])*1000))
else:
  datadict['height6'] = str(0).zfill(4)
if int(erup_hour[0][0]) in range(21,24):
  datadict['height7'] = str(int(float(data[4][0])*1000))
else:
  datadict['height7'] = str(0).zfill(4)

template=open('volc_d01.tpl','rU').read()
fh=open(volcout,'w')
fh.write(template%datadict)
fh.close
```

Filename: volc_d01.asc.tpl

File location: Name lists folder in near real time WRF-Chem directory.
Description: This is a Python template file that is used to generate the eruption information file volc_d01.asc used by the WRF-Chem executables for the initialization of the volcanic ash fields. Note that Line 3 may be edited such that the height offsets in the model may be specified by the user.

By line: number of time steps, heights, i, j

41

.3 .7 1.0 1.5 3.0

200

200

YYYYMMDD HHMMSS MIN HEIGHT(m) ERUPTIONA ERUPTIONS ERUPTIONH

%(date1)s 000000 180 0000 0.000e+00 0.000e+00 0.000e+00

%(date1)s 030000 180 0000 0.000e+00 0.000e+00 0.000e+00

%(date1)s 060000 180 0000 0.000e+00 0.000e+00 0.000e+00

%(date1)s 090000 180 0000 0.000e+00 0.000e+00 0.000e+00

%(date1)s 120000 180 0000 0.000e+00 0.000e+00 0.000e+00

%(date1)s 150000 180 0000 0.000e+00 0.000e+00 0.000e+00

%(date1)s 180000 180 0000 0.000e+00 0.000e+00 0.000e+00

%(date1)s 210000 180 0000 0.000e+00 0.000e+00 0.000e+00

%(date2)s 000000 180 %(height0)s 0.000e+00 0.000e+00 0.000e+00

%(date2)s 030000 180 %(height1)s 0.000e+00 0.000e+00 0.000e+00

%(date2)s 060000 180 %(height2)s 0.000e+00 0.000e+00 0.000e+00

%(date2)s 090000 180 %(height3)s 0.000e+00 0.000e+00 0.000e+00

%(date2)s 120000 180 %(height4)s 0.000e+00 0.000e+00 0.000e+00

%(date2)s 150000 180 %(height5)s 0.000e+00 0.000e+00 0.000e+00

%(date2)s 180000 180 %(height6)s 0.000e+00 0.000e+00 0.000e+00

%(date2)s 210000 180 %(height7)s 0.000e+00 0.000e+00 0.000e+00

%(date3)s 000000 180 0000 0.000e+00 0.000e+00 0.000e+00

%(date3)s 030000 180 0000 0.000e+00 0.000e+00 0.000e+00

%(date3)s 060000 180 0000 0.000e+00 0.000e+00 0.000e+00

%(date3)s 090000 180 0000 0.000e+00 0.000e+00 0.000e+00

%(date3)s 120000 180 0000 0.000e+00 0.000e+00 0.000e+00

%(date3)s 150000 180 0000 0.000e+00 0.000e+00 0.000e+00

%(date3)s 180000 180 0000 0.000e+00 0.000e+00 0.000e+00

%(date3)s 210000 180 0000 0.000e+00 0.000e+00 0.000e+00

%(date4)s 000000 180 0000 0.000e+00 0.000e+00 0.000e+00

%(date4)s 030000 180 0000 0.000e+00 0.000e+00 0.000e+00

%(date4)s 060000 180 0000 0.000e+00 0.000e+00 0.000e+00

%(date4)s 090000 180 0000 0.000e+00 0.000e+00 0.000e+00

%(date4)s 120000 180 0000 0.000e+00 0.000e+00 0.000e+00

%(date4)s 150000 180 0000 0.000e+00 0.000e+00 0.000e+00

%(date4)s 180000 180 0000 0.000e+00 0.000e+00 0.000e+00

%(date4)s 210000 180 0000 0.000e+00 0.000e+00 0.000e+00